NANOSCALE INFLUENCES ON BIOACTIVITY:
ULTRASTRUCTURE AND NANOMECHANICS OF MODEL BIOACTIVE HYDROXYAPATITE BASED BIOMATERIALS

by

Jennifer M. Vandiver

B.S. Materials Science and Engineering
Massachusetts Institute of Technology, 2001

SUBMITTED TO THE DEPARTMENT OF MATERIALS SCIENCE AND ENGINEERING
IN PARTIAL FULFILLMENT OF THE REQUIREMENTS FOR THE DEGREE OF

DOCTOR OF PHILOSOPHY IN MATERIALS SCIENCE AND ENGINEERING
AT THE
MASSACHUSETTS INSTITUTE OF TECHNOLOGY

MAY 8, 2006
[June 2006]

Author: ______________________________
Department of Materials Science and Engineering
May 8, 2006

Certified by: ______________________________
Professor Christine Ortiz
Professor of Materials Science and Engineering
Thesis Supervisor

Accepted by: ______________________________
Professor Samuel Allen
Professor of Materials Science and Engineering
Chairman, Committee for Graduate Students

Nanoscale Influences on Bioactivity: Ultrastructure and Nanomechanics of Model Bioactive Hydroxyapatite Based Biomaterials

By

Jennifer M. Vandiver

Submitted to the Department of Materials Science and Engineering on May 8, 2006
in Partial Fulfillment of the Requirements for the Degree of Doctor of Philosophy
in Materials Science and Engineering

Thesis Supervisor: Christine Ortiz, Professor of Materials Science and Engineering

ABSTRACT

There is a significant need for improved synthetic materials as orthopedic implants to replace human bone lost and damaged due to disease or injury. Certain ceramics, such as hydroxyapatite (HA), have the special property of being bioactive, meaning that an interfacial bond between the implant and the surrounding tissue forms, leading to good fixation. Bioactive ceramics are being investigated in a wide variety of forms for use in different bone implant applications.

Three model synthetic HA based bioceramic systems were examined; phase pure, dense, polycrystalline HA; phase pure, dense, polycrystalline HA with 0.8 wt% silicon substituted into the lattice (SiHA); and phase pure, dense, nanostructured HA (nanoHA) with grain sizes less than 100 nm. SiHA has shown markedly enhanced bioactivity over non-substituted HA yet they have similar micro- and meso-scale properties and nanoHA has shown increased bioactivity over traditionally structured HA although they are chemically identical.

The form of a biomaterial, the nanoscale surface chemical properties (e.g. surface functional groups, charge distribution, Hamaker constant), and morphological structure (e.g. grain size, shape, distribution, roughness) will govern its interaction with the biological environment. The three main processes thought to occur upon implantation of a bioactive material are the adsorption of ions and biomolecules, formation of calcium phosphate layers, and interactions with various cells [5]. These physiochemical processes are expected to be highly dependent on nanoscale properties since this is the length scale of proteins and cell membrane adhesion molecules.

The direct measurement of ultrastructure and nanoscale surface forces of model HA based biomaterials through atomic force microscopy and positionally- and chemically-specific high resolution force spectroscopy compared with *in vitro* and *in vivo* data will lead to better understanding of the impact these properties have on the physiochemical processes occurring at the biomaterial-biological interfaces influencing bioactivity. Although numerous studies of HA based biomaterials have been reported, there has been little clarification of the molecular mechanisms influencing bioactivity, partly due to lack of rigorous analytical tools for characterizing nanoscale physical and chemical surface properties. Quantifying all possible contributions to bioactivity is critical to the optimization, development, and design of new HA based biomaterials.

BIOGRAPHICAL NOTE

Jennifer Vandiver received a B.S. from MIT, the Department of Materials Science and Engineering in 2001 and her Ph.D. in Bio- and Polymeric Materials from MIT, the Department of Materials Science and Engineering in 2006. She has several publications, was an invited poster presenter at the Cambridge University R&D Seminar, and a MRS fall meeting poster award recipient (2005). Throughout her graduate career she has been involved in teaching several undergraduate MIT classes in the Department of Materials Science and Engineering including; Introduction to Solid-State Chemistry, Microstructural Evolution in Materials, Organic and Biomaterials Chemistry, and Mechanical Properties of Materials.

ACKNOLEDGEMENTS

I would like to thank my advisor Prof. Christine Ortiz for all of her guidance and support. She has been instrumental in my professional development and development of my technical writing skills. I would also like to thank the rest of my thesis committee, Prof. Lorna Gibson, Prof. Myron Spector, and Prof. Krystyn Van Vliet, for their advice and guidance.

I would also like to thank my collaborators and colleagues gained through the Cambridge-MIT alliance at the University of Cambridge, as well as the funding I received through this program. I thank Prof. William Bonfield and Serena Best whose labs produced the materials I needed and who allowed me occasional use of their labs. I would also like to thank Nelesh Patel and James Holder for their help in preparing samples and Roger Brookes and Deborah Ireland for the help in teaching me cell culture. I would especially like to thank Claudia Botelho for her support, collaboration, and friendship.

I would also like to acknowledge all of the laboratories at MIT who made my work possible; the MIT Center for Materials Science and Engineering, the Nanomechanics Laboratory in the Department of Materials Science and Engineering, the laboratories of Prof. Michael Rubner and Prof. Krystyn Van Vliet. I thank you for access to your labs and equipment. In particular I would like to thank Libby Shaw for her experience and assistance with X-ray photospectroscopy.

I would like to thank my colleagues and friends here at MIT who have mentored, guided, and advised me, Delphine Dean, Laurel Ng, and Kaungshin Tai. I have enjoyed working with them. I would additionally like to thank Alexander Hu and Jonathon Tejeda, undergraduate students who worked under my supervision and who contributed significantly to my thesis work.

And lastly, I would like to thank my husband, Benjamin Vandiver, who during his own graduate work has not failed to give me the love, support, and patience I have needed.

TABLE OF CONTENTS

LIST OF FIGURES AND TABLES

CHAPTER 1

CHAPTER 2

CHAPTER 3

CHAPTER 4

CHAPTER 5

CHAPTER 6

CHAPTER 7

CHAPTER 1: Background, Motivation, Materials, and General Techniques

1.1 BACKGROUND AND MOTIVATION

Currently, there is a significant need for improved synthetic materials, for use as orthopedic implants, to replace human bone lost and damaged due to disease or injury. Metals such as stainless steel and titanium have been widely used for hard tissue replacement, but they have various problems such as corrosion, wear, fibrous tissue encapsulation [1], inflammation, implant loosening due to poor adhesion [2], and stress shielding which leads to bone resorption [2,3]. Ceramics are better suited for orthopedic use because they are more mechanically similar to hard biological tissues. Certain ceramics, like calcium phosphates, have the special property of being bioactive, meaning that an interfacial bond between the implant and the surrounding tissue forms, leading to good fixation, and generally no fibrous tissue encapsulation [1,4,5]. Bioactive ceramics, such as hydroxyapatite (HA), are being investigated in a wide variety of forms such as granules, powders, nano-particles, fibers, porous scaffolds, and dense monolithic pieces for use in different bone implant applications, including composites [1]. HA ($Ca_5(PO_4)_3OH$), the stable phase of calcium phosphate at physiological conditions (37°C, pH > 4.2, IS=0.15M) [1], is one of the main constituents of bone (~70 wt. %) [2], and is the model system focused upon in this thesis. The crystal structure of HA is hexagonal, space group $P6_3/m$, with lattice constants a=9.417 and c=6.875 [6], and consists of Ca^{2+} ions surrounded by PO_4^{2-} and OH^- ions as shown in **Fig. 1.1A** [7]. Biogenic HA crystals in bone take the form of platelets that are incorporated within "hole zones" 40 nm × 5 nm with the c-axis parallel to the collagen fiber axis as shown in **Fig. 1.1B** [8,9]. Clinical tests show HA to be nontoxic, produce no inflammatory response, and form a good interfacial bond with bone without fibrous capsule formation [1].

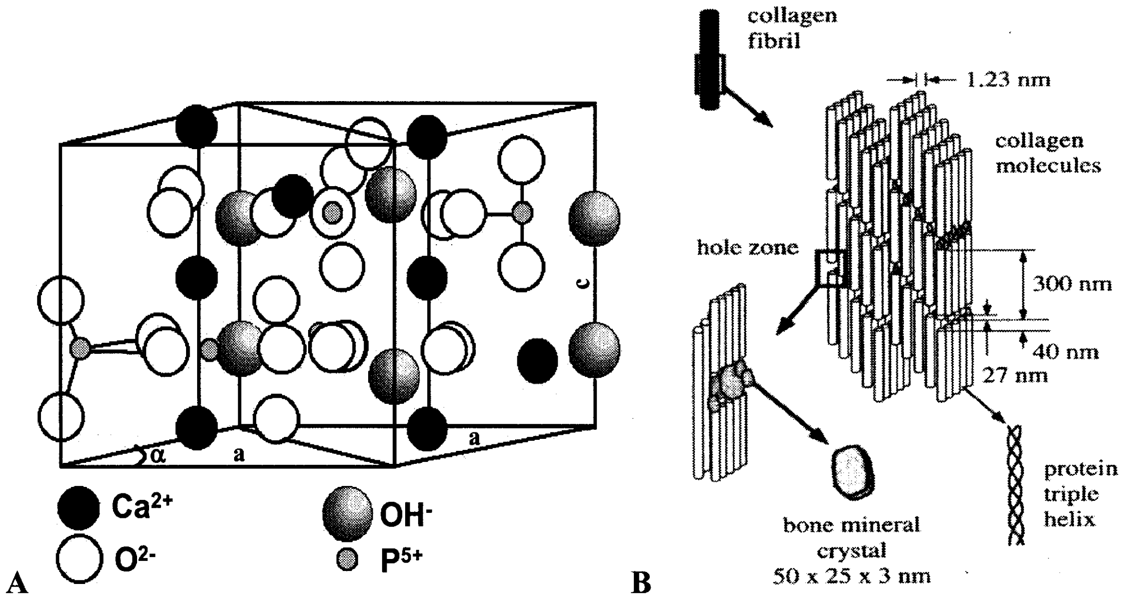

Figure 1.1: **A)** HA unit cell crystal structure [7] **B)** Location and orientation of HA crystals within collagen fibrils in bone [8]

Both nanoscale surface chemical properties (e.g. surface functional groups, charge distribution, Hamaker constant) and morphological structure (e.g. grain size, shape, distribution, roughness) will govern the interaction of material with the biological environment and how well the implant subsequently performs *in vivo*. When HA is implanted into a bony site, a cascade of physiochemical interactions takes place upon exposure to extracellular fluid, resulting in the build up of interfacial layers that bond the bone tissue to the implant material [5,10,11]. Extracellular fluid is composed of interstitial fluid and blood plasma [12] with blood plasma being the predominant fluid that interacts with implanted biomaterials [13]. Plasma contains large amounts of sodium and chloride ions, intermediate amounts of bicarbonate ions, relatively small amounts of potassium, calcium, magnesium, and phosphate ions [12], as well as various proteins. Plasma is highly saturated with respect to calcium phosphates and therefore has great potential to precipitate calcium phosphate [13,14]. The three main processes thought to occur upon implantation of a bioactive biomaterial are adsorption of ions and biomolecules, formation of calcium phosphate (CaP) layers which are generally apatitic in structure, and interactions with various cells [5]. These physiochemical processes are expected to be highly dependent on nanoscale properties since this is the length scale of proteins and cell membrane adhesion molecules. It is well known that nanoscale surface interactions, in particular electrostatics, are a dominant force in protein adhesion [15].

The majority of the literature shows HA to have a negative surface charge in near physiological conditions [16-24]. Negative surface charge of HA is thought to arise from the preferential concentration of PO_4^{3-} groups to the top few nanometers [25] of the surface [26,27]. This Ca deficient surface layer (Ca/P ratio ~1.5 [27]) is expected to be caused by solid-solution equilibrium during the precipitation process used to form stoichiometric HA whereby there is the creation of a vacancy on one of the ten Ca sites, the creation of a vacancy on one of the two hydroxyl sites, and protonation of one of the six PO_4^{3-} groups [27].

The formation of CaP layers when biomaterials are implanted into a bony site [5,10,11,28] is considered essential for the creation of a strong bond with the surrounding tissue [29] and the literature suggests that a negative surface charge is necessary for the formation of these layers. Negative surface functional groups provide preferential sites for nucleation of an amorphous calcium phosphate layer through higher adsorption of positive calcium ions, resulting in a positive layer that will attract negatively charged phosphate groups, leading to the formation of the CaP layer [24,25,30-33]. It has been demonstrated that CaP layers can be reproduced *in vitro* in an aqueous electrolyte solution which mimics the ionic concentrations and pH of human blood plasma, simulated body fluid (SBF) [29,34-38]. Negatively charged self-assembled monolayers have been found to produce the highest growth rate of precipitated CaP layers from SBF [30,31], and electrically polarized, negatively charged ceramic surfaces have been shown to exhibit increased CaP layer formation from SBF [32,33], cell adhesion [39], and osteobonding [40], versus non-poled HA samples. Therefore, it is expected that surface charge will have a strong influence on the processes of inorganic and organic deposition and structural evolution on the implant material, particularly during the initial stages of implantation.

The hypothesis of this thesis is that the nanoscale surface properties of model HA based biomaterials affect the physiochemical processes occurring at the biomaterial-biological interfaces and therefore influence bioactivity. This hypothesis is explored by the direct measurement of the ultrastructure and nanoscale surface forces of model HA based biomaterials and comparison with *in vitro* and *in vivo* data. Three model systems were studied: phase pure synthetic, polycrystalline, dense HA; silicon-substituted phase pure synthetic, polycrystalline, dense HA (SiHA); and nanostructured phase pure synthetic, polycrystalline, dense HA (nanoHA). Although numerous studies of HA have been reported, there has been little clarification of the molecular mechanisms influencing bioactivity, partly due to previous lack of rigorous analytical tools for characterizing nanoscale physical and chemical surface properties.

1.2 MODEL HA-BASED BIOMATERIALS

1.2.1 Phase pure HA

Three model synthetic HA-based materials were examined. The first was phase pure, dense, polycrystalline HA pellets (**Figure 1.2A**). Synthetic HA was prepared by an aqueous precipitation reaction between analytical grade calcium hydroxide ($Ca(OH)_2$) and phosphoric acid (H_3PO_4) solution [41]. To ensure purity of the samples, the reaction vessels were thoroughly cleaned and rinsed with deionized (DI) water prior to use. The precipitation process proceeded as follows: a calcium hydroxide solution was made up by initially stirring 0.5 moles of $Ca(OH)_2$ in 1 liter of DI water. Similarly, 0.299 moles of H_3PO_4 solution were dissolved in 1 liter of DI water. The precipitation reaction occurred when the H_3PO_4 solution was added dropwise to the $Ca(OH)_2$ solution over a period of 2-3 hours at ambient temperature. During the precipitation process the pH of the reaction was maintained at 10.5 by small additions of 25% ammonia solution. The precipitate was filtered under vacuum, thoroughly washed with approximately 100 ml of DI water, and then placed in a glass drying dish to dry at $80^{\circ}C$ for 24 hours in air. The dried HA filter-cake was then crushed using a pestle and mortar and sieved to a particle size less than 75 μm in diameter. The green powder was then either sintered or pressed into pellets using an isostatic press and subsequently sintered to $1200^{\circ}C$ for 2 hours in air. The pellets have an average width of 3.8 mm, an average diameter of 8.64 mm, and are >98% of the theoretical density (3.16 g/cm^3) as measured by water displacement. Purity of the HA pellets was determined via Wide Angle X-ray Diffraction (WAXD) and X-ray fluorescence spectroscopy (XRF). Surface Ca/P ratio was measured via X-ray photospectroscopy (XPS). Due to solid-solution equilibrium during the precipitation process, surface Ca/P ratio is typically less than the stoichiometric bulk Ca/P ratio of 1.67 [27] and may be affected by grain size.

Although this model system is very similar to the mineral component of bone, there are a number of differences between synthetic and biogenic HA. The model system is monolithic, polygranular, dense pellets, while biogenic HA is in the form of isolated platelets, approximately 10 nm in diameter and 1 nm in thickness [42]. Synthetic HA is stoichiometric with a bulk Ca/P ratio of 1.67, while biological HA has varied Ca/P ratios depending on age and specific tissue [8,26]. Additionally, biological HA is not phase pure, it contains small amounts of CO_3, Mg, Na, F and/or Cl. As a result of these ionic substitutions, changes in the lattice parameters can occur, as well as shifts in crystal structure [26]. Synthetic HA provides a well-defined, chemically homogenous model system for nanoscale studies.

1.2.2 Phase pure SiHA

The second model material studied was synthetic, phase pure, dense, polycrystalline HA with 0.8 wt% silicon substituted into the lattice (SiHA) which did not significantly alter the crystal structure [43] (**Fig. 1.2B**). SiHA was prepared through a similar aqueous precipitation reaction between calcium hydroxide ($Ca(OH)_2$) and phosphoric acid (H_3PO_4) solution with silicon tetraacetate (SiAcetate) added to the reaction as a source of silicate ions [43]. Since silicate ions substitute in for phosphate ions, the molar amounts of reactants was calculated such that (H_3PO_4 + SiAcetate) was the equivalent to (H_3PO_4) in stoichiometric HA. The precipitate was washed, dried, ground, sieved, pressed, and sintered similar to HA to create pellets of similar dimensions and density. SiHA has shown markedly enhanced *in vitro* CaP layer formation in SBF [25,44,45], increased *in vitro* cell proliferation and creation of focal points of adhesion [46], as well as *in vivo* bone ingrowth [47] and remodeling [48] compared to non-substituted HA. HA and SiHA have significantly different bioactivity properties yet similar micro- and meso-scale properties. Therefore, examining how the incorporation of silicon affects nanoscale properties such as electrostatic repulsion, van der Waals interactions, and morphology of precipitated apatite layers has great potential to contribute important information relevant to the molecular origins of HA bioactivity.

1.2.3 Phase pure nanostructured HA

The third model material, synthetic, phase pure, dense, nanostructured HA (nanoHA) with grain sizes less than 100 nm (**Fig. 1.2C**), was donated by *Angstrom Medica* (Woburn, MA). Briefly, it was prepared through an aqueous precipitation reaction between analytical grade

$Ca(NO_3)_2 \cdot 4H_2O$ and $(NH_4)_2HPO_4$ [49]. The precipitate was washed, ground, dried, and aged with processing parameters such as solution pH, aging time and temperature adjusted to achieve desired ultrafine spherical particles which were then subjected to pressure-assisted sintering at 90°C for 30 minutes at a pressure of 100 MPa. The resulting material is transparent and 98.5% of theoretical density of HA [49,50]. One reason nanoHA is desirable, is because of its increased mechanical properties over traditional microstructured HA [50].

Additionally, nanostructured HA is more similar to the length scale of biogenic HA in bone and potentially can provide insights into *in vivo* biological interactions. Nanostructured ceramics such as alumina, titania, and HA have shown increased bioactivity through enhanced protein adsorption [51], osteoblast adhesion [52] and osteoblast function [53] compared to their respective microstructured ceramics. Investigations of nanoscale surface properties of nanoHA compared to traditional microstructured polycrystalline HA will determine the changes, if any, in surface interactions (e.g. surface charge distribution, Hamaker constant) due to nanostructuring which could account for bioactivity differences.

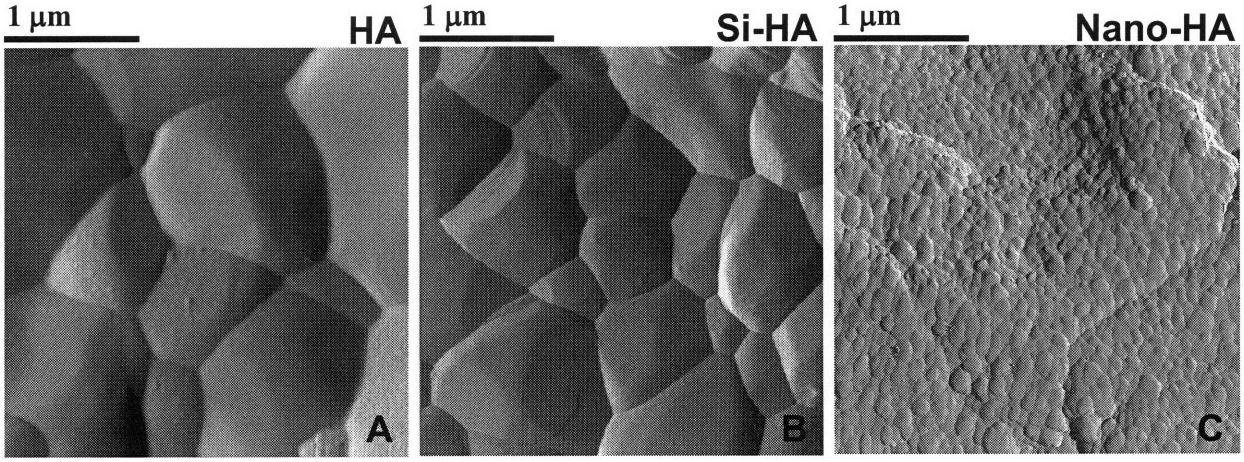

Figure 1.2: Tapping mode amplitude atomic force microscopy images of **A)** HA (grain size = 1.48 ± 0.68 μm) **B)** SiHA (grain size = 0.73 ± 0.40 μm) and **C)** NanoHA (grain size 83 ± 27 nm).

Property	**Technique**	**HA**	**Si-HA**	**NanoHA**
Ca/P ratio Ca/(P+Si)	X-ray Photospectroscopy	1.63	1.54	1.45
Density	Water Displacement	~98% theoretical	~98% theoretical	~98.5% theoretical
Grain size	Atomic Force Microscopy	1.48±0.68μm	0.73±0.40μm	83±27nm
Contact angle	Video Contact Angle Measurement	75±2°	65±2°	69±4°
200nm linear intragrain RMS roughness	Atomic Force Microscopy	1.1±0.37nm	0.93±0.36nm	5.9±2.9nm
Crystal structure	X-ray Diffraction	hydroxyapatite	hydroxyapatite	hydroxyapatite

Table 1.1: Comparison of surface material properties for HA, SiHA, and NanoHA

1.3 GENERAL TECHNIQUES

1.3.1 Atomic force microscopy (AFM)

Since its development in the early 1980's, scanning probe microscopy and subsequently developed atomic force microscopy (AFM), have added enormously to the understanding of surface structure and function from the atomic scale upwards [54,55]. AFM imaging is based on a microfabricated cantilever force transducer with a fine probe tip whose deflection allows for the measurement of surface topographical imaging with <1 nm lateral resolution. The largest advantage of AFM is its ability to image without the need for vacuum in air or fluids, including near-physiological aqueous electrolyte solutions [54,55]. The technique works by reflecting a laser off of a cantilever onto a position sensitive photodiode. For imaging purposes, as the cantilever moves over the surface and is deflected, the position of the laser on the photodiode is recorded, and gives a deflection image. A piezoelectric scanner then adjusts the height of the cantilever in order to keep the cantilever deflection constant. The amount the piezo moves is also recorded, and gives a height image. A schematic is shown in **Fig. 1.3A**. The majority of

AFM imaging was performed on a *Digital Instruments Veeco* Nanoscope IIIA System Controller with Multimode Atomic Force Microscope (AFM) capable of contact, tapping, and force modulation imaging modes in air and fluids.

AFM has been used to image a wide array of materials including superconductors, semiconductors, metals, polymers, ceramics, and biological molecules [54-58]. Both biogenic and synthetic bioceramics such as tooth enamel [59], mammalian skeletal HA [60], synthetic single crystals of HA [61], synthetic HA and synthetic brushite powders [62] have been examined via AFM. In addition to surface topology; deposition, precipitation, adsorption, growth, and mineralization process have been observed [34,35,54-56,63]. Since AFM can be preformed in aqueous environments, it is a powerful tool for studying biological systems and has been used to image proteins, DNA, other biomolecules and cell surface morphology as well as to study protein absorptions, cell migration, and organelle movement [54,55,58].

1.3.2 High Resolution Force Spectroscopy

1.3.2.1 Molecular Force Probe

An extensive portion of this thesis employed the relatively new technique of positionally- and chemically-specific high resolution force spectroscopy (HRFS). HRFS is a nanomechanical technique which is also based on a microfabricated cantilever force transducer, and can measure piconewton (pN)-level surface interaction forces. HRFS experiments were performed using both a one and three-dimensional Molecular Force Probes (1DMFP and 3DMFP, respectively, *Asylum Research, Inc.*). The MFP is engineered for maximum force sensitivity and minimal interference through novel optical lever geometry and a low coherence light source. The three dimensional version has the additional capability to image and perform nanomechanical measurements with nanometer-scale spatial sensitivity allowing one to AFM image and probe a sample simultaneously in order to compare forces to observed nanoscale topographical surface features. The 3DMFP has closed loop uncoupled stacked piezos to minimize drift during imaging and probing. The open fluid cell design of the MFP allows measurements to be taken in near-physiological conditions. A full description of this instrument, its limits, procedures for spring constant calibration and raw data conversion, and details of measurement errors are given in previous work [64]. A schematic is shown in **Fig. 1.3B.**

During HRFS, the cantilever is displaced perpendicular to a sample surface (i.e. z-direction) at a constant rate on approach (towards the surface) and on retract (away from the surface) after contact. All experiments in this thesis were performed using displacement control. The deflection of the cantilever is measured and after calibrating the cantilever spring constant [64], a force versus tip-sample separation distance curve (F-D curve) can be constructed. A schematic of an F-D curve is shown in **Fig. 1.4** with the important positions labeled. Analysis of F-D curves allows the attractive or repulsive forces on approach, as well as adhesion force and distance on retract, between the probe tip and the surface to be quantified [65,66]. The F-D curve for approach and F-D curve for retract may or may not differ depending on surface interactions. In all HRFS experiments, the spring constant of the cantilever is much less than the stiffness of the substrate such that little or no deformation occurs, leading to the D=0 vertical region of apparent infinite slope in the high-force constant compliance regime.

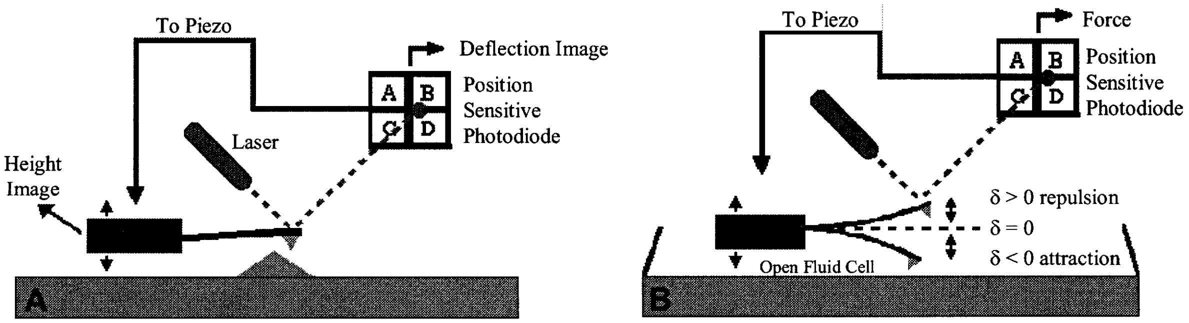

Figure 1.3: Schematic of **A)** AFM imaging and **B)** HRFS.

1.3.2.2 Probe Tip Characterization

Thermomicroscopes, V-shaped, Si_3N_4 cantilever probe tips were first coated with ~2 nm coat of chromium (Cr) and then coated with ~20 nm of gold (Au) through electron beam evaporation. To functionalize, the Au-coated cantilever probe tips were cleaned in O_2 plasma for 10s and immediately placed in specific 1 mM SAM solutions in 100% ethanol for 18 hrs, after which they were rinsed with 100% ethanol and stored in Millipore water (18 MΩ·cm resistivity). The spring constant of each tip was measured in the MFP by a thermal vibration method [64] . The probe tip end radius, R_{TIP}, was measured via *JEOL* 6320FV Field-Emission High-resolution SEM by digitally drawing a circle on a 100,000× SEM image within the point of the tip and comparing the radius of the circle to the image scale bar. A typical image is shown in **Fig 1.5**.

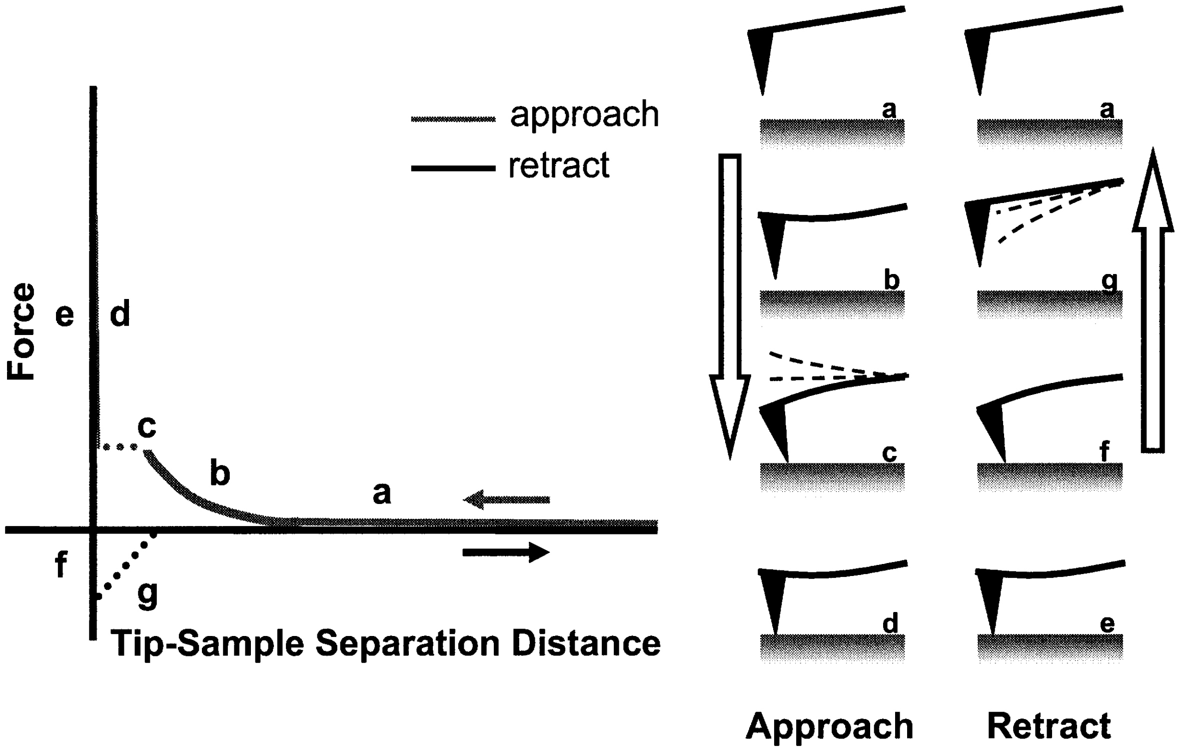

Figure 1.4: Schematic of an F-D curve showing a) initial non-contact region, b) repulsive region, c) jump to contact, d) consistent compliance region on approach, e) consistent compliance region on retract, f) adhesion, g) pull off followed by return to non-contact region.

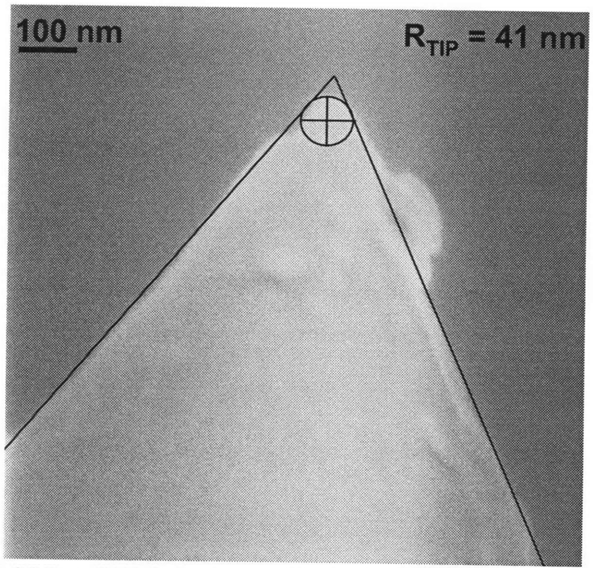

Figure 1.5: Typical 100,000× SEM image of an Au-coated *Thermomicroscopes* probe tip demonstrating determination of R_{TIP}.

1.3.2.3 HRFS Applied to Biomaterials

HRFS has moved AFM technology from high resolution imaging to ultra-precise surface force measurement, which can provide information on local material properties such as elasticity, Hamaker constant, surface charge, and adhesion [67,68]. The ability to modify probe tips using ω-functionalized alkyl thiol self-assembling monolayers (SAMs) allows for the direct measurement of forces between a nanosized probe tip functionalized with molecules of uniform and known structure, chemistry, and charge as a function of separation distance from a sample of interest [69,70] which in turn can be compared to theoretical calculations (i.e. Derjaguin-Landau-Verwey-Overbeek, DLVO, theory). HRFS has been used to measure DLVO forces in electrolyte solutions for many materials including glass, silica, silicon nitride, gold, copper, nickel, zinc, lead sulphide, titanium oxide, zirconia, iron oxide, tungsten, cobalt, aluminum, various polymers, and other thin organic layers [67]. Additionally, by combining raster scanning and measurement of surface forces, one could map material surface forces with nanometer resolution.

This has been done for natural skeleton hydroxyapatite [71] as well as thin films, aggregates of lysozyme, and single molecules of DNA [68].

1.3.2.4 Theoretical Analysis of F-D Curves

Following Derjaguin-Landau-Verwey-Overbeek (DLVO) theory [72], the total net interaction force measured on approach is assumed to be a linear summation of an attractive van der Waals component and a repulsive electrostatic double layer component as follows:

$$F_{total}(D) = F_{electrostatic}(D) + F_{vdw}(D) \qquad (1.1)$$

$F_{electrostatic}$ is dependant on surface charge per unit area, σ (C/m^2), and F_{vdw} is dependant on Hamaker constant, A (zJ). The non-retarded van der Waals force approximately follows an inverse square power law where F_{vdw} is the van der Waals force between a sphere of radius R (assumed equal to the probe tip radius, R_{TIP}) and a planar surface separated by a distance D [73]:

$$F_{VDW} = \frac{AR_{TIP}}{6D^2} \qquad (1.2)$$

The Hamaker constant is a reflection of the 7 layered system Si_3N_4/Cr/Au/S/-$(CH_2)_{10}$-COO^- /aqueous electrolyte(IS=0.01M, pH=7.4)/sample. Previous experiments have suggested that the underlying metal layers (A~100 zJ) are more dominant than the SAM layers since the SAM layer has a much smaller polarizability [74]. One could try to estimate the contributions of each of the layers via comparison with the predictions of a Lifshitz multilayered model, however the lack of knowledge of the exact metal layer thicknesses would render these results imprecise [75]. When possible, the same exact tip material, metal coatings, SAM, and solution were used to probe the samples and hence, the relative differences observed in A can be attributed solely to the surface characteristics of those samples. Since the criterion for the mechanical instability of the cantilever (jump-to-contact) is when the derivative of the force profile or force gradient exceeds the cantilever spring constant (dF/dD>k) [69], an average Hamaker constant can also be estimated at each position from the cantilever jump-to-contact separation distances ($D_{\text{jump-to-contact}}$) when cantilever spring constant, k, is known as follows:

$$D_{\text{jump-to-contact}} = \left[\frac{AR_{TIP}}{3\text{k}}\right]^{1/3} \qquad (1.3)$$

The values of *A* calculated from the jump-to-contact method and **Eq. 1.3** can be compared to fits of high ionic strength (1M) nanomechanical data (where electrostatic double layer forces are largely screened out) to **Eq. 1.2**. $F_{\text{electrostatic}}$ can be approximated for each position by a Poisson-Boltzmann-based formulation. The Poisson-Boltzmann (PB) equation gives an expression for the electrical potential, Φ (volts), between two charged planar surfaces in an electrolyte solution (**Fig. 1.6**). For a monovalent 1:1 electrolyte, the solution has the form:

$$\nabla^2\Phi = \frac{2FC_0}{\varepsilon_w}\sinh\left(\frac{F\Phi}{RT}\right) \qquad (1.4)$$

where *F* is the Faraday constant (96,500 C/mol), C_0 is the bulk concentration of ions (mol/m^3), ε_w is the dielectric permittivity of water ($6.9 \bullet 10^{-10}$ C/Nm^2), R is the universal gas constant (8.314 J/mol K), and T is the absolute temperature (K) [72,76,77]. Constant charge boundary conditions were used, since neither the probe tip nor the substrate is electrically connected to any source that would maintain them at a constant potential [78], such that the electric field at the substrate and probe tip surfaces was related to the surface charge per unit area (i.e. $\Delta\Phi_{\text{surface}} = \frac{\sigma_{\text{surface}}}{\varepsilon_{\text{w}}}$ and $\Delta\Phi_{\text{tip}} = -\frac{\sigma_{\text{tip}}}{\varepsilon_{\text{w}}}$.

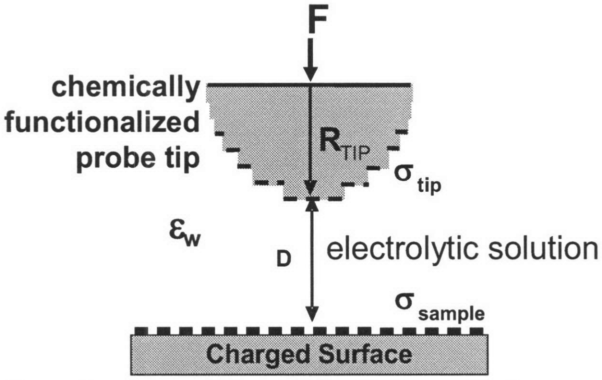

Figure 1.6: Schematic of surface charge model used for Poisson-Boltzmann formulation. [79,80]

A numerical method, known as the Newton method on finite differences [81], was used to solve the nonlinear Poisson-Boltzmann equation. The surface charge per unit area of the probe tip, σ_{tip}, was fixed in the simulations as determined by control experiments using the SAM functionalized probe tip versus a similar SAM functionalized planar substrate and fitting the data to the same electrostatic double layer theory described above. R_{TIP}, *A*, and the solution ionic strength were also fixed parameters and σ_{sample} was the only free fitting variable.

1.3.2.5 HRFS Surface Charge Measurements Compared to Zeta Potential

Once the full nonlinear Poisson-Boltzmann equation is fit to experimental data, the surface potential can be calculated by setting D=0 and solving the Poisson-Boltzmann equation. The surface potential calculated in this way is equivalent to zeta potential [82]. Zeta potential measurements have been the predominant method of surface charge measurement, and are usually performed via electrophoresis on dilute colloidal suspensions or by the streaming potential method on fibers, films, and other macroscopic structures [83]. Zeta potential is the measurement of the double layer electric potential at the slip plane [17], which is the boundary between a layer of more rigidly bound counter ions and the diffuse electrostatic double layer of highly mobile, hydrated counter ions. The sign and magnitude of the zeta potential depends on the polarity of adsorbed ions, and the surface charge of the solid. Zeta potential measurements have variability due to particle size and shape [84] as well as IS of measurement solution [17,82].

Zeta potential measurements of HA have been preformed numerous times in the literature but there is a large degree of variability between methods and samples. The surface potentials calculated from zeta potential measurements performed near physiological pH, but at varied IS, have varied from -50 mV [25] to 3 mV [17], although the majority of measurements have been between -5 and -20 mV [16-24]. Ionic species present in and IS of measurement solution, as well as substituted impurities, phase impurities, Ca-deficiency, and lattice defects in the HA samples could all be possible causes for variation [17,20,85]. Additionally, it has been shown that the surface potentials of HA samples can vary over time in solution [17,86].

Typically, zeta potential measured by microelectrophoretic and other techniques are expected to be lower, 30-50%, than fitted potentials for nanomechanical data ideal (smooth) surfaces [87] because of the potential drop in the immobilized liquid layer close to the surface [88]. This layer moves with the particle in zeta potential measurements, but is not included in Poisson-Boltzmann theory [88], since the slip plane where zeta potential is measured is further from the surface than the Stern surface where Poisson-Boltzmann theory begins [88]. The surface charges calculated via HRFS data is the effective charge at the stern surface since electrostatic double layer theory is valid only within the diffuse double layer [82].

1.4 SUMMARY AND GOALS

This thesis directly measured the ultrastructure and nanoscale surface properties of model HA-based biomaterials in order to elucidate processes occurring at the biomaterial-biological interface influencing bioactivity. First, surface roughness, surface charge, Hamaker constant, and adhesion forces were quantified and compared for microstructured HA, microstructured SiHA and nanostructured HA to determine effect due to Si addition and nanostructuring. Next, CaP layers were precipitated onto HA and SiHA from SBF and the surface properties of the precipitated layers were quantified and compared to the initial surfaces to determine effects of CaP layer formation, one of the initial stages of bioactivity. The effect of the bone protein osteocalcin on the formation of CaP layers was accessed though CaP precipitation from osteocalcin containing SBF. And finally, human osteoblasts were cultured on microstructured HA, nanostructured HA and a CaP precipitated layer to access osteoblast response to these three surfaces with specific differences in surface roughness and chemistry. The goal of this thesis is to illuminate bioactivity influence from surface properties measured and determine desired properties for optimal bioactivity.

1.5 REFERENCES

[1] L.L. Hench: *J Am Ceram Soc*; 81(7) (1998), p. 1705.

[2] W. Suchanek, M. Yoshimura: *J. Mater. Res.*; 13(1) (1998), p. 94.

[3] B.D. Ratner, A.S. Hoffman, F.J. Schoen, J.E. Lemons, editors. *Biomaterials science: An introduction to materials in medicine*. San Diego: Academic Press; (1996).

[4] R.Z. LeGeros, J.P. LeGeros. In: Hench LL, Wilson J, editors. *An introduction to bioceramics*. Singapore: World Scientific Publishing; (1993). p. 139.

[5] P. Ducheyne, Q. Qiu: *Biomaterials*; 20 (1999), p. 2287.

[6] W.T. Lee, M.T. Dove, E.K.H. Salje: *J Phys. Condens Matter*; 12 (2000), p. 9829.

[7] J.M. Hughes, M. Cameron, K.D. Crowley: *Am Mineral*; 74 (1989), p. 870.

[8] J. Rho, L. Kuhn-Spearing, P. Zioupos: *Med Eng Phys*; 20(2) (1998), p. 92.

[9] R.S. Lakes: *Nature*; 361 (1993), p. 511.

[10] V.A. Dubok: *Powder Metallurgy and Metal Ceramics*; 39(7-8) (2000), p. 381.

[11] J.D. de Bruijn, C.P.A.T. Klein, K. de Groot, V.C.A. van Blitterswijk: *J Biomed Mater Res*; 26 (1992), p. 1365.

[12] A.C. Guyton, J.E. Hall. *Textbook of medical physiology*. Philadelphia, PA: W.B. Saunders Co.; (1996).

[13] H.M. Kim: *Current Opinion in Solid State and Materials Science*; 7 (2003), p. 289.

[14] W. Neuman, M. Neuman. *The chemical dynamics of bone mineral*. Chicago, IL: University of Chicago Press; (1958).

[15] D. Leckband: *Annu Rev Biophys Biomol Struct*; 29 (2000), p. 1.

[16] E. Reynolds, A. Wong: *Infection and Immunity*; 39 (1983), p. 1285.

[17] P. Ducheyne, C.S. Kim, S.R. Pollack: *J Biomed Mater Res*; 26 (1992), p. 147.
[18] K. Kandori, S. Sawai, Y. Yamamoto, H. Saito, T. Ishikawa: *Colloids and Surf*; 68 (1992), p. 283.
[19] M.K.Y. Rao, R.P. Somasundaran, K.M. Schilling, B. Carson, K.P. Ananthapadmanabhan: *Colloids and Surf A*; 79 (1993), p. 293.
[20] T. Suzuki, T. Yamamoto, M. Toriyama, K. Nishizawa, Y. Yokogwa, M. Mucalo, et al.: *J Biomed Mater Res*; 34 (1997), p. 507.
[21] M.A. Lopes, F.J. Monteiro, J.D. Santos, A.P. Serro, B. Saramago: *J Biomed Mater Res*; 45 (1999), p. 370.
[22] J.C. Knowles, S. Callcut, G. Georgiou: *Biomaterials*; 21 (2000), p. 1387.
[23] P.X. Zhu, Y. Masuda, K. Koumoto: *J Colloid Interface Sci*; 243 (2001), p. 31.
[24] T. Himeno, H.-M. Kim, H. Kaneko, M. Kawashita, T. Kokubo, T. Nakamura. In: Besim Ben-Nissan DS, William Walsh, editor. *Bioceramics 15: Proceedings of the international symposium on ceramics in medicine*. Uetikon-Zuerich, Switzerland: Trans Tech Publications; (2003). p. 457.
[25] C.M. Botelho, M.A. Lopes, I.R. Gibson, S.M. Best, J.D. Santos: *J Mater Sci: Mater Med*; 13 (2002), p. 1123.
[26] W. van Raemdonck, P. Ducheyne, P. De Meester. In: Ducheyne P, Hastings G, editors. *Metal and ceramic biomaterials*. Boca Raton, Fl: CRC Press; (1984). p. 143.
[27] P.W. Brown, R.I. Martin: *J Phys Chem B*; 103 (1999), p. 1671.
[28] M. Neo, T. Nakamura, C. Ohtsuki, T. Kokubo, T. Yamamuro: *J Biomed Mater Res*; 27 (1993), p. 999.
[29] T. Kokubo, H. Kushitani, S. Sakka, T. Kitsugi, T. Yamamuro: *J Biomed Mater Res*; 24 (1990), p. 721.
[30] K. Sato, Y. Kumagai, J. Tanaka: *J Biomed Mater Res*; 50 (2000), p. 16.
[31] M. Tanahashi, T. Matsuda: *J Biomed Mater Res*; 34 (1997), p. 305.
[32] K. Yamashita, N. Oikawa, T. Umegaki: *Chem Mater*; 8 (1996), p. 2697.
[33] K.S. Hwang, J.E. Song, J.W. Jo, H.S. Yang, Y.J. Park, J.L. Ong, et al.: *J Mater Sci: Mater Med*; 13 (2002), p. 133.
[34] J. Hamagami, G. Yamaguchi, K. Kanamura, T. Umegaki: *Bioceramics*; 14 (2002), p. 279.
[35] K. Onuma, A. Ito, T. Tateishi, T. Kameyama: *J cryst growth*; 154 (1995), p. 118.
[36] J.H.C. Lin, K.H. Kuo, S.J. Ding, C.P. Ju: *J Mater Sci: Mater Med*; 12 (2001), p. 731.
[37] Y. Leng, J. Chen, S. Qu: *Biomaterials*; 24(2125-2131) (2003), p.
[38] K.A. Khor, H. Li, P. Cheang: *Biomaterials*; 24 (2003), p. 769.
[39] M. Ohgaki, T. Kizuki, M. Katsura, K. Yamashita: *J Biomed Mater Res*; 57 (2001), p. 366.
[40] T. Kobayashi, S. Nakamura, K. Yamashita: *J Biomed Mater Res*; 57 (2001), p. 477.
[41] M. Akao, H. Aoki, K. Kato: *J Mater Sci*; 16 (1981), p. 809.
[42] S.J. Eppell, W. Tong, J.L. Katz, L. Kuhn, M.J. Glimcher: *J Orthop Res*; 19 (2001), p. 1027.
[43] I.R. Gibson, S.M. Best, W. Bonfield: *J Biomed Mater Res*; 44 (1999), p. 422.
[44] I.R. Gibson, J. Huang, S.M. Best, W. Bonfield. In: Ohgushi H, Hastings GW, Yoshikawa T, editors. *Bioceramics 12: Proceedings of the international symposium on ceramics in medicine*. River Edge, N.J.: World Scientific Publishing; (1999). p. 191.
[45] F. Balas, J. Perez-Pariente, M. Vallet-Regi: *J Biomed Mater Res*; 66A (2003), p. 364.

[46] C.M. Botelho, R.A. Brooks, S.M. Best, M.A. Lopes, J.D. Santos, N. Rushton, et al. In: Barbosa MA, Monteiro FJ, Correia R, Leon B, editors. *Bioceramics 16: Proceedings of the international symposium on ceramics in medicine*. Uetikon-Zuerich, Switzerland: Trans Tech Publications; (2004). p. 845.

[47] N. Patel, S.M. Best, W. Bonfield, I.R. Gibson, K.A. Hing, E. Damien, et al.: *J Mater Sci: Mater Med*; 13 (2002), p. 1199.

[48] A.E. Porter, N. Patel, J.N. Skepper, S.M. Best, W. Bonfield: *Biomaterials*; 25 (2004), p. 3303.

[49] E.S. Ahn. Nanostructure apatites as orthopedic biomaterials [PhD Thesis]. Cambridge, MA: Massachusetts Institute of Technology; 2001.

[50] E.S. Ahn, N.J. Gleason, A. Nakahira, J. Ying: *Nano Lett*; 1(3) (2000), p. 149.

[51] T.J. Webster, C. Ergun, R.H. Doremus, R.W. Siegel, R. Bizios: *J Biomed Mater Res*; 51 (2000), p. 475.

[52] T.J. Webster, R.W. Siegel, R. Bizios: *Biomaterials*; 20 (1999), p. 1221.

[53] T.J. Webster, C. Ergun, R.H. Dormeus, R. Siegal, R. Bizios: *Biomaterials*; 21 (2000), p. 1803.

[54] L. Bottomley: *Anal Chem*; 70 (1998), p. 425R.

[55] L. Haggerty, A. Lenhoff: *Biotechnol Prog*; 9 (1993), p. 1.

[56] K. Jandt, M. Finke, P. Cacciafesta: *Colloids Surf B: Biointerfaces*; 19 (2000), p. 301.

[57] K. Merrett, R.M. Cornelius, W.G. McClung, L.D. Unsworth: *J Biomater Sci, Polym Ed*; 13 (2002), p. 593.

[58] P.P. Lehenkari, G.T. Charras, S.A. Nesbitt, M.A. Horton. *New technologies in scanning probe microscopy for studying molecular interactions in cells*: Cambridge University Press; (2000).

[59] J. Kirkham, S.J. Brookes, R.C. Shore, W.A. Bonass, D.A. Smith, M.L. Wallwork, et al.: *Connect Tissue Res*; 38 (1998), p. 91.

[60] J. Zhang, J. Kirkham, M.L. Wallwork, D.A. Smith, J. Brookes, R.C. Shore, et al.: *Langmuir*; 15 (1999), p. 8178.

[61] K. Onuma, A. Ito, T. Tateishi, T. Kameyama: *J Cryst Growth*; 148 (1995), p. 201.

[62] L. Siperko, W. Landis: *Appl Phys Lett*; 61 (1992), p. 2610.

[63] L. Siperko, W. Landis: *Analyst*; 119 (1994), p. 1935.

[64] J. Seog, D. Dean, A.H.K. Plass, S. Wong-Palms, A.J. Grodzinsky, C. Ortiz: *Macromolecules*; 35(14) (2002), p. 5601.

[65] J. Fitz, D. Anselmetti, J. Jarchow, X. Fernandez-Busquets: *J Struct Biol*; 119 (1997), p. 167.

[66] M. Benoit, D. Gabriel, G. Gerisch, H. Gaub: *Nature Cell Bio*; 2 (2000), p. 313.

[67] H.-J. Butt, B. Cappella, M. Kappl: *Surf Sci Rep*; (2005), p.

[68] M. Radmacher, J.P. Cleveland, M. Fritz, H.G. Hansma, P.K. Hansma: *Biophys J*; 66 (1994), p. 2159.

[69] A. Noy, D.V. Vezenov, C.M. Lieber: *Annu Rev Mater Sci*; 27 (1997), p. 381.

[70] D.A. Smith, C. Robinson, J. Kirkham, J. Zhang, M.L. Wallwork: *Rev Anal Chem*; 20 (2001), p. 1.

[71] D.A. Smith, S.D. Connell, C. Robinson, J. Kirkham: *Anal Chim Acta*; 479 (2003), p. 39.

[72] E.J.W. Verwey, J.T.G. Overbeek, K.V. Nes. *Theory of the stability of lyophobic colloids*. New York: Elsevier Publishing Company; (1948).

[73] J. Israelachvili. *Intermolecular and surface forces*. second ed. Amsterdam: Academic Press; (1991).
[74] P.D. Ashby, L. Chen, C.M. Lieber: *J Am Chem Soc*; 122 (2000), p. 9467.
[75] T. Ederth: *Langmuir*; 17 (2001), p. 3329.
[76] O. Devereux, P.L. de Bruyn. *Interaction of plane-parallel double layers*. Cambridge, MA: MIT Press; (1963).
[77] A. Sanfeld. *Thermodynamics of charged and polarized layers*. Bath, UK: Wiley-Interscience; (1968).
[78] J. Cleveland. In. p.
[79] V.A. Parsegian, D. Gingell: *Biophys. J.*; 12 (1972), p. 1192.
[80] H.J. Butt: *Biophys. J.*; 60 (1991), p. 1438.
[81] G.E. Forsythe, W.R. Wasow. *Finite difference methods for partial differential equations*. New York: John Wiley and Sons, Inc.; (1960).
[82] P. Hiemenz, R. Rajagopalan, editors. *Principles of colloid and surface chemistry*. Third ed. New York: Marcel Dekker, Inc.; (1997).
[83] C. Werner, R. Zimmermann, T. Kratzmuller: *Colloids and Surf A*; 192 (2001), p. 205.
[84] M. James, R.J. Hunter, R.W. O'Brien: *Langmuir*; 8(2) (1992), p. 420.
[85] S. Chander, D.W. Fuerstenau. In: Misra D, editor. *Adsorption on and surface chemistry of hydroxyapatite*. New York: Plenum Press; (1982).
[86] P. Somasundaran: *J Colloid Interface Sci*; 27 (1968), p. 659.
[87] G. Toikka, R.A. Hayes, J. Ralston: *Langmuir*; 12 (1996), p. 3783.
[88] H.G. Pedersen, L. Bergstrom: *J Am Ceram Soc*; 82(5) (1999), p. 1137.

CHAPTER 2: Variation of Nanoscale Surface Charge of Synthetic Polycrystalline Hydroxyapatite

2.1 INTRODUCTION

Hydroxyapatite (HA) ($Ca_5(PO_4)_3OH$) is being investigated in a wide variety of forms for use in different bone implant applications [1-4]. The nanoscale surface chemical properties (e.g. surface functional groups, charge distribution), and morphological structure (e.g. grain size, shape, distribution, roughness) will critically influence the implant's interaction with the biological environment, and how well the implant subsequently performs *in vivo* [5]. It is expected that surface charge will have a strong influence on the processes of inorganic and organic deposition and structural evolution on the implant material, especially in the initial stages of implantation. Reports of increased crystal growth of bone-like HA [6], cell adhesion [7], and osteobonding [8] to negatively charged surfaces of electrically polarized HA support this hypothesis. Also, Si-substituted HA (SiHA) has been shown to have improved bioactive properties both *in vitro* and *in vivo*, [9-11] which has been suggested to be due to increased negative surface charge from substitution of PO_4^{3-} groups with more negative SiO_4^{4-} groups [9]. Zeta potential measurements of HA performed near physiological pH, but at varied IS, have found varied surface potentials from -50 mV [9] to 3 mV [12], although the majority of measurements have been between -5 and -20 mV [12-20]. Ionic strength of measurement solution, substituted impurities, phase impurities, Ca-deficiency, and lattice defects could all be possible causes for variation [12,16,21]. Negative surface charge of HA is thought to arise from the preferential concentration of PO_4^{3-} groups to the top few nanometers [9] of the surface [2,22]. This Ca deficient surface layer (Ca/P ratio ~1.5 [22]) is expected to be caused by solid-solution equilibrium during the precipitation process [22].

Typically, surface charge is measured via the zeta potential method [23-25] which yields an averaged, bulk value for colloidal dispersions, fibers, films, and other microscopic structures. Here, the complementary and relatively new technique of chemically-specific high resolution force spectroscopy (HRFS) [26] is employed, which allows for the direct measurement of piconewton (pN) level forces in fluid between a nanosized probe tip functionalized with molecules of uniform and known structure, chemistry, and charge (e.g. self-assembling monolayers (SAMs)) as a function of separation distance from a sample of interest. By comparing HRFS data on approach of the probe tip to the sample surface to appropriate electrostatic double layer theory [27-29], an estimation of the surface charge per unit area, σ (C/m^2), of the sample of interest can be made. Here, the normal electrostatic double layer forces between COO^- and NH_3^+-terminated alkanethiol SAM-functionalized probe tips and dense, polycrystalline, phase pure synthetic HA were measured via chemically specific HRFS with new nanomechanical instrumentation [30] that allows for both high resolution topographic imaging and HRFS with nanoscale spatial resolution. Nanomechanical data on approach was compared to the nonlinear Poisson-Boltzmann-based electrostatic double layer theory for surfaces of constant surface charge to predict σ_{HA} (C/m^2) as a function of ionic strength (IS), position within a variety of grains, and across grain boundaries. This new methodology allows for precise and positionally sensitive measurement of nanoscale surface properties that control bioactivity.

2.2 MATERIALS AND METHODS

2.2.1 Sample Preparation and Characterization

Synthetic HA was prepared as described in **Section 1.2.1**. Purity of the HA pellets was determined via Wide Angle X-ray Diffraction (WAXD) using a *Philips* PW1710 X-ray diffractometer and X-ray fluorescence spectroscopy (XRF) using a *Philips* PW1606 spectrometer. Surface wettability was assessed via contact angle measurements with DI water using a Video Contact Angle System 2000 (*AST, Inc.*) Grain size analysis, via grain diameter measurements, was performed using a *FEI/Philips* XL30 FEG environmental scanning electron microscopy (ESEM). To prepare samples for ESEM, the HA pellet was polished to a 3 μm finish using an aluminum oxide film on a uni-pol polisher (*Geoscience Instruments Corp.*) and then etched in 10% H_3PO_4 for 10 seconds. Three SEM images of different sites were then taken at 10,000× and these images were analyzed using Scion Image (*Scion Corporation*) to determine grain size and distribution. Surface topography was imaged using a *Veeco* (*Digital Instruments)* Nanoscope IIIA System Controller with Multimode Atomic Force Microscope (AFM) in contact mode in air with a *Thermomicroscopes* Si_3N_4 V-shaped cantilever with a spring constant (k_c) ~ 0.01 N/m.

2.2.2 Chemically-Specific HRFS with SAMs

2.2.2.1 Preparation of Probe Tips

HRFS experiments were performed with Au-coated [31] Si_3N_4 cantilever probe tips chemically functionalized with alkanethiol SAMs terminated with either COO^- groups (11-Mercaptoundecanoic acid, HS-$(CH_2)_{10}$-COOH, *Aldrich*) or NH_3^+ groups (11-aminoundecanethiol, HS-$(CH_2)_{11}$-NH_3, *Dojindo Laboratories*) prepared and characterized as described in **Section 1.3.2.2**.

2.2.2.2 Averaged (Blind) HRFS

HRFS experiments were conducted using a 1-D Molecular Force Probe (1DMFP, *Asylum Research, Inc.*) to measure force, F (nN), versus tip-sample separation distance, D (nm), on approach and retract (F-D curves). A full description of this instrument, its limits, procedures for spring constant calibration and raw data conversion, and details of measurement errors are given in previous work [31]. HRFS experiments were performed using two cantilevers (*Thermomicroscopes*, V-shaped, spring constant = 0.01 N/m); one with a COO^--terminated SAM probe tip (R_{TIP} =64 nm) and the other with a NH_3^+-terminated SAM probe tip (R_{TIP} =37.5 nm). HRFS experiments for the COO^--terminated SAM probe tip (pKa(COOH)~4.75) were carried out in aqueous electrolyte solutions having ionic strengths (IS) of 0.001M-1M NaCl and constant pH~6, which were prepared by dissolving NaCl crystals in DI water. An equilibration time of 20 minutes was allowed during solution changes and the order of experiments was from low to high IS. HRFS experiments for the NH_3^+-terminated SAM probe tip ($pKa(NH_2)$~5.5) were carried out in aqueous electrolyte solutions having IS of 0.01M-1M formate buffer, pH~4, prepared by mixing formic acid ($HCHO_2$) with DI water and adding NaCl crystals to get desired IS. Both NaCl and formate buffer produce monovalent electrolyte solutions. The probe tip-surface force as a function of tip-sample separation distances on approach and retract was measure at a z-piezo displacement rate of 2 μm/s. HRFS experiments of these probe tips were first conducted on Au-coated Si substrates [31] functionalized with the same SAM as the probe tip in varied IS solutions of constant pH (pH~6 for COO^--terminated SAM and pH~4 for NH_3^+-terminated SAM) to determine surface charge per unit area of the SAM and then these probe tips of known charge were used to probe an HA sample. Approximately 30 individual HRFS probes were performed and averaged at each of three random locations on the samples of interest.

2.2.2.3 Positionally Specific HRFS

HRFS was additionally performed using a 3-D Molecular Force Probe (3DMFP, *Asylum Research, Inc*) which has all the same features as the 1DMFP but additional capabilities to image the surface and perform positionally sensitive HRFS in the plane of the sample surface. An Au-coated Si_3N_4 cantilever probe tip (Thermomicroscopes, V-shaped, spring constant =0.03 N/m, R_{TIP} =89 nm) chemically functionalized with COO^--terminated SAM was prepared and characterized as described in **Section 1.3.2.2**. This probe tip was used to image and probe an HA sample simultaneously within a variety of grains and across grain boundaries in order to compare forces to observed topographical surface features. The experiment was carried out in 0.01M NaCl solution (pH~6). The probe tip-surface forces as a function of tip-sample separation distance were measured on approach and retract at a z-piezo displacement rate of 2 μm/s. Approximately 5 individual HRFS probes were performed and averaged at each position.

2.2.2.4 Theoretical Predictions

HRFS data on approach was compared to the numerical solutions of the full nonlinear electrostatic double layer theory based on a Poisson-Boltzmann (P-B) formulation for a surface of constant charge per unit area [27-29] as described previously in **Section 1.3.2**. In this case the van der Waals component was not included in theoretical fits, but due to its small magnitude, inclusion of it resulted in a minimal different in the estimated surface charge density (<5%). For the 1DMFP experiments, control HRFS experimental data of the COO^--terminated SAM probe tip versus a COO^--terminated SAM planar substrate were compared to the theory (data not shown) and σ_{COO-} was estimated to be -0.0084 C/m^2 where the fixed parameters in the analysis were R_{TIP} and the IS. Analogous NH_3^+-terminated SAM HRFS experiments and theoretical fits (data not shown) yielded $\sigma_{NH3+} = +0.0207\ C/m^2$. For the 3DMFP experiment, σ_{COO-} of -0.0178 C/m^2 was used. These probe tips of known σ were used to test HA in varied IS solutions and experimental data was fit to the theoretical solution using σ_{HA} as the only free fitting variable.

2.3 RESULTS

2.3.1 General Characterization: WAXD, Contact Angle, ESEM, and AFM

WAXD demonstrated the HA pellets to be phase pure while XRF analysis confirmed that the pellets had a bulk Ca/P molar ratio of approximately 1.67 and did not reveal any unexpected elements. Instantaneous contact angle measurements with DI water gave an averaged contact angle (75 ± 2°, *n*=6). Grain size analysis was performed on the ESEM images (**Fig. 2.1A**) where the diameter of every distinct grain on three separate digital images was measured, for a total of 93 grains. The grain size distribution (**Fig. 2.1B**) was found to have a mean value of 1.48 ± 0.68 μm. Five 5 μm × 5 μm contact mode AFM (CMAFM) deflection images were also analyzed which encompassed several grains. The grain sizes determined via CMAFM images agreed well with the ESEM images where 28 separate grains were measured giving an average size of 1.17 ± 0.76 μm. The average root mean squared (RMS) surface roughness of the five 5 μm scans was 113.6 ± 21.0 nm, which takes into account several grains and grain boundaries. Additional smaller scans inside 5 different grains were performed in order to quantify the surface roughness inside the grains and the average RMS surface roughness was found to be 17.9 ± 3.2 nm. Typical AFM images are shown in **Fig. 2.2**.

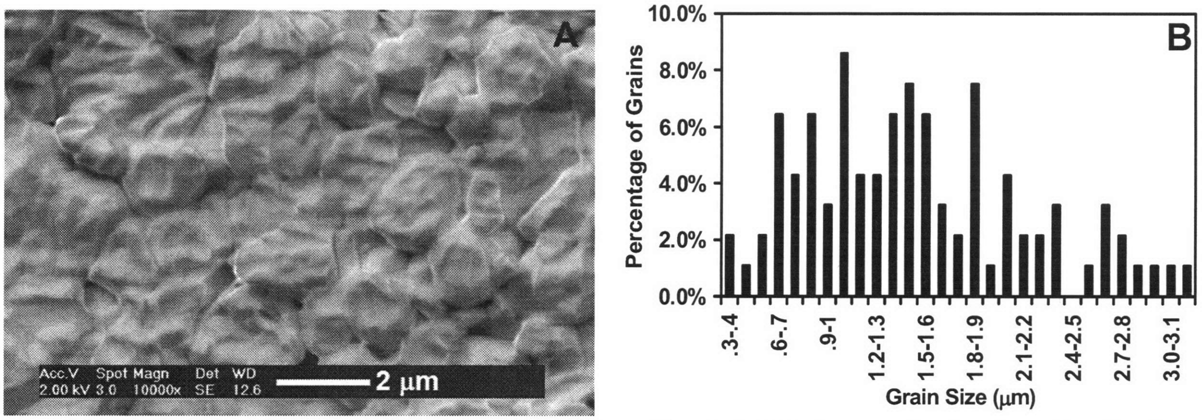

Figure 2.1: A) ESEM image of acid etched HA pellet (10,000×). **B)** Grain size distribution of acid etched HA pellet (1.48 ± 0.68 μm).

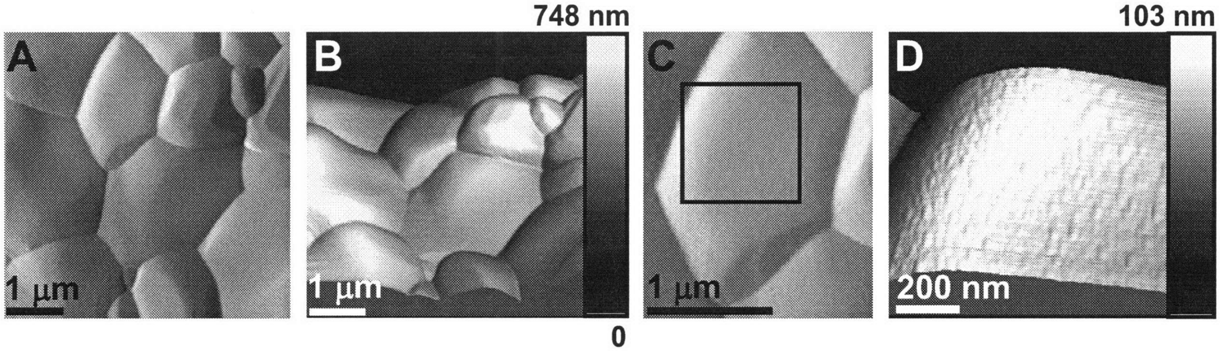

Figure 2.2: CMAFM images of as-received HA pellet taken in air **A)** 2-D deflection image **B)** 3-D height image of image shown in A). **C)** 2-D deflection image of single grain in image A). **D)** 3-D height image of intragranular surface inside square of in the image shown in part C)

2.3.2 Chemically-Specific HRFS: Charged SAM Probe Tips versus HA

2.3.2.1 Averaged (Blind) HRFS with 1DMFP

The averaged approach force-distance (F-D) curves with standard deviations for the COO^--terminated SAM probe tip versus an HA pellet surface at pH~6 and varied IS (**Fig. 2.3A**) all show purely repulsive, nonlinear forces on approach of the probe tip to the HA surface. The repulsive forces observed in the 0.1M and 1M IS solutions are observed to be significantly less in both magnitude and range than the lower IS solutions of 0.01M and 0.001M. The averaged F-D curves with standard deviations for the NH_3^+-terminated SAM probe tip versus HA at pH~4 and varied IS (**Fig. 2.3B**) all show an attractive, nonlinear force that begins at increasingly smaller distances from the sample surface with increasing IS, i.e. 10.8 nm, 9.2 nm, and 6.9 nm at 0.01M, 0.1M, and 1M IS respectively and exhibit minimum values of $F/R_{TIP} \sim 0.20$ mN/m, ~ 0.17 mN/m, and ~ 0.25 mN/m at D ~ 3.4 nm, D ~ 3.7 nm, and D ~ 1.9 nm respectively. These results clearly suggest an electrostatic double layer origin for the surface interaction force with the HA possessing a net negative surface charge. One observation of note was that the variance in the HRFS data for the COO^--terminated SAM probe tip with position on the HA surface (**Fig. 2.4A**) was significantly greater than the variance of HRFS curves with position on the COO^--

terminated SAM (**Fig. 2.4B**). Hence, the effect of position was investigated further using the 3DMFP and discussed in the following section.

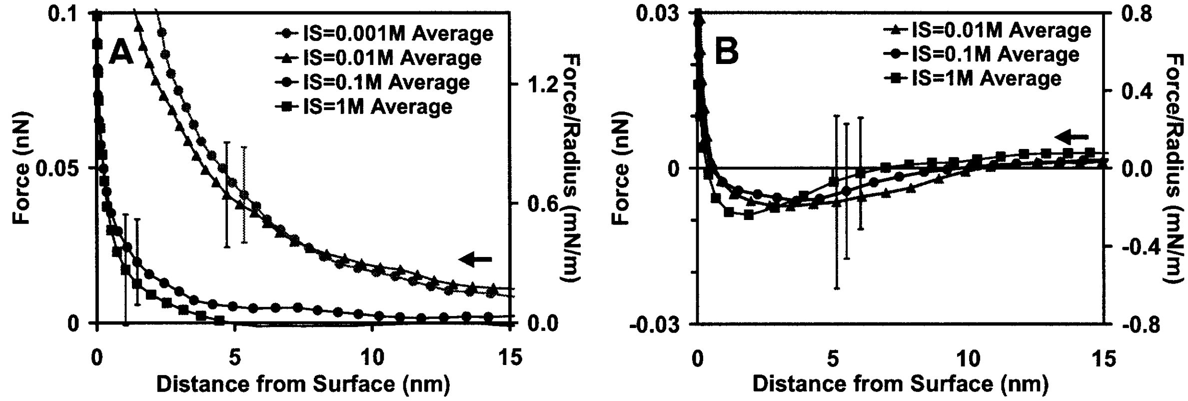

Figure 2.3: 1DMFP HRFS data. Averaged (n=90 curves, 30 each at 3 positions) approach F-D curves with standard deviation probing HA as a function of IS with: **A)** COO^{-}-terminated SAM probe tip (R_{TIP}=64 nm, pH ~ 6) and **B)** NH_3^+-terminated SAM probe tip (R_{TIP}=37 nm, pH ~ 4).

In order to estimate σ_{HA}, the averaged HRFS curves shown in **Fig. 2.4** (each for one position) were fit to the numerical solution of P-B theory for surfaces of constant charge per unit area using the following fixed parameters; surface charge of probe tips (σ_{COO-} = -0.0084 C/m^2 or σ_{NH3+} = +0.0207 C/m^2), IS=0.01M, R_{TIP} (R_{TIP}(COO-) =64 nm or $R_{TIP}(NH_3^+)$ =37 nm). σ_{HA} (C/m^2) was the only free variable fitting parameter [34]. HRFS data of the COO^{-}-terminated SAM probe tip vs. HA in 0.01M IS fit reasonably well to theoretical P-B theory as shown in **Fig. 2.5A** which yielded a best fit parameter of σ_{HA} = -0.0050 C/m^2. HRFS data of a NH_3^+-terminated SAM probe tip vs. HA in 0.01M IS solution, through comparison with P-B theory, yielded a similar result of σ_{HA} = -0.0048 C/m^2 (**Fig. 2.5B**).

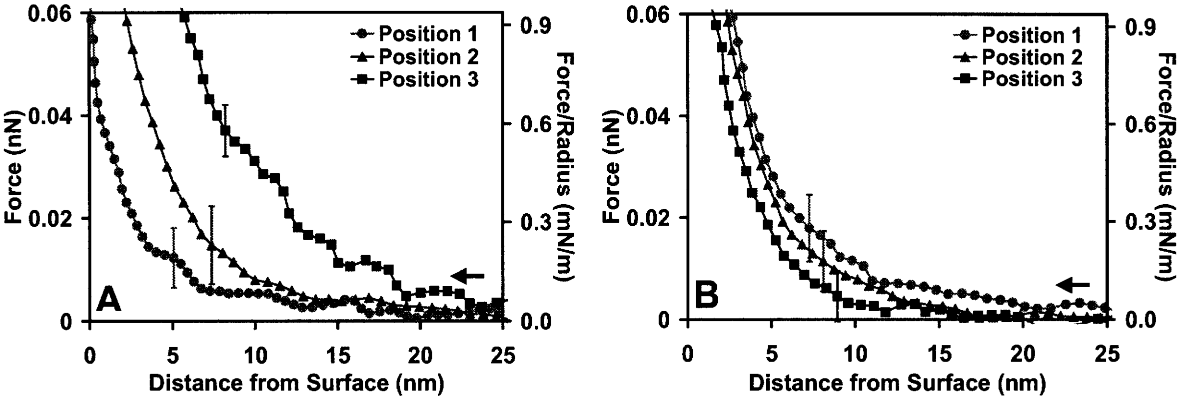

Figure 2.4: 1DMFP HRFS data. Averaged (n=30) approach F-D curves with standard deviation for COO$^-$-terminated SAM probe tip at 3 randomly selected positions (R_{TIP} =64 nm, pH ~ 6, IS=0.01M) probing: **A)** HA and **B)** COO$^-$-terminated SAM planar surface.

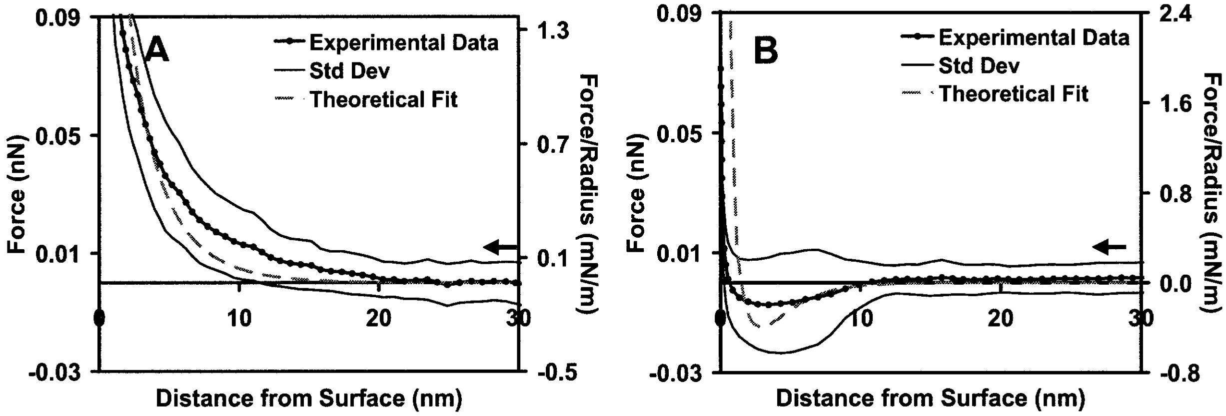

Figure 2.5: 1DMFP HRFS data. **A)** Averaged (n=90 curves, 30 each at 3 positions) approach F-D curve for COO$^-$-terminated SAM probe tip versus HA (pH~6) and P-B theoretical fit (fixed parameters: σ_{COO^-} = -0.0084 C/m^2, IS=0.01M, R_{TIP} =64 nm; best fit parameter, σ_{HA} = -0.005 C/m^2). **B)** Averaged approach F-D curve for NH$_3^+$-terminated SAM probe tip versus HA (pH~4) and P-B theoretical fit (fixed parameters: σ_{NH3+} = +0.0207 C/m^2, IS=0.01M, R_{TIP} =37 nm; best fit parameter, σ_{HA} = -0.0048 C/m^2).

The retract F-D curves were also examined and the average adhesion forces and distances with standard deviations for the COO$^-$-terminated SAM probe tip probing HA at varied solution IS were calculated (**Fig. 2.6**). The adhesion force magnitudes at 0.1M and 1M are statistically lower ($p<0.01$) than the adhesion force magnitudes at 0.001M and 0.01M although the forces between 0.1M and 1M were not statistically different, nor were the forces between 0.001M and 0.01M. The adhesion pull-off distances ranged up to 60 nm and were also statistically lower

($p<0.01$) at higher IS except for 0.001 compared to 0.01. The Derjaguin-Muller-Toporov elastic contact mechanics theory [32,33] can provide an upper limit estimate for the number of molecular contacts that exist at the maximum compressive force and contribute to the adhesive interaction. The elastic contact area between the probe tip and a planar surface, $A_{contact}=\pi a^2$, can be calculated from a, the elastic contact area radius, as follows:

$$a=\left(\frac{(F+F_{adhesion})R_{TIP}}{K}\right)^{1/3}, \quad K=\frac{4}{3}\left(\frac{1-\nu_1^{\,2}}{E_1}+\frac{1-\nu_2^{\,2}}{E_2}\right)^{-1} \qquad (2.1)$$

where K = the reduced elastic modulus, ν = Poisson's ratio, E = Young's (elastic) modulus, $E_1(Au)$ = 64 GPa, $\nu_1(Au)$ = 0.44, $E_2(HA)$ = 95 GPa, and $\nu_2(HA)$ = 0.28. Taking a maximum compressive force of ~1 nN at D=0 and a maximum observed adhesive force also of ~1 nN, $A_{contact}$ was found to be ~5.2 nm^2 for the 64 nm radius COO$^-$-terminated SAM probe tip used for the 1DMFP experiments. Since the area per SAM molecule is approximately 0.216 nm^2 [34], the number of molecules within the maximum elastic contact area corresponds to 24. Hence, the maximum adhesive force per SAM molecule within this elastic contact area is ~42 pN, an upper limit since the contact radius will decrease from the maximum value before piezo reversal and upon retract, as well as the fact that the adhesion force taken was the maximum observed.

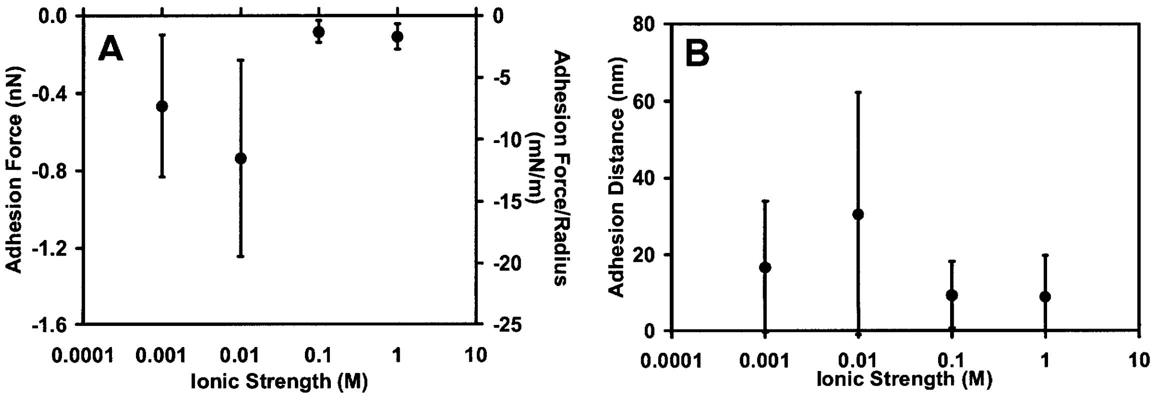

Figure 2.6: Analysis of 1DMFP HRFS retract data (R_{TIP}=64 nm, pH ~ 6) **A)** Averaged (n=30) adhesion forces and **B)** Averaged (n=90 curves, 30 each at 3 positions) adhesion distances on retract between COO$^-$-terminated SAM probe tip and HA at varied solution IS.

2.3.2.2 Positionally Specific Surface Force Analysis with the 3DMFP

As mentioned previously, when performing HRFS experiments with the 1DMFP, a variance in the experimental data with position on the HA surface was noticed which was significantly greater than the variance of HRFS curves with position on the COO^--terminated SAM (**Fig. 2.4**). Hence, further investigation was carried out with the 3DMFP where AFM imaging and HRFS could both be performed together, making it possible to correlate intersurface forces with topographical features. The first set of HRFS experiments (labeled Scan 1) traversed 3 different grains on the HA surface corresponding to the positions shown as "X's" in the CMAFM deflection (topographical) image given in **Fig. 2.7A**. Underneath the AFM image in **Fig. 2.7A**, a topographical profile of the surface height versus horizontal distance across the image (corresponding to the horizontal black line in the top image of **Fig. 2.7A**) is given and shows the surface geometry of the probed area. A second smaller scan (labeled Scan 2) was made at the grain boundary between probe position 5 and 6 of Scan 1, and the surface locations of the HRFS experiments taken across the grain boundary are shown as "X's" in **Fig. 2.7B**. **Fig. 2.7C** shows the averaged (n=5) approach F-D curves with standard deviation for the probe positions of Scan 1. **Fig. 2.7D** shows the averaged approach F-D curves with standard deviation for the probe positions of Scan 2. Position 5 on Scan 1 and position 1 on Scan 2 probe the same topographical face. The probe at point 4 on Scan 2 showed unusual nanomechanical behavior, most likely due to geometric and interlocking effects between the probe tip and the grain boundary. A positional variance of the surface forces was observed in both of these datasets and the data was analyzed in this context. In particular, the positions were grouped by facet as shown in **Fig. 2.8**, where a facet was defined as a distinct topographical face whose area had a relatively constant slope.

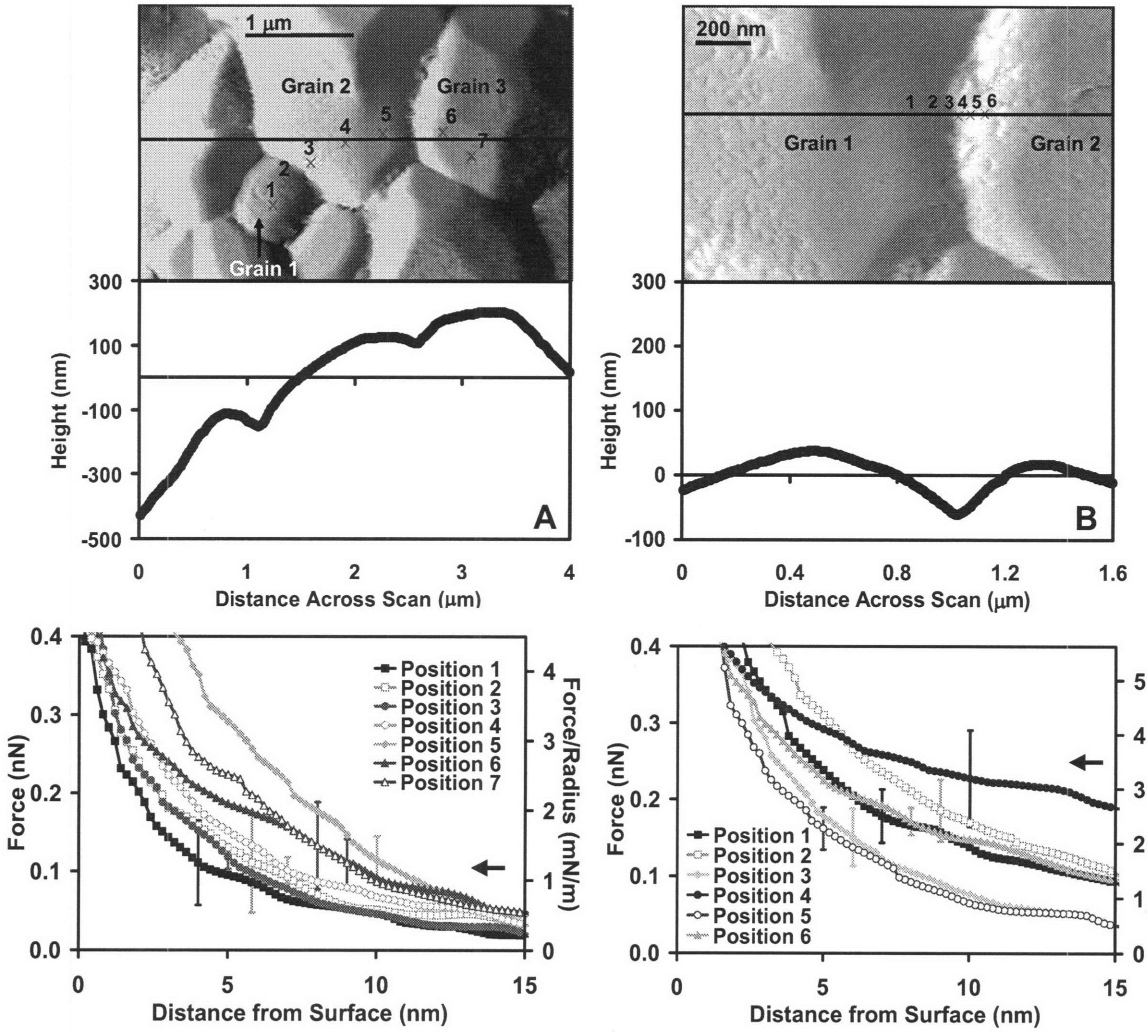

Figure 2.7: **A)** Scan 1 CMAFM deflection image taken using 3DMFP with COO^--terminated SAM probe tip in aqueous electrolyte (R_{TIP} =89 nm, IS=0.01M, pH ~6) showing specific positions (X's) probed and height profile along the solid black line in the image. **B)** Scan 2 CMAFM deflection image taken using 3DMFP with COO^--terminated SAM probe tip in aqueous electrolyte (R_{TIP} =89 nm, IS=0.01M, pH~6) showing specific positions (X's) probed and height profile along the solid black line in the image. **C)** Averaged (n=5) approach F-D curves with standard deviation of 7 probe locations shown in A). **D)** Averaged (n=5) approach F-D curves with standard deviation of 6 probe locations shown in B). Hi-lo bars represent one standard deviation.

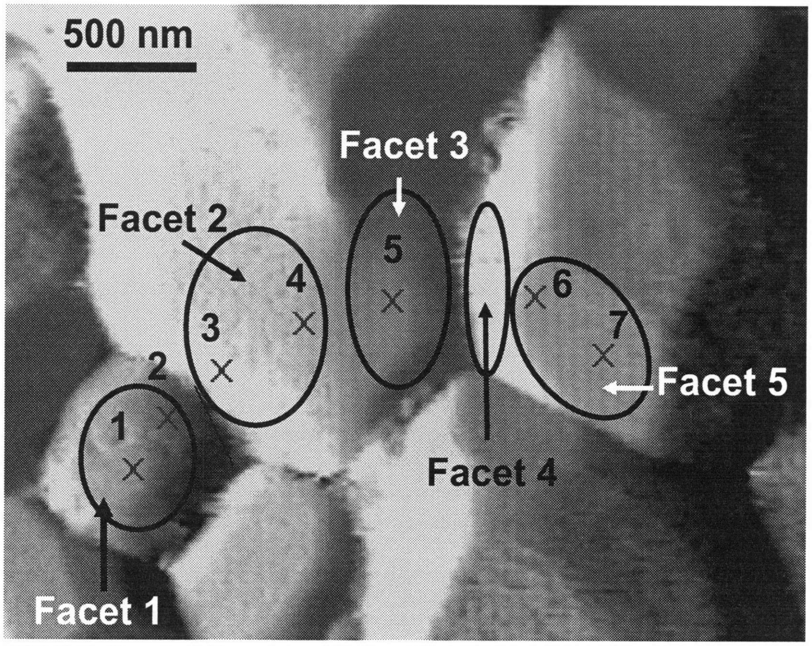

Figure 2.8: CMAFM deflection image taken using 3DMFP with COO^--terminated SAM probe tip in aqueous electrolyte (R_{TIP} =89 nm, IS=0.01M, pH~6) showing the different facets among the grains imaged.

Generally, the 3DMFP HRFS data and the 1DMFP HRFS data taken at 0.01M IS were consistent in magnitude and range, even using different probe tips where variations always arise due to geometry and other nanoscale factors such as variations in surface roughness, SAM density, etc. The 3DMFP data shows slightly larger F/R_{TIP} correlating with a higher probe tip surface charge density than that used for the 1DMFP.

Using the same process as for the 1DMFP data, the 3DMFP HRFS data on approach was compared to electrostatic double layer theory and σ_{HA} for each position was calculated by averaging the fitted σ_{HA} for three individual curves at that position. **Fig. 2.9A** and **B** show the averaged σ_{HA} for each probe position for Scans 1 and 2 respectively, along with standard deviations. The σ_{HA} of each facet was examined since facets likely have different exposed crystallographic planes with differing numbers of exposed charged groups causing σ_{HA} variations. Statistical analysis shows the average σ_{HA} for each facet to be significantly different from the others in 9 out of 10 comparisons ($p<0.05$). The average σ_{HA} over all positions in both scans was calculated in this experiment to be -0.019 ± 0.020 C/m^2. The magnitude of the force and hence, the fitted value of σ_{HA}, showed variations within individual grains, between differing grains, and across the grain boundary. **Fig. 2.9C** shows σ_{HA} versus the distance of the probe position from the grain boundary (left side of grain boundary, including data from both scans). A linear regression of these data points gives a R^2 correlation factor of >98% which is statistically significant ($p<0.05$) and a slope of -0.19 C/m^2 per μm. This trend is consistent with surface charge being due to ion arrangements in crystallographic planes which become disordered and shifts from one plane to another at grain boundaries.

Since the surface charge calculation is based on an approximated fit to the HRFS data, specific data from each individual curve was also examined. The force between the probe tip and HA at one Debye length away from the surface (κ^{-1}=3 nm) was recorded for each curve (n=5) at each position in each scan (data not shown). An increase in this force would indicate a larger surface charge per unit area if the force is caused mainly by electrostatics. The trends for surface charge and force between the probe tip and HA at one Debye length away from the surface were consistent.

Similar to the 1DMFP data, the retract F-D curves were also examined and the average adhesion forces and distances for the COO^--terminated SAM probe tip probing HA were recorded. The average adhesion force magnitudes and the adhesion pull-off distances were similar to the values obtained from the 1DMFP experiment and although they differed per facet there were no obvious correlations with surface charge. Similar to the 1DMFP experiments, $A_{contact}$ was calculated to be ~6.5 nm^2 for the 89 nm radius COO^--terminated SAM probe tip used for the 3DMFP experiments, corresponding to 30 SAM molecules and a maximum adhesive force per SAM molecule of 33 pN.

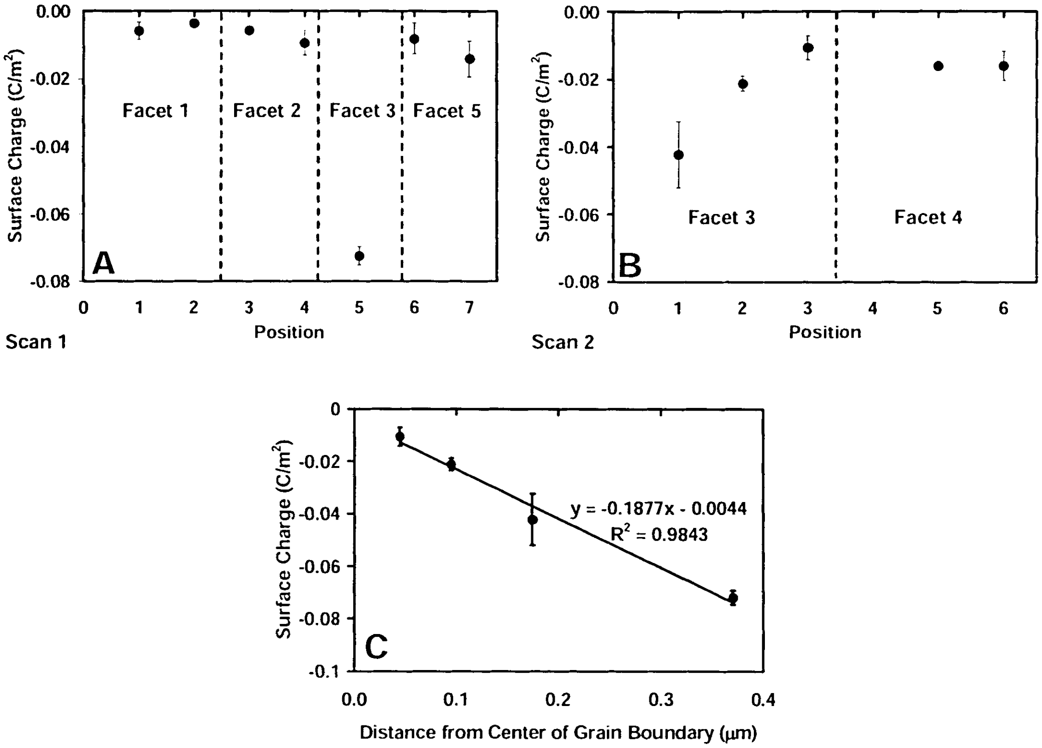

Figure 2.9: Surface charge determined from 3DMFP HRFS data via comparison to P-B electrostatic double layer model (fixed parameters: σ_{COO^-} = -0.0178 C/m^2, IS=0.01M, R_{TIP} =89 nm, pH~6). **A)** Averaged (n=3) surface charge calculated from fitting individual approach F-D curves for each probe position on scan 1 shown in **Fig. 2.7A** to P-B theoretical model. **B)** Averaged (n=3) surface charge calculated from fitting HRFS data at each specific probe position on scan 2 shown in **Fig. 2.7B** to the P-B theoretical model. **C)** Linear regression of surface charge density to the left of the grain boundary between facet 3 and 4. Hi-Lo bars represent one standard deviation.

2.4 DISCUSSION

It has been shown that the sensitive and powerful nanomechanical technique of chemically and spatially specific high resolution force spectroscopy can measure the nanoscale forces that exist at the interface between a biomaterial surface and physiological fluids. Nanosized probe tips of known chemistry and geometry were used to test a common bone implant material, i.e. phase pure, dense, polycrystalline synthetic hydroxyapatite, and fits of these data on approach to electrostatic double layer theory [27-29] enabled approximation of the HA surface charge per unit area, σ_{HA}. On retract of the probe tip away from the surface, nanoscale adhesive interaction forces, $F_{adhesion}$, were measured. One of the most unique aspects of this methodology is that it allows for the determination of local nanoscale variations in σ_{HA} and $F_{adhesion}$ within grains and across grain boundaries, important information unable to be obtained by other standard techniques such as zeta potential measurements. Nanoscale variations in the local interface potential are certain to affect the adsorption process of ions and biomolecules, the formation of calcium phosphate (CaP) layers, and interactions with various cells which determine the build up of interfacial layers that bond the bone tissue to the implant material. With these new capabilities, the relation of such local nanoscale parameters to bioactivity can be explored, for example by correlating σ and $F_{adhesion}$ measured by HRFS measurements with the kinetics of CaP layer growth when the same samples are incubated in simulated body fluid (SBF) or implanted *in vivo*. In addition, chemically specific HRFS will be able to detect at the differences in nanoscale surface properties between the original HA surface and precipitated CaP layers from SBF. Lastly, the same experimental and theoretical methodology can be used for studying the nanoscale interactions between biomaterial surfaces and proteins and cells since the nanosized probe tips can be functionalized accordingly. Overall, it is clear that this method holds great potential for fundamental research on the physicochemical processes occurring at biomaterial interfaces and elucidating the molecular origins of bioactivity. Following, is a discussion of specific aspects of the data.

2.4.1 Approach HRFS Data

All trends in HRFS experimental data with IS and theoretical fits support the fact that on approach the intersurface interaction is dominated by electrostatic double layer forces and that HA has a net negative surface charge per unit area, σ_{HA}, ranging from -0.0037 – -0.072 C/m^2 with an average value of -0.019 C/m^2. The net negative surface charge of HA is consistent with previous reports in the literature [9,14,19,35] and as mentioned previously, has been suggested to be due to preferential surface migration of PO_4^{3-} groups [2,22]. Jump to contacts, although not numerous, were noticed but in this case the van der Waals component was not included in theoretical fits. Due to its small magnitude, inclusion of it resulted in a minimal different in the estimated surface charge density (<5%). In the next chapter when HA is compared to SiHA, Hamaker constants for both surfaces are calculated and the van der Waals component is included in theoretical fits.

2.4.2 Spatial Heterogeneity of Surface Charge of HA

Geometrical calculations have ruled out the variance in apparent surface charge being due to the slope of the sample surface (**Appendix A**). Unlike SAM layers, the HA pellets do not present a uniform charge over its surface but is locally (at the nanoscale level) heterogeneous, likely due to different arrangements of ions in the HA crystal structure. The degree to which these nanoscale heterogeneities are relevant to Ca^{2+} binding, CaP precipitation, protein adsorption, and ultimately biocompatibility is discussed in chapters 5-7.

2.4.3 Relation of HRFS Data to Zeta Potential

Once the full nonlinear P-B equation is fit to the experimental data, the surface potential can be calculated by setting D=0 and solving the P-B equation. The surface potential calculated in this way is equivalent to zeta potential [23]. Until recently, the majority of surface charge measurements have been accomplished through zeta potential measurements. Zeta potential is dependant on surface charge density and is defined as the electrostatic potential at the hydrodynamic shear plane which is the boundary between a layer of more rigidly bound counterions and the diffuse electrostatic double layer of highly mobile, hydrated counterions [23]. Zeta potential measurements are averaged, bulk measurements and have the variability of particle size [19,36] and IS dependence [23]. When the surface potential is calculated from the average surface charged measured by 3DMFP, $\sigma_{HA} = -0.019$, a value of -64 mV is obtained. The negative sign for surface charge of phase pure HA measured here is in agreement with the majority of zeta potential measurements of HA in the literature that vary from -50 mV [9] to 3 mV [12] with the majority between -5 and -20 mV [12-20]. The magnitude is a bit higher than the literature but zeta potentials measured by microelectrophoretic and other techniques are expected to be lower, 30-50%, than fitted potentials for nanomechanical data ideal (smooth) surfaces [37] because of the potential drop in the immobilized liquid layer close to the surface [38]. A more detailed comparison between HRFS and zeta potential is given in **Section 1.3.2.3**. The surface charge calculated here via HRFS data compared to P-B theory is the effective charge at the Stern surface since electrostatic double layer theory is valid only within the diffuse double layer that begins at the Stern surface [23]. The HRFS surface charge model should closely resemble the electrostatic interaction of a biomacromolecule or cell approaching a biomaterial surface, where the effective charge at the Stern surface is what the biomacromolecule or cell feels inside the diffuse double layer.

2.4.4 Retract HRFS Data

Both the 1DMFP and 3DMFP data produced similar adhesion forces and distances, with a maximum adhesive force per SAM molecule of 42 pN, clearly typical of a noncovalent interaction (e.g. hydrogen bonding, van der Waals, or ionic). The adhesion forces measured are likely not hydrophobic interactions since HA is not very hydrophobic as seen in the contact angle measurements. Rarity of jump-to-contact occurrences indicates van der Waals forces to be minimally important and the lack of consistent trend in adhesion forces and distances with surface charge indicates the interactions is unlikely to have a significant component that is electrostatic in nature. Adhesion interactions most likely have contributions from both long range and short range forces which can be difficult to deconvolute.

2.5 CONCLUSIONS

The average surface charge for phase pure, polycrystalline hydroxyapatite in NaCl solution IS=0.01 and pH~6 was found to be ~ -0.02 C/m^2, equivalent to a surface potential of -64 mV which correlates reasonably well with surface potentials reported in the literature [9,12-20]. The surface charge varies with nanoscale position on the surface and across grain boundaries and seems associated with exposed crystal plane since different facets in the same grain have statistically different surface charges. Excess PO_4^{3-} groups at the surfaces cause all surfaces to have a negative charge and variance is most likely due to different arrangements on each crystal plane of the additional charged ions making up the HA lattice. It is expected that surface charge has a strong influence on the processes of inorganic and organic deposition and structural evolution on the implant material, especially in the initial stages of implantation. New HRFS methodologies can give positionally sensitive measurement of nanoscale surface charge variation, which is an initial step in elucidating electrostatic effects on the bioactivity of HA.

2.6 APPENDIX A - Geometrical Effects of Surface Slope

Since the HA sample probed is topographically heterogeneous, the variance in HRFS curves due to geometrical effects was evaluated. HRFS was approximated as the interaction between a spherical probe tip and a sloped surface (**Fig. 2.A.1**). Variable D is the tip-surface distance measured by the MFP. However, due to the possible slope of the surface there are portions of the probe tip that could be interacting with the surface at distance D', which would change how the tip-surface interaction area varied with distance. The change in tip interaction distance versus D at various possible surface slopes is shown in **Fig. 2.A.1B**. Height profiles via the 3DMFP software were taken across the probe locations as demonstrated in **Fig. 2.8A and 2.9A**, and the slope of the profile corresponding to probe location was calculated. Absolute values of slopes ranged from 0.34° to 22.64°. The plot of averaged (n=3) P-B fitted surface charge versus slope as shown in **Fig. 2.A.2** demonstrates no significant trend. In conclusion, the range of sample surface slope is not large enough to significantly change tip interaction area or force data. This is consistent with geometrical calculations since a sample surface slope of 22.64°, the max slope probed in this experiment, would change the tip interaction area by less than 8% at 15 nm ($5\kappa^{-1}$ at 0.01M), the approximate max range of electrostatic interactions at 0.01 IS. Because the geometrical constraints do not significantly alter the force curves, trends seen in force curves are likely due to electrostatic differences.

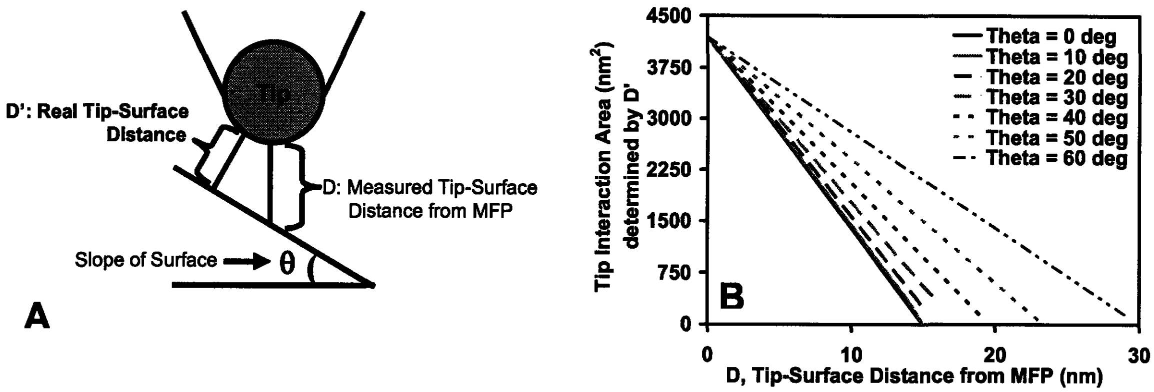

Figure 2.A.1: **A)** Geometrical considerations taken into account when probing a non-flat surface. **B)** Change in interaction area versus distance due to slope of sample surface.

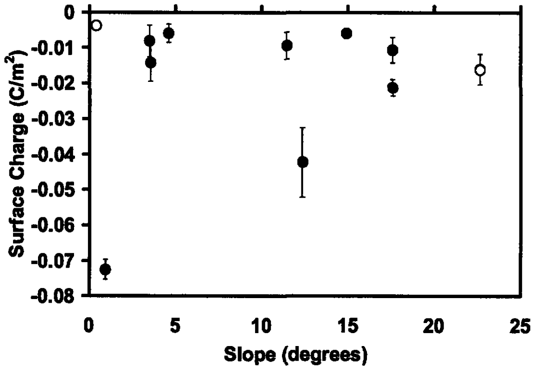

Figure 2.A.2: Averaged (n=3) surface charge calculated from fitting 3DMFP HRFS data (fitting parameters: σ_{COO^-} = -0.0178 C/m^2, IS=0.01M, R_{TIP} =89 nm, pH~6) at each probe position to the P-B theoretical model versus sample surface slope. Hollow data points represent negative slopes. Hi-Lo bars represent one standard deviation.

2.7 REFERENCES

[1] L.L. Hench: *J Am Ceram Soc*; 81(7) (1998), p. 1705.

[2] W. van Raemdonck, P. Ducheyne, P. De Meester. In: Ducheyne P, Hastings G, editors. *Metal and ceramic biomaterials*. Boca Raton, Fl: CRC Press; (1984). p. 143.

[3] W. Suchanek, M. Yoshimura: *J. Mater. Res.*; 13(1) (1998), p. 94.

[4] V.A. Dubok: *Powder Metallurgy and Metal Ceramics*; 39(7-8) (2000), p. 381.

[5] R.Z. LeGeros, J.P. LeGeros. In: Hench LL, Wilson J, editors. *An introduction to bioceramics*. Singapore: World Scientific Publishing; (1993). p. 139.

[6] K. Yamashita, N. Oikawa, T. Umegaki: *Chem Mater*; 8 (1996), p. 2697.

[7] M. Ohgaki, T. Kizuki, M. Katsura, K. Yamashita: *J Biomed Mater Res*; 57 (2001), p. 366.

[8] T. Kobayashi, S. Nakamura, K. Yamashita: *J Biomed Mater Res*; 57 (2001), p. 477.

[9] C.M. Botelho, M.A. Lopes, I.R. Gibson, S.M. Best, J.D. Santos: *J Mater Sci: Mater Med*; 13 (2002), p. 1123.

[10] I.R. Gibson, J. Huang, S.M. Best, W. Bonfield. In: Ohgushi H, Hastings GW, Yoshikawa T, editors. *Bioceramics 12: Proceedings of the international symposium on ceramics in medicine*. River Edge, N.J.: World Scientific Publishing; (1999). p. 191.

[11] N. Patel, S.M. Best, W. Bonfield, I.R. Gibson, K.A. Hing, E. Damien, et al.: *J Mater Sci: Mater Med*; 13 (2002), p. 1199.
[12] P. Ducheyne, C.S. Kim, S.R. Pollack: *J Biomed Mater Res*; 26 (1992), p. 147.
[13] E. Reynolds, A. Wong: *Infection and Immunity*; 39 (1983), p. 1285.
[14] K. Kandori, S. Sawai, Y. Yamamoto, H. Saito, T. Ishikawa: *Colloids and Surf*; 68 (1992), p. 283.
[15] M.K.Y. Rao, R.P. Somasundaran, K.M. Schilling, B. Carson, K.P. Ananthapadmanabhan: *Colloids and Surf A*; 79 (1993), p. 293.
[16] T. Suzuki, T. Yamamoto, M. Toriyama, K. Nishizawa, Y. Yokogwa, M. Mucalo, et al.: *J Biomed Mater Res*; 34 (1997), p. 507.
[17] M.A. Lopes, F.J. Monteiro, J.D. Santos, A.P. Serro, B. Saramago: *J Biomed Mater Res*; 45 (1999), p. 370.
[18] J.C. Knowles, S. Callcut, G. Georgiou: *Biomaterials*; 21 (2000), p. 1387.
[19] P.X. Zhu, Y. Masuda, K. Koumoto: *J Colloid Interface Sci*; 243 (2001), p. 31.
[20] T. Himeno, H.-M. Kim, H. Kaneko, M. Kawashita, T. Kokubo, T. Nakamura. In: Besim Ben-Nissan DS, William Walsh, editor. *Bioceramics 15: Proceedings of the international symposium on ceramics in medicine*. Uetikon-Zuerich, Switzerland: Trans Tech Publications; (2003). p. 457.
[21] S. Chander, D.W. Fuerstenau. In: Misra D, editor. *Adsorption on and surface chemistry of hydroxyapatite*. New York: Plenum Press; (1982).
[22] P.W. Brown, R.I. Martin: *J Phys Chem B*; 103 (1999), p. 1671.
[23] P. Hiemenz, R. Rajagopalan, editors. *Principles of colloid and surface chemistry*. Third ed. New York: Marcel Dekker, Inc.; (1997).
[24] E. Kissa. *Dispersions: Characterization, testing, and measurement*. New York: Marcel Dekker, Inc.; (1999).
[25] In: *Colloidal dynamics*: www.colloidal-dynamics.com; (1999).
[26] A. Noy, D.V. Vezenov, C.M. Lieber: *Annu Rev Mater Sci*; 27 (1997), p. 381.
[27] O. Devereux, P.L. de Bruyn. *Interaction of plane-parallel double layers*. Cambridge, MA: MIT Press; (1963).
[28] A. Sanfeld. *Thermodynamics of charged and polarized layers*. Bath, UK: Wiley-Interscience; (1968).
[29] E.J.W. Verwey, J.T.G. Overbeek, K.V. Nes. *Theory of the stability of lyophobic colloids*. New York: Elsevier Publishing Company; (1948).
[30] *Asylum research*: www.asylumresearch.com.
[31] J. Seog, D. Dean, A.H.K. Plass, S. Wong-Palms, A.J. Grodzinsky, C. Ortiz: *Macromolecules*; 35(14) (2002), p. 5601.
[32] H. Hertz. *Hertz's miscellaneous papers*. London: MacMillian; (1896).
[33] B.V. Derjaguin, V.M. Muller, Y.P.J. Topotov: *Colloid Interface Sci*; 53 (1975), p. 314.
[34] F. Schreiber: *Prog Surf Sci*; 65 (2000), p. 151.
[35] K. Kandori, A. Fudo, T. Ishikawa: *Phys Chem Chem Phys*; 2 (2000), p. 2015.
[36] M. James, R.J. Hunter, R.W. O'Brien: *Langmuir*; 8(2) (1992), p. 420.
[37] G. Toikka, R.A. Hayes, J. Ralston: *Langmuir*; 12 (1996), p. 3783.
[38] H.G. Pedersen, L. Bergstrom: *J Am Ceram Soc*; 82(5) (1999), p. 1137.

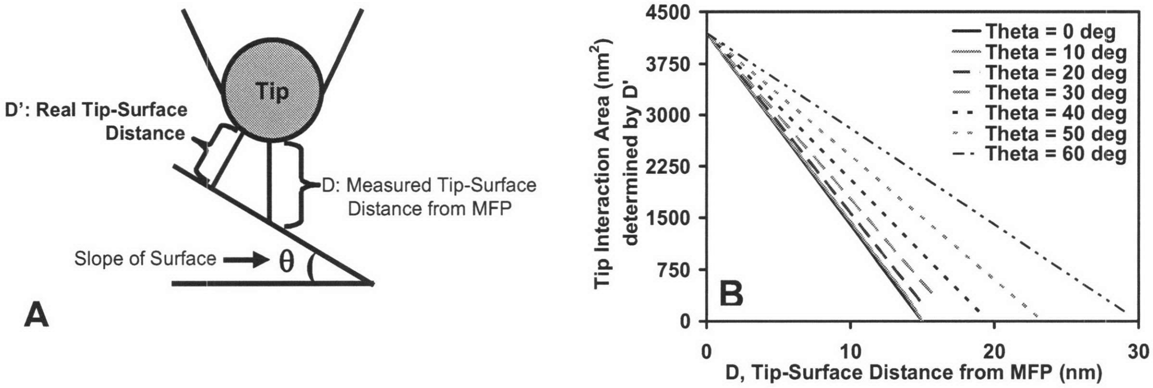

Figure 2.A.1: A) Geometrical considerations taken into account when probing a non-flat surface. **B)** Change in interaction area versus distance due to slope of sample surface.

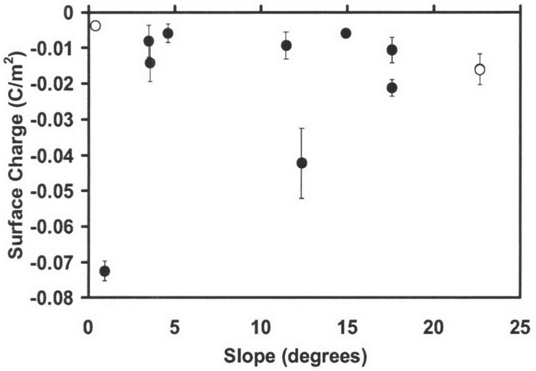

Figure 2.A.2: Averaged (n=3) surface charge calculated from fitting 3DMFP HRFS data (fitting parameters: σ_{COO}- = -0.0178 C/m^2, IS=0.01M, R_{TIP} =89 nm, pH~6) at each probe position to the P-B theoretical model versus sample surface slope. Hollow data points represent negative slopes. Hi-Lo bars represent one standard deviation.

2.7 REFERENCES

[1] L.L. Hench: *J Am Ceram Soc*; 81(7) (1998), p. 1705.

[2] W. van Raemdonck, P. Ducheyne, P. De Meester. In: Ducheyne P, Hastings G, editors. *Metal and ceramic biomaterials*. Boca Raton, Fl: CRC Press; (1984). p. 143.

[3] W. Suchanek, M. Yoshimura: *J. Mater. Res.*; 13(1) (1998), p. 94.

[4] V.A. Dubok: *Powder Metallurgy and Metal Ceramics*; 39(7-8) (2000), p. 381.

[5] R.Z. LeGeros, J.P. LeGeros. In: Hench LL, Wilson J, editors. *An introduction to bioceramics*. Singapore: World Scientific Publishing; (1993). p. 139.

[6] K. Yamashita, N. Oikawa, T. Umegaki: *Chem Mater*; 8 (1996), p. 2697.

[7] M. Ohgaki, T. Kizuki, M. Katsura, K. Yamashita: *J Biomed Mater Res*; 57 (2001), p. 366.

[8] T. Kobayashi, S. Nakamura, K. Yamashita: *J Biomed Mater Res*; 57 (2001), p. 477.

[9] C.M. Botelho, M.A. Lopes, I.R. Gibson, S.M. Best, J.D. Santos: *J Mater Sci: Mater Med*; 13 (2002), p. 1123.

[10] I.R. Gibson, J. Huang, S.M. Best, W. Bonfield. In: Ohgushi H, Hastings GW, Yoshikawa T, editors. *Bioceramics 12: Proceedings of the international symposium on ceramics in medicine*. River Edge, N.J.: World Scientific Publishing; (1999). p. 191.

The formation of CaP layers when HA-based biomaterials are implanted into a bony site [13-16] is considered essential for the creation of a strong bond with the surrounding tissue [17] and it has been demonstrated that CaP layers can be reproduced *in vitro* in an aqueous electrolyte solution which mimics the ionic concentrations and pH of human blood plasma, simulated body fluid (SBF) [17-22]. Literature suggests that negative surface functional groups provide preferential sites for nucleation of calcium phosphate layers [6,23-27]. Negatively charged self-assembled monolayers have been found to produce the highest growth rate of precipitated CaP layers from simulated body fluid [24,25], and electrically polarized, negatively charged ceramic surfaces have been shown to exhibit increased CaP layer formation [26,27], cell adhesion [28], and osteobonding [29], versus non-poled HA samples. Previous experiments on (unsubstituted) dense, polycrystalline HA showed that it was negatively charged, believed to be due to preferential concentration of PO_4^{3-} groups to the top few nanometers of the surface [5,6,30], and that the local nanoscale surface charge per unit area, σ_{HA} (C/m^2), and corresponding zeta potential, ξ_{HA} (mV), were spatially dependent and associated with the exposed crystal plane or facet [12]. The negative surface potentials measured were consistent with the majority of measurements in the literature of HA performed near physiological pH, but varied IS that ranged from -50 mV [6] to 3 mV [31] with the majority between -5 and -20 mV [23,31-38].

Here, the nanomechanical technique of chemically and spatially specific high resolution force spectroscopy [12,39] was applied to dense, polycrystalline 0.8 wt.% SiHA at pH 7.4 and ionic strength (IS)=0.01M. In addition to an electrostatic double layer component, a marked shorter range attractive component, presumed to be van der Waals interactions, was observed and Hamaker constants (*A*) were estimated from the distance of cantilever jump-to-contacts and verified by fits to the inverse square power law [40] to data taken at high IS (1M) where the majority of electrostatic double layer forces are screened out. Using these estimated values of A, the Derjaguin-Landau-Verwey-Overbeek (DLVO) approximation which assumes linear additivity of the electrostatic double layer and van der Waals components [41], and the Poisson-Boltzmann surface charge model for electrostatic double layer forces [42,43], σ_{SiHA} and ξ_{SiHA} were calculated as a function of position for specific nanosized areas within individual grains. These values were compared to σ_{HA} and ξ_{HA} from control experiments on dense, polycrystalline, phase pure HA conducted with the same probe tip to avoid variations due to probe tip geometry.

Such investigations of nanoscale surface properties have great potential to contribute important information relevant to the molecular origins of HA biocompatibility. Furthermore, examining how the incorporation of silicon affects such nanoscale properties as electrostatic repulsion, van der Waals interactions, and morphology of precipitated layers will be critical to the optimization, development, and design of new HA-based biomaterials.

3.2 MATERIALS AND METHODS

3.2.1. Sample Preparation and Characterization

HA and SiHA were synthesized using an aqueous precipitation chemical route between calcium hydroxide, orthophosphoric acid [44], and for SiHA, silicon tetraacetate [2], as described in **Section 1.2.1**. Phase purity of the materials used in this study was verified through X-ray diffraction (XRD) using a *Philips* PW1710 X-ray diffractometer. Data was collected between 25° and 40° 2θ using a step size of 0.02° and a count time of 2.5 seconds. Phase identification was accomplished by comparing the peak positions of the diffraction patterns with ICDD (JCPDS) standards. X-ray fluorescence confirmed the incorporation of 0.8 wt.% Si in the HA lattice and stoichiometry (Ca/P or Ca/(Si+P) ratio ~1.67) using a *Philips* PW1606 spectrometer. FTIR spectra on sintered powders were obtained using a *System* 2000 FT-IR/NIR FT-Raman with a resolution of 4 cm^{-1} and by averaging 100 scans.

Dense (>98% of the theoretical density, 3.16 g/cm^3), polycrystalline HA and SiHA pellets (~1 cm in diameter) were prepared by compacting the as-prepared powders and isostatically pressing them at a pressure of 150 MPa prior to sintering in air at 1200°C for 2 hours, using a ramp rate of 2.5°C per minute. The sintered pellets were visualized using an environmental scanning electron microscopy (ESEM, *Phillips* ESEM-FEG XL30) in low vacuum mode, using an off axis gaseous secondary electron detector and a 10 kV operating voltage. Image analysis was performed using the Leica QWIN image analysis software package. The grain size of the sintered samples was determined by drawing around the boundaries of individual grains manually. The equivalent circular diameter of the grains (G_{gr}) was determined from the measured area of each grain according to the following equation:

$$G_{gr} = \left(\sqrt{\frac{\text{Area}}{\pi}} \right) \times 2 \qquad (3.1)$$

Wettability of the HA and SiHA pellets was assessed via contact angle measurements with deionized (DI) water (Video Contact Angle System 2000, *AST Inc.*) as a function of time allowed to sit on the surface. The temporal evolution of three separate water drops (at different positions) on a HA and SiHA sample were measured, giving n=6 angles (right and left angle of each drop) measured at each time point.

3.2.2. High Resolution Force Spectroscopy

High resolution force spectroscopy experiments were performed using both one and three-dimensional Molecular Force Probes (1DMFP and 3DMFP, respectively, *Asylum Research Inc.*). The three dimensional version has the additional capability to image and perform nanomechanical measurements with nanometer-scale spatial sensitivity. An Au-coated, *Thermomicroscopes*, V-shaped, Si_3N_4 cantilever probe tip (cantilever spring constant, $k \sim 0.05$ N/m as measured by a thermal vibration method [45]) was chemically functionalized with the carboxyl-terminated self-assembling monolayer or COOH-SAM (11-mercaptoundecanoic acid ($HS-(CH_2)_{10}-COOH$, *Aldrich*). The probe tip was prepared and characterized as described in **Section 1.3.2.2**. The same cantilever probe tip was used to image and nanomechanically probe several distinct positions within a variety of grains on both HA and SiHA samples in 0.01M IS trihydroxymethyl aminomethane ($(CH_2OH)_3CNH_2$, Tris buffer) solution (pH=7.4). The probe tip end radius, R_{TIP}, was measured by a *JEOL* 6320FV Field-Emission High-resolution SEM to be ~70 nm. Experiments were also carried out in 1M, pH 7.4 Tris buffer solution with a different probe tip of R_{TIP} ~90 nm. Surface forces, F, were measured as a function of tip-sample separation distance (henceforth referred to as "distance", D) on approach (i.e. probe tip advancing towards the sample surface at a constant rate) and retract (i.e. probe tip moving away from the sample surface at a constant rate) at a z-piezo displacement rate of 2 μm/s. Ten nanomechanical experiments were carried out at each sample site location. For the approach data, F-D curves for each position were averaged, and standard deviations reported. For the retract data, the maximum attractive adhesive force and the corresponding distance of adhesion of each individual retract curve were recorded and averaged for each position. Images presented are contact mode normal cantilever deflection (scan rate of 1 Hz), which is reflective of surface topography; light areas correspond to regions of high topography and darker areas to regions of lower topography. Surface topographical analysis was performed on the corresponding height images within a ~200 × 200 nm square area around each position tested nanomechanically. Tests for statistical significance were carried out on data using unpaired Student's t-tests.

3.2.3. Theoretical Predictions

Derjaguin-Landau-Verwey-Overbeek (DLVO) theory [41] was used predict the surface charge per unit area of HA, σ_{HA}(C/m^2), and SiHA, σ_{SiHA}(C/m^2), as a function of position from the HRFS data on approach as described previously in **Section 1.3.2** [41,46,47]. Average Hamaker constants were estimated for the 0.01M data at each position from the cantilever jump-to-contact separation distances ($D_{jump\text{-}to\text{-}contact}$) using **Eq. 1.3**. The resulting values of *A* calculated from the jump-to-contact method were consistent with fits of high IS (1M) nanomechanical data (where electrostatic double layer forces are largely screened out) to the non-retarded van der Waals force, **Eq. 1.2** [40]. The surface charge per unit area of the probe tip, σ_{COO^-}, was fixed in the simulations and estimated to be ~ -0.018 C/m^2 as determined by control experiments using a COO$^-$-SAM probe tip versus a COO$^-$-SAM planar substrate and fitting the data to the same electrostatic double layer theory described above. R_{TIP}, *A*, and the solution IS were also fixed parameters and σ_{SiHA} or σ_{HA} was the only free fitting variable. Five individual F-D curves per position were fit for $D > 5$ nm to exclude any possible short range non-DLVO components of the interaction. σ was averaged at each position and reported with standard deviations. Once the full nonlinear Poisson-Boltzmann equation was fit to the experimental data, the surface potential was calculated by setting $D=0$ and solving the Poisson-Boltzmann equation. The surface potential calculated in this way is equivalent to zeta potential [48].

3.3 RESULTS

3.3.1. Standard Characterization: FTIR, ESEM, and Contact Angle Measurements

FTIR was used to identify the molecular groups present on SiHA and HA as well as to assess the alteration in the hydroxyl and phosphate bands (**Fig. 3.1**). Peaks were observed for both samples at 568, 600, 960, 1043, and 1008 cm^{-1} corresponding to PO_4^{3-} groups and at 630 cm^{-1} corresponding to the OH^- group. For SiHA, additional peaks were observed at 498 and 884 cm^{-1} corresponding to the SiO_4^{4-} group. It can be observed that Si content leads to a decrease in the intensity of the band at 630 cm^{-1} that corresponds to the OH^- group [6]. This observation is consistent with the substitution mechanism proposed where some phosphate groups (-3) are replaced by silicate groups (-4), leading to the loss of some OH groups in order to maintain the charge balance [2]. The introduction of silicon in the structure of HA also influences the bonds and symmetry modes of the phosphate groups, as can be seen by the intensity ratio between the phosphate bands at 960 (γ1) cm^{-1} corresponding to the symmetric stretch and 1043 (γ3) cm^{-1} that corresponds to the asymmetric stretch. The ratio changes from 0.440 for HA to 0.444 for SiHA. This result is in agreement with previously reported data [2].

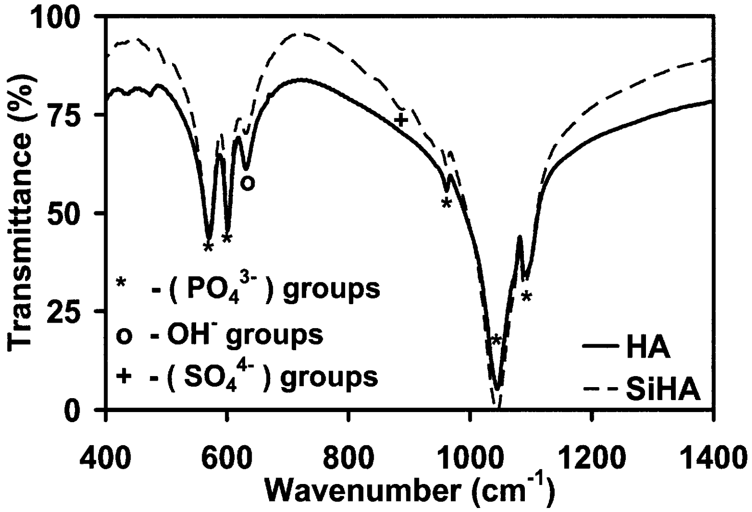

Figure 3.1: FTIR spectra of dense, polycrystalline HA and 0.8 wt.% SiHA.

ESEM images (*data not shown*) show HA to have significantly larger ($p < 0.001$) grains (5.2 ± 2.1 μm, n=100) than SiHA (2.6 ± 1.3 μm, n=100). This observation indicates Si interferes with grain growth, possibly to occur if Si was preferentially located at the grain boundaries and diminished grain boundary movement during grain growth [3].

Contact angle measurements showed SiHA to have an instantaneous contact angle (65 ± 2°, n=6) significantly lower than HA (75 ± 2°, n=6) ($p < 0.001$). As the water droplet remained on the surface, the contact angle for both samples decreased at a rate of 0.11°/second for SiHA and 0.13°/second for HA as shown in **Fig. 3.2**. This decrease is likely due to absorption of water into the crystal lattice, forming a hydrated layer, as has been observed in the literature [49].

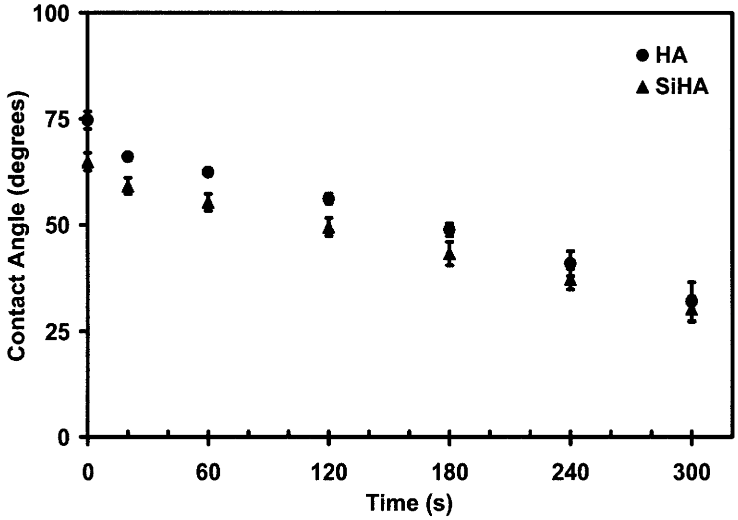

Figure 3.2: Averaged (n=6) contact angle measurements on a SiHA and HA sample surface with time water droplets were allowed to sit on the surface. Hi-lo bars indicate one standard deviation.

3.3.2. Estimations of Hamaker Constants from Approach HRFS Data

A contact mode deflection image of the SiHA and HA surfaces in aqueous electrolyte solution (pH=7.4, IS=0.01M) along with numerical labels for the specific locations where each series of nanomechanical experiments was carried out is shown in **Figs. 3.3A** and **B**, respectively. The probe locations are grouped by crystalline facet where a facet is defined as a distinct topographical face whose area has a relatively constant slope. **Fig. 3.3C** shows typical height profiles of intragranular SiHA and HA surfaces with the baseline slope of underlying grain subtracted. For both the SiHA and HA sample, the average linear root-mean-squared (RMS) roughness of ~200 nm long height profiles (after subtraction of the baseline slope of the grain) through all positions probed was < 1 nm. Therefore, for the areas probed and within experimental resolution, the surfaces of both samples had similar roughness. The length scale of surface features was much smaller than the length scale of the probe tip. For comparison, the radius of the maximum probe tip-surface interaction area at the maximum interaction distance (i.e. D=15 nm [50]) was ~200 nm.

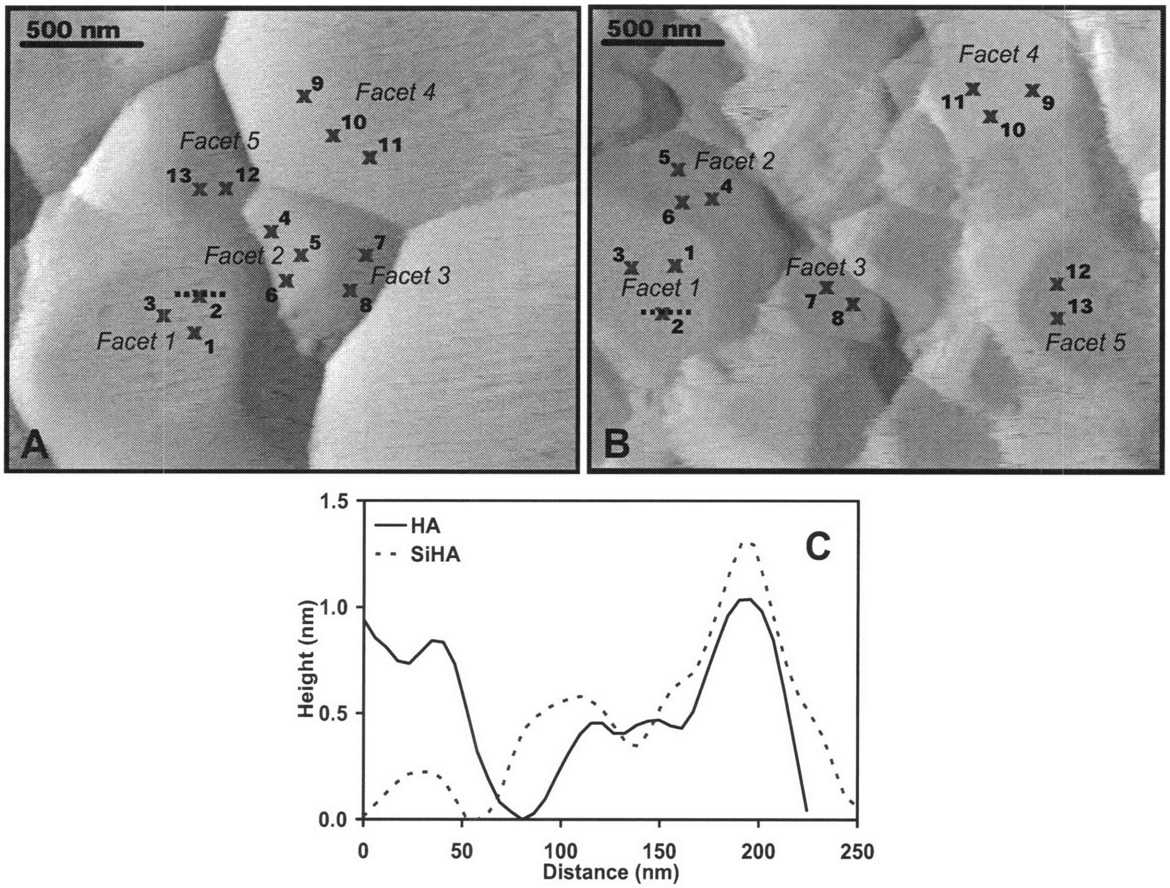

Figure 3.3: Contact mode AFM deflection images taken with a COO^--SAM functionalized probe tip in aqueous solution (R_{TIP} ~70 nm, IS=0.01M, pH=7.4) showing specific positions (X's) probed and labeling of facets on **A)** SiHA and **B)** HA surfaces. **C)** Typical height profiles along black dashed lines in images A and B (corresponding to position 2) with baseline slope of facet subtracted out.

Fig. 3.4A and **B** shows typical individual approach F-D curves in aqueous electrolyte solution (pH=7.4, IS=0.01M) using a COO^--SAM probe tip (R_{TIP} ~70 nm) for SiHA and HA, respectively. Both curves exhibit a nonlinearly increasing net repulsive force (as indicated by the positive value) with decreasing separation distance for $D < 15$ nm and jump-to-contacts. For SiHA position 1 of **Fig. 3.3A**, $D_{jump\text{-}to\text{-}contact} = 2.46$ nm and for HA position 1 of **Fig. 3.3B**, $D_{jump\text{-}to\text{-}contact} = 1.04$ nm. The average $D_{jump\text{-}to\text{-}contact}$ for SiHA (n=76 experiments from all 13 positions) was found to be equal to 2.64 ± 0.82 nm, corresponding to an average Hamaker constant (calculated using **Eq. 1.3**), A_{SiHA}, of 35 ± 27 zJ with a range from 3 - 103 zJ. This value can be compared to that of unsubstituted HA where the average $D_{jump\text{-}to\text{-}contact}$ for HA (n=46 experiments from all 13 positions) for HA was 1.94 ± 0.70 nm, yielding an average A_{HA} of 13 ± 12 zJ with a range from 2 - 32 zJ, which is statistically smaller than that of SiHA ($p<0.01$). Additional nanomechanical experiments were performed in pH 7.4, 1M Tris buffer aqueous solution using a COO^--SAM probe tip (R_{TIP} ~90 nm) **(Fig. 3.5).** Since the majority of $F_{electrostatic}$ is screened out at this high salt concentration, the net force at D>5nm is assumed to be primarily van der Waals. The averaged approach F-D curves (20 experiments each at n=4 positions) were fit to **Eq. 1.2** and yielded an average $A_{SiHA} = 70 \pm 14$ zJ with a range from 60 - 90 zJ, which is somewhat higher than A_{SiHA} calculated from the $D_{jump\text{-}to\text{-}contacts}$ at 0.01M but with overlapping ranges. An average A_{SiHA} was calculated for the 1M data from the jump-to-contact distances and found to be 62 ± 49 (n=22 experiments from all 4 positions) which is statistically similar ($p<0.01$) to the value found through fitting the averaged curves to equation *(3)* and hence, demonstrates self-consistency of the two methods used to estimate A. It was not possible to calculate A_{HA} from the 1M data as only non-DLVO repulsive forces were observed for D<5nm. Hence, all subsequent comparisons to electrostatic double layer theory (at 0.01M IS) were carried out for D>5 nm, where <1% of the force were non-DLVO. **Fig. 3.6A** is plot of the average Hamaker constants versus position and the corresponding frequency histogram for the pooled dataset is shown in **Fig. 3.6B**. Unpaired Student's t-tests comparing the average Hamaker constant for different facets, show that HA possesses significant differences in 7 out of 10 comparisons and for SiHA, 6 out of 10 comparisons are statistically different ($p<0.01$).

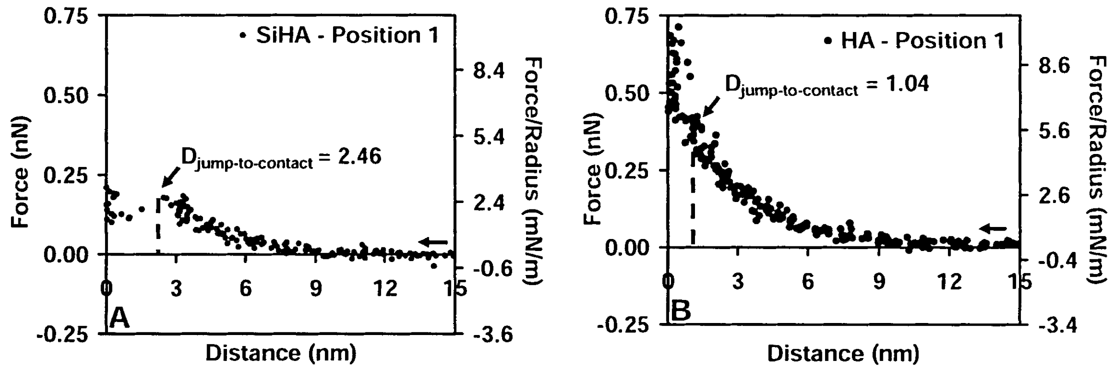

Figure 3.4: Typical individual approach F-D curves taken in aqueous solution (pH=7.4, IS=0.01M, R_{TIP} ~70 nm, k ~0.042 N/m) for a COO^--SAM functionalized probe tip versus **A)** SiHA (position 1 labeled in **Fig. 3.3A**) demonstrating jump-to-contact ($D_{jump\text{-}to\text{-}contact} = 2.46$ nm) and **B)** HA (position 1 labeled in **Fig. 3.3B**) demonstrating jump-to-contact ($D_{jump\text{-}to\text{-}contact} = 1.07$ nm).

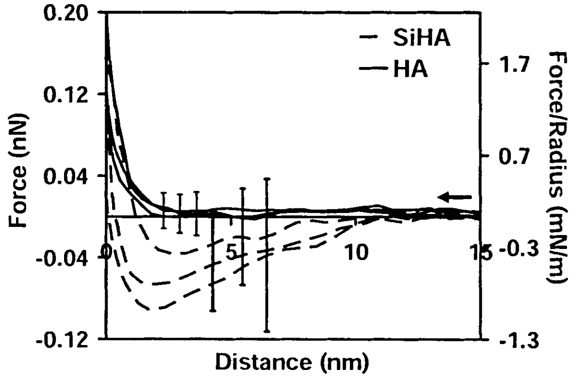

Figure 3.5: Average (n=20) approach F-D curves with standard deviation at three different positions taken in aqueous solution (pH=7.4, IS=1M, R_{TIP} ~90 nm, k ~0.053 N/m) for a COO^--terminated SAM functionalized probe tip vs. HA and SiHA surfaces.

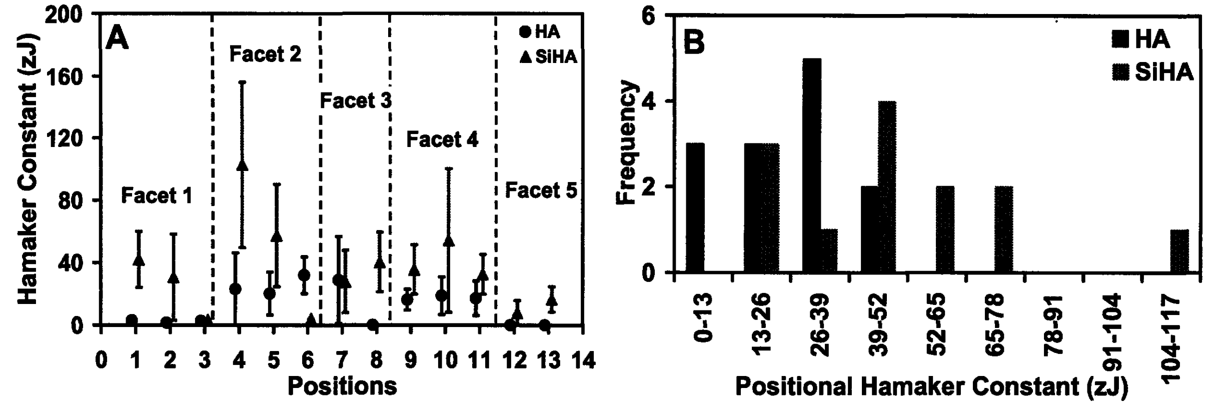

Figure 3.6: **A)** Averaged (n ~ 5-10) Hamaker constant with standard deviation for each position (corresponding to those labeled in **Figs. 3.3A and B**) of SiHA and HA samples calculated from $D_{jump\text{-}to\text{-}contact}$ of individual approach force versus distance **B)** Frequency histogram of Hamaker constant for each position for HA and SiHA.

3.3.3. Averaged HRFS Data on Approach

Fig. 3.7A and **B** show a typical averaged F-D curve with standard deviation for the COO^--SAM probe tip versus SiHA (position 1 of **Fig. 3.3A**) and HA (position 1 of **Fig. 3.3B**) samples, respectively, in aqueous electrolyte solution (pH7.4, 0.01M). The jump-to-contact regions are smoothed out compared to the individual curves (e.g. **Fig. 3.4**) by the averaging process. The standard deviation remains relatively constant and low in the longer range repulsive region (D>5 nm) and is observed to increase with decreasing separation distance at shorter distance ranges (D<5 nm) due to variability in the adhesive jump-to-contacts. **Fig. 3.8** shows the averaged force versus distance curves for the COO^--SAM probe tip versus the SiHA and HA samples at selected sample locations (for data clarity) labeled in **Fig. 3.3**. While the data presented here is all from a single probe tip-sample combination, experiments using different probe tips and samples showed the trends described here to be highly consistent.

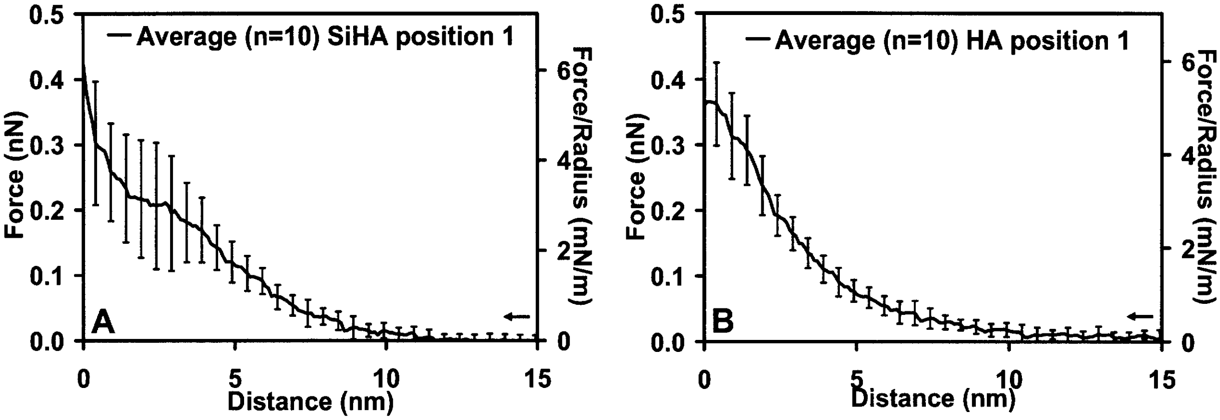

Figure 3.7: Average (n=10) approach F-D curves with standard deviations for one sample position for a COO⁻-SAM functionalized probe tip versus **A)** SiHA (position 1 labeled in **Fig. 3.3A**) and **B)** HA (position 1 labeled in **Fig. 3.3B**) surfaces in aqueous solution (pH=7.4, IS=0.01M, R_{TIP} ~70 nm).

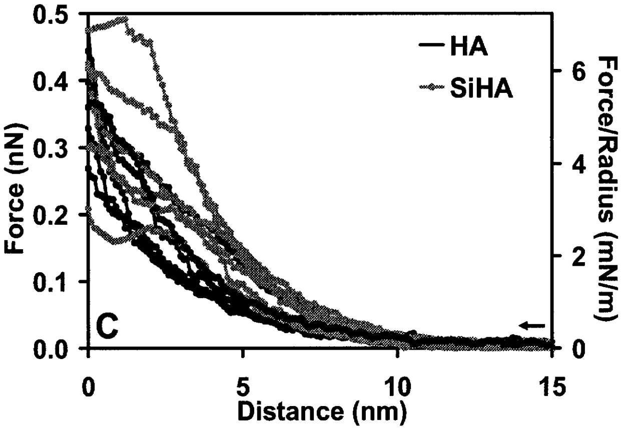

Figure 3.8: Averaged (n=10) approach F-D curves for a COO⁻-SAM functionalized probe tip versus HA and SiHA surfaces in aqueous solution (pH=7.4, IS=0.01M, R_{TIP} ~70 nm) each for a different sample location shown in **Fig. 3.3A and B**.

3.3.4. Estimation of Surface Charge Densities from DLVO Fits

Typical individual approach F-D curves with typical theoretical fits showing the van der Waals and electrostatic components separately as well as the net interaction are given in **Fig. 3.9.** At D=5 nm, the electrostatic component accounted for ~98% of the net force for the HA sample and ~86% of the force for the SiHA sample. The average σ_{SiHA} for all positions calculated from the theoretical fits to approach F-D curves was found to be -0.024 ± 0.013 C/m^2 (n=64 experiments from all 13 positions) while for σ_{HA} it was found to be -0.011 ± 0.006 C/m^2 (n=65 experiments from all 13 positions) where the latter value is consistent with data reported previously on similar samples [12]. Using the non-linear Poisson-Boltzmann equation, surface potentials, equivalent to zeta potentials, were calculated. For SiHA, a potential of -87 ± 55 mV was obtained, while for HA a potential of -49 ± 28 mV was obtained. Unlike standard zeta potential measurements, however, the average σ_{SiHA} and σ_{HA} can be calculated for each nanosized surface position and compared to surface features such as crystalline facet (**Fig. 3.10A**). The effect of sample surface slope on the surface charge density was investigated through geometrical calculations previously and shown to be inconsequential in the ranges measured [12]. Unpaired Student's t-tests comparing the average surface charge density magnitudes on different facets, show that HA possesses significant differences in 7 out of 10 comparisons ($p<0.01$) and for SiHA 4 out of 10 comparisons are statistically different ($p<0.01$). A histogram corresponding to the pooled data in **Fig 3.10A** is given in **Fig. 3.10B** and shows that SiHA has a bimodal distribution with the first peak approximately equivalent to that for HA.

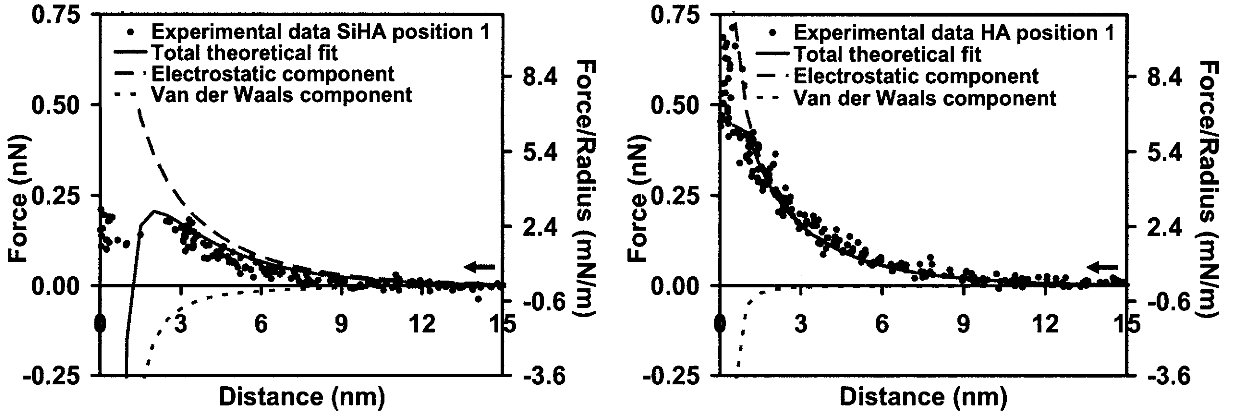

Figure 3.9: Typical individual approach F-D curves with theoretical fits showing predicted net force, as well as individual van der Waals and electrostatic components for a COO$^-$-SAM functionalized probe tip (σ_{COO^-} = -0.0125 C/m^2) versus **A)** SiHA (σ_{SiHA} = -0.018 C/m^2) and **B)** HA (σ_{HA} = -0.009 C/m^2) in aqueous solution (pH=7.4, IS=0.01M, R_{TIP} ~70 nm, k ~0.042 N/m, Hamaker constant fixed to values calculated from $D_{jump\text{-}to\text{-}contact}$: A_{SiHA}= 42 zJ, A_{HA}= 2.8 zJ).

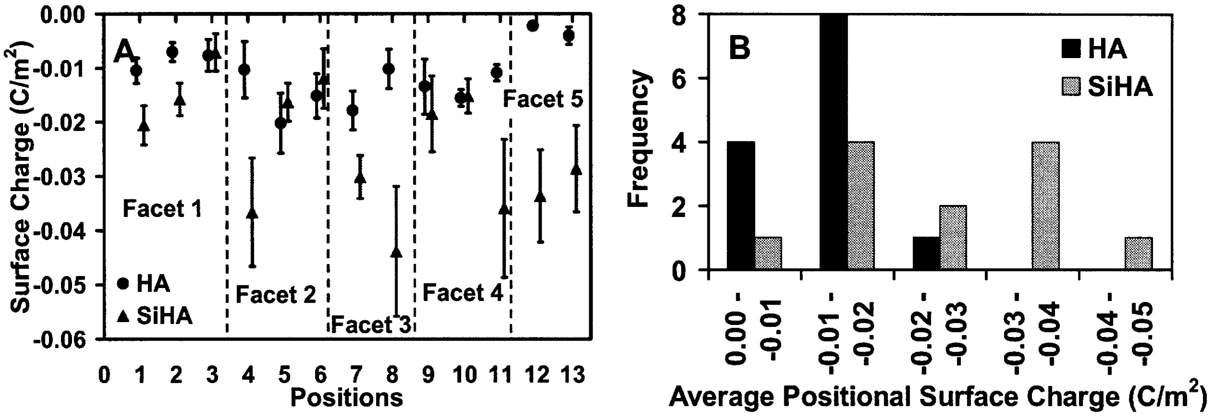

Figure 3.10: **A)** Averaged (n=5) surface charge density for each position (corresponding to those labeled in **Figs. 3.3A and B**) of SiHA and HA samples calculated by fitting individual approach F-D curves for each position to DLVO theory using the following fixed parameters: σ_{COO^-} = -0.0125 C/m^2, IS=0.01M, R_{TIP} ~70 nm, and A_{SiHA} or A_{HA} calculated from the jump-to-contact distances at each location. **B)** Frequency histogram of average surface charge density for each position of HA and SiHA.

3.3.5. Nanoscale Adhesion on Retract

The retract force versus distance curves for the COO^--terminated SAM probe tip vs. HA and SiHA were also analyzed. 100% of the SiHA retract curves showed adhesion while 91% of the HA retract curves showed adhesion. The average adhesion distance for SiHA was 3.6 ± 4.8 nm (number of F-D curves for all 13 positions, n=130) and for HA it was 4.3 ± 5.5 nm (number of F-D curves for all 13 positions, n=126) which are statistically the same ($p<0.01$). The average adhesion force for SiHA was 0.7 ± 0.3 nN (number of F-D curves, n=126 for all 13 positions), which is statistically larger than for HA which was 0.5 ± 0.3 nN (number of F-D curves, n=123 from for 13 positions) ($p<0.01$). The adhesion forces for HA showed more positional dependence (**Fig. 3.11A**), 8 out of 10 facet average comparisons statistically different ($p<0.01$), than SiHA where only 1 out of 10 facet average comparisons were statistically different. **Fig. 3.11B** shows the corresponding frequency histogram for the pooled dataset in **Fig. 3.11A**. For HA, there appears to be a positive correlation ($p<0.01$) between average Hamaker constant and adhesion force for each position (**Fig. 3.12A**, R^2 = 0.75, number of data points, n=13 positions) and a negative correlation between average surface charge density and adhesion force for each position (**Fig. 3.12B**, R^2 = 0.74, number of data points, n=13 positions), while minimal correlation is observed for SiHA.

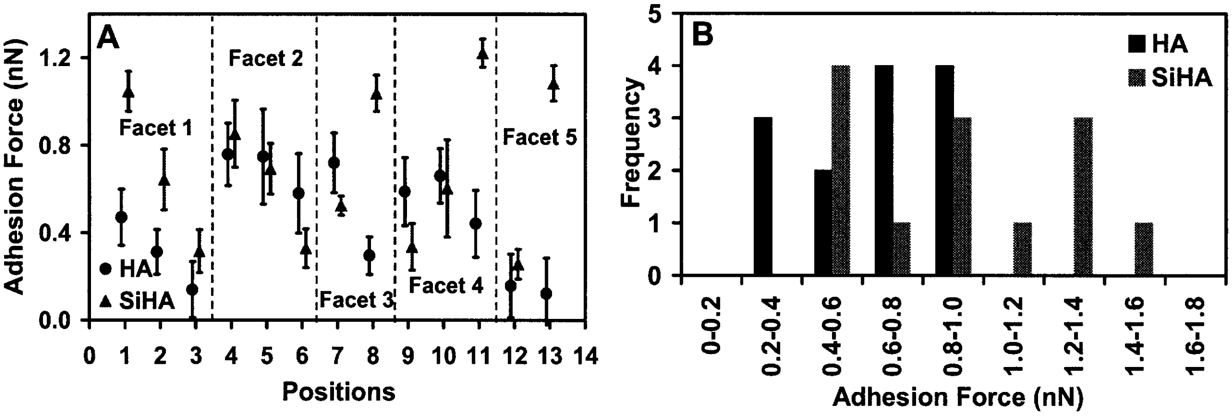

Figure 3.11: **A)** Averaged (n~10) adhesion force for each position (corresponding to those labeled in **Figs. 3.3A and B**) of HA and SiHA samples (IS=0.01M, pH=7.4, k ~0.042 N/m, R_{TIP} ~70 nm). **B)** Frequency histogram of average adhesion force for each position of HA and SiHA.

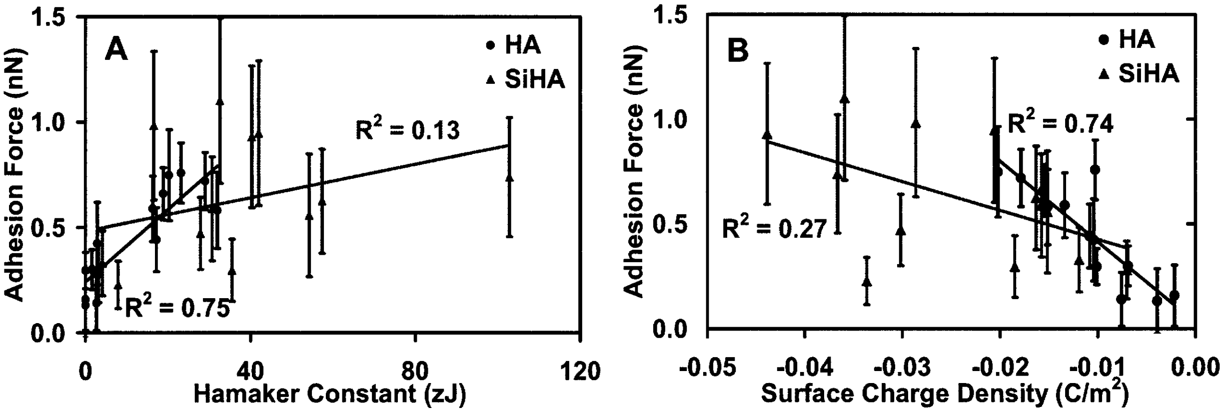

Figure 3.12: **A)** Average (n ~ 10) adhesion force versus average (n ~5-10) Hamaker constant for each position shown in **Figs. 3.3A and B** for SiHA and HA (pH=7.4, IS=0.01M, R_{TIP} ~70 nm, k ~0.042 N/m) showing a correlation factor for HA data of R^2 = 0.75 and for SiHA data R^2 = 0.13. **B)** Average (n ~10) adhesion force versus surface charge for each position shown in **Figs. 3.3A and B** for SiHA and HA (pH=7.4, IS=0.01M, R_{TIP} ~70 nm, k ~0.042 N/m) showing a correlation factor for HA data of R^2 = 0.74 and for SiHA data R^2 = 0.27.

3.4 DISCUSSION

3.4.1 Increased Hamaker Constant of SiHA

One major result of this study was the observation of an increased attractive component of the net force on approach for SiHA compared to HA. This was shown by increased jump-to-contact distances at 0.01M (**Fig. 3.4**) and the marked difference between samples observed at 1M (**Fig. 3.5**) where the HA has a net repulsive intersurface interaction and the Si-HA has a net attractive intersurface interaction. This attraction was attributed to van der Waals forces and the average Hamaker constant of SiHA (35 zJ) was found to be ~2.5× greater that of HA (13 zJ). The magnitudes of the van der Waals values here are intermediate compared to typical ceramics in aqueous solution which range from 1.6 to 94 zJ [51]. Initial contact angle measurements are consistent with SiHA having a higher surface energy than HA, which is related to the Hamaker constant. A contribution to this could come from the fact that Si is more easily polarized than P due to lower atomic number with the same number of electron shells [52]. Another possible contribution is the effect the introduction of Si into the HA structure has on the symmetry modes of the phosphate groups. The intensity ratio between the phosphate bands symmetric stretch (1043 (γ3) cm^{-1}) and asymmetric stretch at 960 (γ1) cm^{-1} changes from 0.440 for HA to 0.444 for SiHA. This indicates the phosphate groups in SiHA have less symmetry, which could increase their polarizability. Both HA and SiHA show spatial variation in the Hamaker constant which could be due to crystal structure and varied number of substituted SiO_4^{4-} groups. Variation in Hamaker constant could play a role in bone-biomaterial bonding.

3.4.2 Increased Surface Charge of SiHA

Consistent with the literature [6], SiHA was observed to be more negatively charged than HA with σ_{SiHA} (-0.024 C/m^2) 2× greater than unsubstituted HA (-0.011 C/m^2). In terms of surface or zeta potential, $\xi_{SiHA} = -87 \pm 55$ mV is 1.8× greater than $\xi_{HA} = -49 \pm 28$ mV. This may be attributed to the substitution of some PO_4^{3-} groups by more negative SiO_4^{4-} groups [6,8]. Although FTIR results in air indicate that the substitution mechanism leads to the loss of OH^- groups in order to maintain charge balance, charge balance is not maintained in fluid. The zeta potential predicted by nanomechanical measurements were, somewhat surprisingly, extremely similar to the measured microelectrophoretic values on similar samples $\xi_{SIHA} = -71 \pm 5$ mV (pH7.4, IS=0.0001M) and $\xi_{HA} = -50 \pm 5$ mV (pH 7.4, IS=0.0001M) [6] given the difference in ionic strength, sample type, dependence on particle size and shape [38,53], and fundamental differences between the two methods. Typically, ξ measured by microelectrophoretic and other techniques are expected to be lower than fitted potentials for nanomechanical data ideal (smooth) surfaces [54] because of the potential drop in the immobilized liquid layer close to the surface since the slip plane where zeta potential is measured is further from the surface than the Stern surface where Poisson-Boltzmann theory begins [55]. The surface charge densities calculated here via nanomechanics experiment are effective charges at the Stern surface since electrostatic double layer theory is valid only within the diffuse double layer [48]. This should resemble what a biomacromolecule or cell feels inside the diffuse double layer approaching a biomaterial surface. During cell adhesion the distance between the cell membrane and biomaterial surface needs to decrease from micrometers to 10-20 nm before adhesion receptors can mediate direct connections [56]. Since the hyaluronan pericellular coat around certain cells (i.e. epithelial and chondrocytes) has a polyelectrolyte character [56], the surface charge properties of the biomaterial are expected to be a critical factor in mediating cell adhesion.

3.4.3 Positional Dependence of Surface Charge and Hamaker Constant

The Hamaker constant and surface charge of SiHA had slightly less surface positional dependence than HA in that there were fewer statistical differences between facet averages (**Fig. 3.6** and **3.10**). The results for HA are consistent with previous research showing the surface charge to vary with nanoscale position on the surface [12]. Variation is associated with exposed crystal plane, each of which has a different arrangement of the charged ions making up the HA lattice, since different facets in the same grain have different surface charges [12]. In this experiment, it was observed that there was less of a correlation between surface charge and crystal plane or facet for SiHA. This observation could be accounted for by substitution of SiO_4^{4-} groups into random PO_4^{3-} lattice locations which could decrease the overall surface charge inconsistently within crystal planes. This result is also consistent with the bimodal distribution in that the more negatively charge peak could be associated with areas of higher SiO_4^{4-} concentration and the peak aligned with HA associated with areas lower in SiO_4^{4-} concentration.

3.4.4 Increased Adhesion Force of SiHA

SiHA was observed to have a larger attractive adhesion force (0.7 ± 0.3 nN) than HA (0.5 ± 0.3 nN). The magnitude of the adhesion forces observed for both HA and SiHA are typical of multiple noncovalent interactions. The adhesion forces measured are likely not hydrophobic interactions since both HA and SiHA become more hydrophilic over time in aqueous solution, as seen in the contact angle measurements. The adhesion forces for HA showed more positional dependence and there appears to be some correlation between increased Hamaker constant and surface charge with increased adhesion force for small A and σ as shown in **Fig.10**. Since both A and σ increase for SiHA, this correlation is only seen in the HA data meaning that the SiHA has larger and more consistent surface adhesion. The larger adhesion forces observed for SiHA are possibly due to its larger Hamaker constant versus HA and are expected to play a role in bone-biomaterial bonding. The greater attractive van der Waals force for SiHA could help overcome the electrostatic double layer repulsion of osteoblasts with negatively charged cell membrane surfaces (e.g. surface potentials of MC3T3-E1 mouse osteoblasts suspended in physiological saline were measured through ultrasonic attenuation spectroscopy to vary from -29.4 to -52.4 mV at pH 7.3 - 7.5 [57]) and the net negative charge of most serum proteins [58]. In general, adhesion interactions have contributions from surface forces such as van der Waals, surface charge, and hydrophobicity as well as surface topology, which can be difficult to deconvolute.

3.4.5 Surface Force Relationship to Bioactivity

As described here, the magnitude and spatial distribution of nanoscale surface characteristics such as surface charge, Hamaker constant, and adhesion are markedly different between SiHA and HA which could account for the increase in bioactivity of SiHA over HA. It is expected these characteristics play an important role in the physiochemical processes that take place upon implantation of a bioactive biomaterial into a bony site. In addition to surface forces measured here it should be reiterated that HA did have larger grains (5.2 ± 2.1 μm) than SiHA (2.6 ± 1.3 μm), likely due to silicon interference in grain growth [3]. The decreased grain size, and therefore increased number of triple grain junctions in SiHA, increases its solubility, which could also affect its bioactivity [59,60]. Bioactivity is likely determined by a combination of nano- and microscale properties. Isolating the effects of each, in theory, could be determined by a general methodology whereby samples are prepared of varying microstructure (e.g. grain size) but constant nanomechanical and structural features, which in practice is nontrivial.

3.5 CONCLUSIONS

The technique of chemically and spatially specific high resolution force spectroscopy has been employed to measure the net nanoscale surface interactions of dense, polycrystalline 0.8 wt.% Si-substituted HA at specific nanosized positions within individual grains in aqueous electrolyte solution. It has been shown that silicon incorporation into an HA lattice results in increased nanoscale attractive van der Waals interactions and an increased negative charge surface charge density relative to unsubstituted HA. Additionally, SiHA was found to have increased surface adhesion less dependant on surface position than HA, possibly due to increased van der Waals interactions. The markedly enhanced *in vitro* apatite formation in simulated body fluid (SBF) [6-8], increased *in vitro* cell proliferation and creation of focal points of adhesion [9], as well as *in vivo* bone ingrowth [10] and remodeling [11] of SiHA over pure HA may be due in part to these nanoscale surface characteristics.

3.6 REFERENCES

[1] E.M. Carlisle: *Science*; 167 (1970), p. 279.

[2] I.R. Gibson, S.M. Best, W. Bonfield: *J Biomed Mater Res*; 44 (1999), p. 422.

[3] I.R. Gibson, S.M. Best, W. Bonfield: *J Am Ceram Soc*; 85 (2002), p. 2771.

[4] R.Z. LeGeros, J.P. LeGeros. In: Hench LL, Wilson J, editors. *An introduction to bioceramics*. Singapore: World Scientific Publishing; (1993). p. 139.

[5] W. van Raemdonck, P. Ducheyne, P. De Meester. In: Ducheyne P, Hastings G, editors. *Metal and ceramic biomaterials*. Boca Raton, Fl: CRC Press; (1984). p. 143.

[6] C.M. Botelho, M.A. Lopes, I.R. Gibson, S.M. Best, J.D. Santos: *J Mater Sci: Mater Med*; 13 (2002), p. 1123.

[7] I.R. Gibson, J. Huang, S.M. Best, W. Bonfield. In: Ohgushi H, Hastings GW, Yoshikawa T, editors. *Bioceramics 12: Proceedings of the international symposium on ceramics in medicine*. River Edge, N.J.: World Scientific Publishing; (1999). p. 191.

[8] F. Balas, J. Perez-Pariente, M. Vallet-Regi: *J Biomed Mater Res*; 66A (2003), p. 364.

[9] C.M. Botelho, R.A. Brooks, S.M. Best, M.A. Lopes, J.D. Santos, N. Rushton, et al. In: Barbosa MA, Monteiro FJ, Correia R, Leon B, editors. *Bioceramics 16: Proceedings of the international symposium on ceramics in medicine*. Uetikon-Zuerich, Switzerland: Trans Tech Publications; (2004). p. 845.

[10] N. Patel, S.M. Best, W. Bonfield, I.R. Gibson, K.A. Hing, E. Damien, et al.: *J Mater Sci: Mater Med*; 13 (2002), p. 1199.

[11] A.E. Porter, N. Patel, J.N. Skepper, S.M. Best, W. Bonfield: *Biomaterials*; 25 (2004), p. 3303.
[12] J. Vandiver, D. Dean, N. Patel, W. Bonfield, C. Ortiz: *Biomaterials*; 26 (2005), p. 271.
[13] P. Ducheyne, Q. Qiu: *Biomaterials*; 20 (1999), p. 2287.
[14] V.A. Dubok: *Powder Metallurgy and Metal Ceramics*; 39(7-8) (2000), p. 381.
[15] J.D. de Bruijn, C.P.A.T. Klein, K. de Groot, V.C.A. van Blitterswijk: *J Biomed Mater Res*; 26 (1992), p. 1365.
[16] M. Neo, T. Nakamura, C. Ohtsuki, T. Kokubo, T. Yamamuro: *J Biomed Mater Res*; 27 (1993), p. 999.
[17] T. Kokubo, H. Kushitani, S. Sakka, T. Kitsugi, T. Yamamuro: *J Biomed Mater Res*; 24 (1990), p. 721.
[18] J. Hamagami, G. Yamaguchi, K. Kanamura, T. Umegaki: *Bioceramics*; 14 (2002), p. 279.
[19] K. Onuma, A. Ito, T. Tateishi, T. Kameyama: *J cryst growth*; 154 (1995), p. 118.
[20] J.H.C. Lin, K.H. Kuo, S.J. Ding, C.P. Ju: *J Mater Sci: Mater Med*; 12 (2001), p. 731.
[21] Y. Leng, J. Chen, S. Qu: *Biomaterials*; 24(2125-2131) (2003), p.
[22] K.A. Khor, H. Li, P. Cheang: *Biomaterials*; 24 (2003), p. 769.
[23] T. Himeno, H.-M. Kim, H. Kaneko, M. Kawashita, T. Kokubo, T. Nakamura. In: Besim Ben-Nissan DS, William Walsh, editor. *Bioceramics 15: Proceedings of the international symposium on ceramics in medicine*. Uetikon-Zuerich, Switzerland: Trans Tech Publications; (2003). p. 457.
[24] K. Sato, Y. Kumagai, J. Tanaka: *J Biomed Mater Res*; 50 (2000), p. 16.
[25] M. Tanahashi, T. Matsuda: *J Biomed Mater Res*; 34 (1997), p. 305.
[26] K. Yamashita, N. Oikawa, T. Umegaki: *Chem Mater*; 8 (1996), p. 2697.
[27] K.S. Hwang, J.E. Song, J.W. Jo, H.S. Yang, Y.J. Park, J.L. Ong, et al.: *J Mater Sci: Mater Med*; 13 (2002), p. 133.
[28] M. Ohgaki, T. Kizuki, M. Katsura, K. Yamashita: *J Biomed Mater Res*; 57 (2001), p. 366.
[29] T. Kobayashi, S. Nakamura, K. Yamashita: *J Biomed Mater Res*; 57 (2001), p. 477.
[30] P.W. Brown, R.I. Martin: *J Phys Chem B*; 103 (1999), p. 1671.
[31] P. Ducheyne, C.S. Kim, S.R. Pollack: *J Biomed Mater Res*; 26 (1992), p. 147.
[32] E. Reynolds, A. Wong: *Infection and Immunity*; 39 (1983), p. 1285.
[33] K. Kandori, S. Sawai, Y. Yamamoto, H. Saito, T. Ishikawa: *Colloids and Surf*; 68 (1992), p. 283.
[34] M.K.Y. Rao, R.P. Somasundaran, K.M. Schilling, B. Carson, K.P. Ananthapadmanabhan: *Colloids and Surf A*; 79 (1993), p. 293.
[35] T. Suzuki, T. Yamamoto, M. Toriyama, K. Nishizawa, Y. Yokogwa, M. Mucalo, et al.: *J Biomed Mater Res*; 34 (1997), p. 507.
[36] M.A. Lopes, F.J. Monteiro, J.D. Santos, A.P. Serro, B. Saramago: *J Biomed Mater Res*; 45 (1999), p. 370.
[37] J.C. Knowles, S. Callcut, G. Georgiou: *Biomaterials*; 21 (2000), p. 1387.
[38] P.X. Zhu, Y. Masuda, K. Koumoto: *J Colloid Interface Sci*; 243 (2001), p. 31.
[39] A. Noy, D.V. Vezenov, C.M. Lieber: *Annu Rev Mater Sci*; 27 (1997), p. 381.
[40] J. Israelachvili. *Intermolecular and surface forces*. second ed. Amsterdam: Academic Press; (1991).
[41] E.J.W. Verwey, J.T.G. Overbeek, K.V. Nes. *Theory of the stability of lyophobic colloids*. New York: Elsevier Publishing Company; (1948).

[42] V.A. Parsegian, D. Gingell: *Biophys. J.*; 12 (1972), p. 1192.
[43] H.J. Butt: *Biophys. J.*; 60 (1991), p. 1438.
[44] M. Akao, H. Aoki, K. Kato: *J Mater Sci*; 16 (1981), p. 809.
[45] J. Seog, D. Dean, A.H.K. Plass, S. Wong-Palms, A.J. Grodzinsky, C. Ortiz: *Macromolecules*; 35(14) (2002), p. 5601.
[46] O. Devereux, P.L. de Bruyn. *Interaction of plane-parallel double layers*. Cambridge, MA: MIT Press; (1963).
[47] A. Sanfeld. *Thermodynamics of charged and polarized layers*. Bath, UK: Wiley-Interscience; (1968).
[48] P. Hiemenz, R. Rajagopalan, editors. *Principles of colloid and surface chemistry*. Third ed. New York: Marcel Dekker, Inc.; (1997).
[49] D. Eichert, C. Combes, C. Drouet, C. Rey. In: Li P, Zhang K, Colwell C, editors. *Bioceramics 17: Proceedings of the international symposium on ceramics in medicine*. Uetikon-Zuerich, Switzerland: Trans Tech Publications; (2005). p. 3.
[50] M. Rixman, D. Dean, C. Macias, C. Ortiz: *Langmuir*; 19(15) (2003), p. 6202.
[51] H.D. Ackler, R.H. French, Y.M. Chiang: *J Colloid Interface Sci*; 179 (1996), p. 460.
[52] P. Atkins. *The elements of physical chemistry*. 2nd ed. New York: W.H. Freeman and Company; (1997).
[53] M. James, R.J. Hunter, R.W. O'Brien: *Langmuir*; 8(2) (1992), p. 420.
[54] G. Toikka, R.A. Hayes, J. Ralston: *Langmuir*; 12 (1996), p. 3783.
[55] H.G. Pedersen, L. Bergstrom: *J Am Ceram Soc*; 82(5) (1999), p. 1137.
[56] M. Cohen, D. Joester, B. Geiger, L. Addadi: *ChemBioChem*; 5 (2004), p. 1393.
[57] I.O. Smith, M.J. Baumann, L.R. McCabe: *J Biomed Mater Res*; 70A (2004), p. 436.
[58] B. Blombaek, L. Hanson, editors. *Plasma proteins*. New York, USA: John Wiley & Sons; (1979).
[59] A.E. Porter, L.W. Hobbs, V.B. Rosen, M. Spector: *Biomaterials*; 23 (2002), p. 725.
[60] A.E. Porter, N. Patel, J.N. Skepper, S.M. Best, W. Bonfield: *Biomaterials*; 24 (2003), p. 4609.

CHAPTER 4: Surface Roughness Accounts for Nanoscale Surface Force Differences between Synthetic Nanostructured Hydroxyapatite and Microstructured Hydroxyapatite

4.1 INTRODUCTION

Nanostructured materials are used in many areas for their increased surface area to volume ratio and their increased surface activity due to increased grain boundary volume [1,2]. Current advances in nanostructured materials for medical applications have progressed in two major areas; the evolution from micro to nano length scales in order to mimic biological materials [3-5] and as biomolecule carriers [3]. It is widely recognized that surface topology on both a micro and nano scale significantly influences cell response [4-9] and generally rougher surfaces have increased cell response [8-10]. It is then a natural progression to attempt to employ specific topologies for medical applications. Specifically, nanostructuring of bone implant materials has been investigated as a way to improve orthopedic implants [4,5,11].

Hydroxyapatite (HA), a bioactive ceramic with a crystal structure very similar to the inorganic phase in bone [12-14], is a popular choice for orthopedic implants. Synthetic HA, however, is typically structured on the micron size scale while biogenic HA crystals in bone take the form of platelets ~ 50 × 25 × 3 nm incorporated within collagen fiber bundles with the c-axis parallel to the collagen fiber axis [15,16]. Nanostructured ceramics, with grain sizes less than 100 nm, such as alumina, titania, and HA have shown increased bioactivity through enhanced apatite formation in simulated body fluid [17], protein adsorption [18], osteoblast adhesion [19] and osteoblast function [4,20,21] over their respective conventionally non-nanostructured ceramics.

In particular, nanostructured hydroxyapatite (nanoHA) shows great promise for use as an orthopedic implant. Many routes have been developed to produce nanoHA. Some common routes include precipitation [22-25], precipitation followed by spraying [26-28] or freeze drying [29], a sol-gel approach [30], a mechanochemical and/or hydrothermal process [31,32], and electrodeposition [33]. Ahn et al. has developed an optimized process to produce nanoHA with excellent chemical and microstructural uniformity via aqueous precipitation followed by pressure-assisted sintering. The resulting material is fully dense, transparent, and nanocrystalline with superior mechanical properties compared to conventional microstructured HA [25]. Nanostructuring of ceramics typically reduces flaw sizes, and this in addition to the high crystallinity, phase purity, and homogeneity of nanoHA are credited with the improved mechanical properties [25]. NanoHA has been found to have enhanced protein adsorption [18] as well as osteoblast attachment, proliferation, and mineralization compared to non-nanostructured HA [4,11,20].

The importance of proteins in mediating cell adhesion is well established [34-37] and it has been shown that in the absence of serum, osteoblast adhesion to nanostructured ceramics was independent of nano grain size, demonstrating the critical role proteins play in the increased osteoblast adhesion to nanostructured ceramics [19]. For anchorage-dependant cells such as osteoblasts, adhesion is critical for subsequent cell function [38] and so greater protein adhesion could also account for the increased osteoblast function on nanostructured ceramics [4,20,21]. Surface topology, as measured by surface radius of curvature on the order of 8-80 nm, has been shown to affect protein adhesion in that different shaped proteins interact with the surface in dissimilar ways [39].

In addition to surface morphology, surface energy or wettability could also influences protein interactions, although surface roughness and wettability are not independent parameters. For smooth surfaces, wettability is directly related to surface energy [40,41], but for rough surfaces the interaction is more complicated. In the Wenzel model, which describes the contact angle for a rough surface, increased surface roughness increases the contact angle for surfaces with contact angle > 90^o and decreases the contact angle for surface with contact angle < 90^o [42]. Increased wettability of a surface has been correlated with increased cell spreading [35,43] and decreased wettability has been correlated with increased protein adhesion and cell adhesion [10,35,44].

Surface morphology is important but it is possible that nanostructuring could result in changes to other surface properties which could also affect protein adhesion and cell response [5,6]. Nanoscale surface interactions, such as surface energy and electrostatics, are also a dominant force in protein and cell adhesion [10,43,45-47] and it is therefore important to be able to measure and understand nanoscale surface interactions of nanoHA (i.e. magnitude, functional form, spatial distribution, and deconvolution into various constituents such as electrostatic double layer and van der Waals).

In order to investigate nanoscale surface interactions in relation to nanostructuring, the nanomechanical technique of chemically and spatially specific high resolution force spectroscopy (HRFS) [48,49] was applied to dense, nanoHA (with grain sizes of 80 ± 30 nm) [11,25]. A nanosized probe tip (R_{TIP}~50nm) functionalized with a carboxy-terminated self-assembling monolayer (COOH-SAM) at the end of a microfabricated cantilever was used to measure the intersurface force (F) perpendicular to the plane of a nanoHA sample as a function of tip-sample separation distance (D) in aqueous electrolyte solution (pH=7.4, ionic strength (IS)=0.01M). Hamaker constants (A) were estimated from the distance of jump-to-contacts and using these estimated values of A, the surface charge density (σ_{nanoHA}) was calculated via comparison to Derjaguin-Landau-Verwey-Overbeek (DLVO) theory [50]. A fully 3 dimensional closed loop system [51] enabled nanoscale spatial specificity. This data was compared to previous experiments on dense, microstructured, polycrystalline, phase pure HA (micronHA) with grain size approximately 1.5 ± 0.7 μm which found $A_{\mathrm{HA}} = 18 \pm 19$ zJ and $\sigma_{\mathrm{HA}} = -0.011 \pm 0.006$ C/m^2 [52].

Investigations of nanoscale surface properties of nanoHA compared to micronHA could determine the changes, if any, in nanoscale surface interactions such as Hamaker constant, surface charge, and adhesion forces due to nanostructuring. If there are differences in surface interactions than these differences could influence the increased bioactivity of nanoHA over micronHA in addition to surface morphology differences.

4.2 MATERIALS AND METHODS

4.2.1 Sample Preparation and Characterization

Dense monolithic samples of nanoHA were donated by *Angstrom Medica* (Woburn, MA). Briefly, it was prepared through an aqueous precipitation reaction between analytical grade $Ca(NO_3)_2{\cdot}4H_2O$ and $(NH_4)_2HPO_4$. The precipitate was washed, ground, dried, and aged with processing parameters such as solution pH, aging time and temperature adjusted to achieve desired ultrafine spherical particles which were then subjected to pressure-assisted sintering at 90°C for 30 minutes at a pressure of 100 MPa. The resulting material is transparent and 98.5% of theoretical density of HA [11,25]. Phase purity was verified through X-ray diffraction (XRD) using a Rigaku Rotaflex X-ray diffractometer with Cu X-ray source. Data was collected between 25° and 40° 2θ using a step size of 0.02°. Phase identification was accomplished by comparing the peak positions of the diffraction patterns with ICDD (JCPDS) standards.

Samples ~ 6 mm × 4 mm × 2 mm, were cut using a *Isomet* 1000 diamond saw under irrigation of de-ionized (DI) water. The top surface was then polished on a uni-pol polisher (*Geoscience Instruments Corp.*), first using a *Bueler* ultra-prep 45 μm grit diamond grinding disk, then *Metadi* diamond suspensions 15 μm, 6 μm and 1 μm, followed by a final step using *MasterMet* 0.2 μm diameter colloidal silica. The sample was then sonicated in DI water, etched for 90 seconds in 2% citric acid to expose grain structure, sonicated once more in DI water and dried in N_2 gas.

Tapping mode AFM (TMAFM) with Olympus AC240TS-2 rectangular Si cantilevers (spring constant, $k_C = 2$ N/m) was employed to image surface topography, grain size, and surface roughness at high resolutions in ambient conditions with a *Veeco* (*Digital Instruments)* Nanoscope IIIA System Controller and Multimode AFM. Wettability was assessed via contact angle measurements with DI water (Video Contact Angle System 2000, *AST Inc*). A *Kratos* AXIS Ultra Imaging X-ray Photoelectron Spectrometer (XPS) with AlKα X-ray source was used to analyze surface compositions at a take-off angle of 0° (penetration depth < 10 nm).

4.2.2 Chemically and Spatially Specific High Resolution Force Spectroscopy

High resolution force spectroscopy (HRFS) experiments were performed using a three-dimensional Molecular Force Probe (*Asylum Research, Inc)* which has the capability to image and perform nanomechanical measurements with nanometer-scale spatial sensitivity. Images presented are contact mode normal cantilever deflection (scan rate of 1 Hz) and surface topographical analysis was performed on the corresponding height images within a ~ 200 × 200 nm square area around each position tested nanomechanically. An Au-coated, *Thermomicroscopes*, V-shaped, Si_3N_4 cantilever probe tip (cantilever spring constant, k ~ 0.04 N/m as measured by a thermal vibration method [53]) was chemically functionalized with a carboxyl-terminated self-assembling monolayer (COOH-SAM, 11-mercaptoundecanoic acid ($HS-(CH_2)_{10}-COOH$, *Aldrich*). The probe tip was prepared and characterized as described in **Section 1.3.2.2**. This functionalized probe tip with R_{TIP} ~50 nm was used to image and nanomechanically probe several distinct positions on a nanoHA sample in 0.01M ionic strength (IS) trihydroxymethyl aminomethane (Tris buffer, $(CH_2OH)_3CNH_2$) solution (pH=7.4). Surface forces, F, normal to the sample plane were measured as a function of tip-sample separation distance (henceforth referred to as "distance", D) on approach (i.e. probe tip advancing towards the sample surface at a constant rate) and retract (i.e. probe tip moving away from the sample surface at a constant rate) at a z-piezo displacement rate of 2 μm/s. Ten nanomechanical experiments were carried out at each sample site location. For the approach data, F-D curves for each position were averaged, and standard deviations reported. For the retract data, the maximum attractive adhesive force and the corresponding distance of adhesion of each individual retract curve were recorded and averaged for each position.

Derjaguin-Landau-Verwey-Overbeek (DLVO) theory [50] was used predict the surface charge per unit area of nanoHA, $\sigma_{nanoHA}(C/m^2)$, as a function of position from approach HRFS data as described in **Section 1.3.2** [50,54,55]. Average Hamaker constants (*A*) were estimated at each position from the cantilever jump-to-contact separation distances ($D_{jump\text{-}to\text{-}contact}$) using **Eq. 1.3**. The surface charge per unit area of the probe tip, σ_{COO^-}, was fixed in the simulations and estimated to be ~ -0.0108 C/m^2 as determined by control experiments using a COO^--SAM probe tip versus a COO^--SAM planar substrate and fitting the data to the same electrostatic double layer theory described above. Fixed parameters were solution ionic strength (IS=0.01M), probe tip surface charge density, R_{TIP}, and *A*. Throughout this work, "n" refers to the number of measurements taken.

4.3 RESULTS

4.3.1 Surface Characterization

Typical 3 and 1 μm scan TMAFM amplitude and height images of the nanoHA surface with height profiles are given in **Fig. 4.1**. Analysis of these images yielded an average grain diameter of 83 ± 27 nm (n = 89). The average root-mean-squared (RMS) roughness of five 1 μm scans was calculated from TMAFM height images and found to be 16 ± 11 nm. Contact angle measurements with DI water gave an averaged (n=12) contact angle of 69° ± 3.6° which is statistically smaller ($p<0.05$) than that measured previously for micronHA (75 ± 2°, n=6) [52]. An XPS survey spectrum showed the expected Ca, P, and O peaks. The Ca/P ratio was calculated to be 1.45, less than the stoichiometric 1.67.

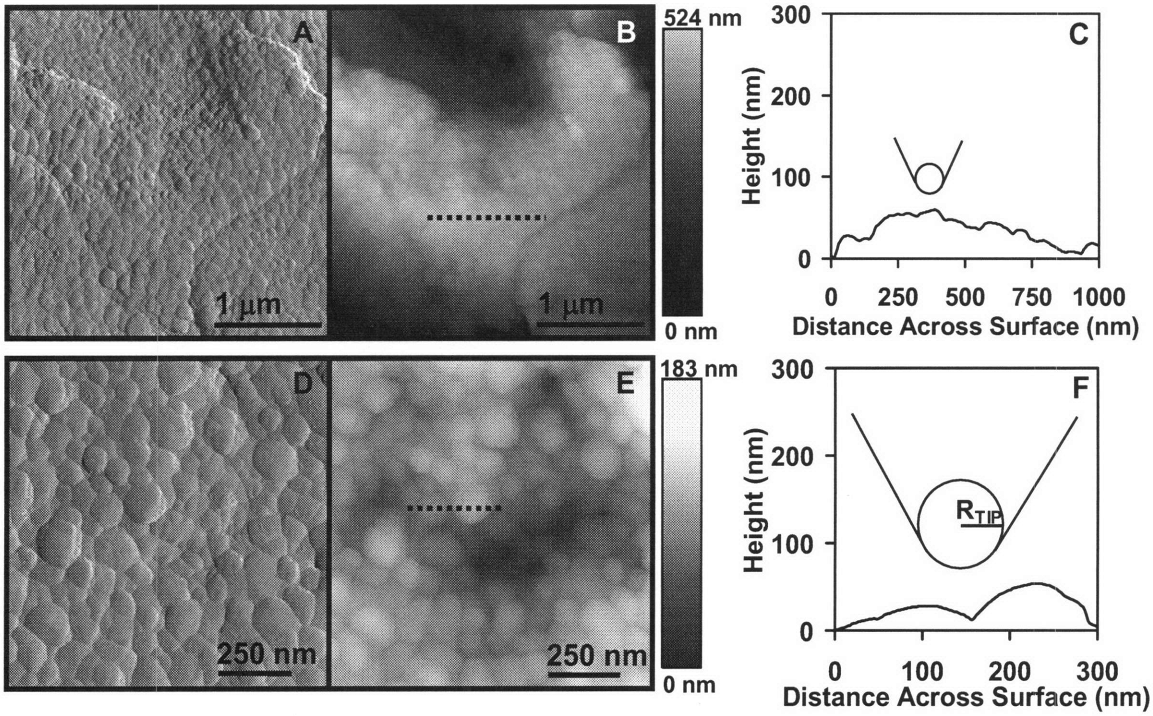

Figure 4.1: TMAFM images of nanoHA in ambient conditions **A)** 3 μm scan amplitude image **B)** 3 μm scan height image **C)** height profile of dotted line in B with tip schematic **D)** 1 μm scan amplitude image **E)** 1 μm scan height image **F)** height profile of dotted line in E with tip schematic showing R_{TIP}.

4.3.2 Chemically and Spatially Specific High Resolution Force Spectroscopy (HRFS)

Nanomechanical experiments were carried out at 7 specific locations. Approximately 200 nm long profiles were obtained through each position and the linear root-mean-squared (RMS) roughness was calculated for each profile. The average linear RMS roughness of profiles was 5.9 ± 2.9nm. **Fig. 4.2** shows averaged (n=10) approach F-D curves with standard deviation for all probe positions. All curves exhibit nonlinearly increasing net repulsive force with decreasing separation distance for $D < 15$ nm.

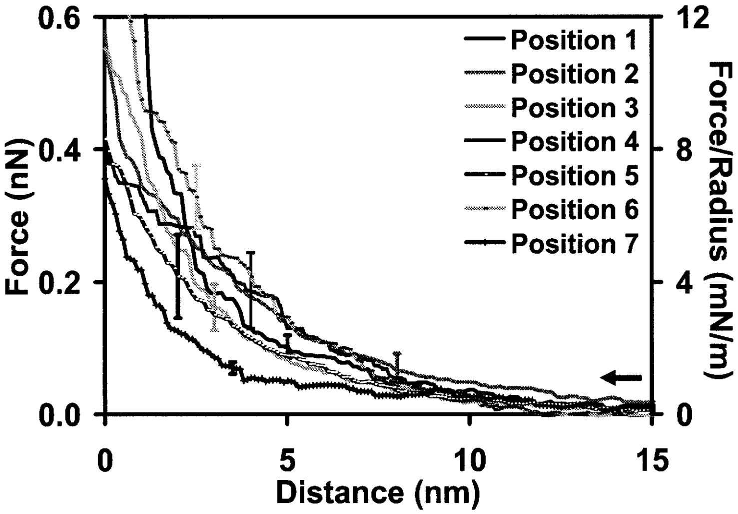

Figure 4.2: Averaged (n = 5) approach F-D curves for COO$^-$-terminated SAM probe tip versus nanoHA at all 7 probe locations (R_{TIP}~50 nm, IS=0.01M, pH=7.4).

The average Hamaker constant was calculated from the average of individual curve $D_{jump-to-contacts}$ at each position using **Eq. 1.3** and found to be equal to 7.5 ± 8.9 zJ (n=7). This value is less than that of micronHA measured previously, 12.6 ± 11.8 zJ [52]. Once estimates for *A* were found for each position, 5 individual curves at each probe position were fit to DLVO theory to determine σ_{nanoHA} for each position. A typical individual approach F-D curves with theoretical fits showing the van der Waals and electrostatic components separately as well as the net interaction is shown in **Fig. 4.3.** The average σ_{nanoHA} calculated for each position from theoretical fits to 5 individual approach curves are shown in **Fig. 4.4A**. The average σ_{nanoHA} for all positions was found to be -0.012 ± 0.007 C/m^2 (n=7), statistically similar (p=0.05) to σ_{micronHA} from previous work which was found to be -0.011 ± 0.005 C/m^2 (n=13) [52]. A surface charge frequency histogram for nanoHA and micronHA is given in **Fig. 4.4B**.

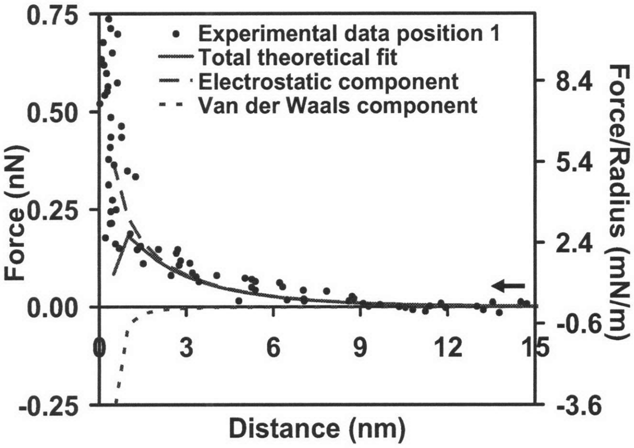

Figure 4.3: Typical individual approach F-D curves with theoretical fit showing predicted net force, as well as individual van der Waals and electrostatic components for a COO$^-$-SAM functionalized probe tip ($\sigma_{\text{COO-}}$ = -0.0108 C/m^2) versus nanoHA (σ_{nanoHA} = -0.018 C/m^2) in aqueous solution (pH=7.4, IS=0.01M, R_{TIP} ~50 nm, k ~ 0.04 N/m, Hamaker constant fixed to values calculated from $D_{\text{jump-to-contact}}$: A_{nanoHA}= 3.5 zJ).

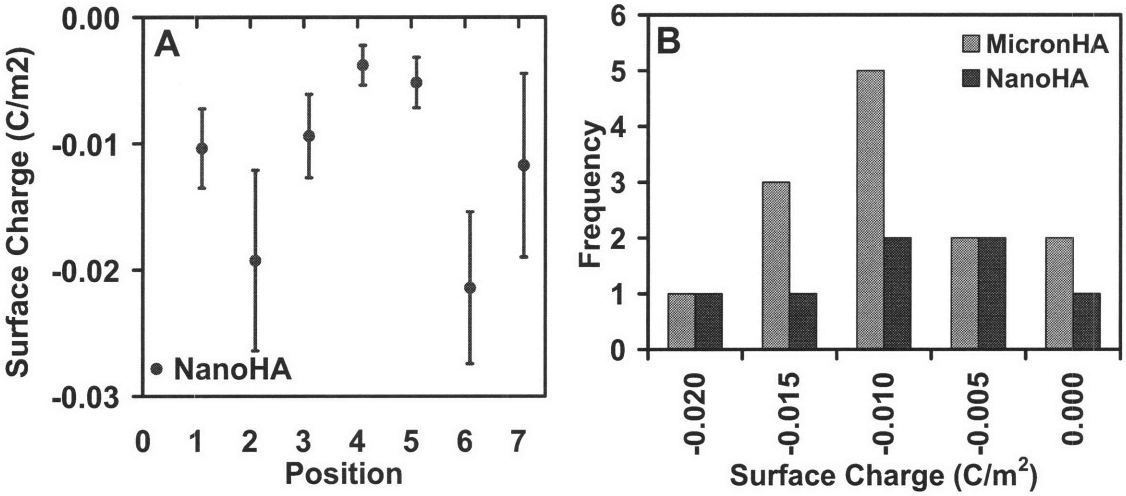

Figure 4.4: **A)** Averaged (n=5) surface charge density for each position (corresponding to those labeled in **Figs. 4.2A**) calculated by fitting individual approach F-D curves for each position to DLVO theory using the following fixed parameters: $\sigma_{\text{COO-}}$ = -0.0108 C/m^2, IS=0.01M, R_{TIP} ~50 nm, and A_{nanoHA} calculated from $D_{\text{jump-to-contact}}$ at each location **B)** Average surface charge frequency histogram for nanoHA and micronHA.

Retract curves were also analyzed and 82% of the retract curves showed adhesion. Average adhesion distance was 9.4 ± 3.9 nm (number of F-D curves, n=70 for all 7 positions). Average positional adhesion forces are shown in **Fig. 4.5A** and the overall average adhesion force was 0.17 ± 0.16 nN (number of F-D curves, n=70 for all 7 positions). The adhesion distance was significantly larger ($p<0.05$) and the adhesion force was significantly smaller ($p<0.05$) than that found previously for micronHA which were respectively 2.8 ± 0.9 nm and 0.46 ± 0.29 nN [52]. **Fig. 4.5B** shows the corresponding frequency histogram for average adhesion force.

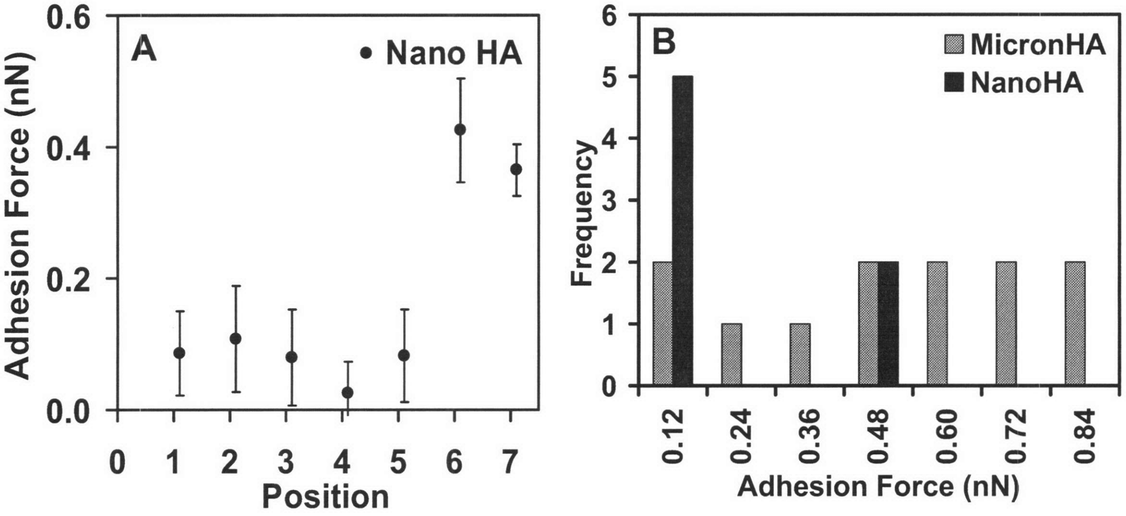

Figure 4.5: **A)** Averaged (n ~10) adhesion force for each nanoHA probe position (IS=0.01M, pH=7.4, k ~0.04 N/m, R_{TIP} ~50 nm). **B)** Frequency histogram of average adhesion force.

4.4 DISCUSSION

The morphological differences between micronHA and nanoHA are clear and distinct in that nanoHA has much smaller grain sizes and increased nanoscale roughness. Preparation of nanoHA was optimized for spherical equiaxed grains which are observed in **Fig. 4.1** with an average grain diameter of ~80 nm. The average radius of curvature, ~40 nm, and the average linear RMS roughness, ~6 nm, are on the order of the size of proteins. Some examples include the abundant plasma proteins albumin (~14 × 4 nm [56]), fibrinogen (~46 × 4 nm [57]), and laminin (~70 × 70 nm [58]) as well as the important adhesion proteins fibronectin (~16 nm × 9 nm [59]) and vitronectin, which is a linear protein ~15 nm in length [60]. Surface topology, as measured by surface radius of curvature on the order of 8-80 nm, has been shown to significantly affect protein adhesion and in particular, proteins of different shapes interact with the surface in dissimilar ways [39]. Therefore, increased protein absorption and selective protein absorption of nanoHA over non-nanostructured HA is likely due to surface morphology, (i.e. grain shape and size).

NanoHA was found to have increased wettability over micronHA but surface roughness and wettability are not independent. For smooth surfaces, wettability is directly related to surface energy [40,41] but rough surfaces are described by the Wenzel model which claims that surface roughness increases the contact angle for surfaces with contact angle $> 90^{\circ}$ and decreases the contact angle for surface with contact angle $< 90^{\circ}$ [42,61]. Common materials such as titanium, calcite, quartz, barite, and talc of all been shown to have increased wettability with increased roughness [62,63] and decreased contact angle with decreased grain size has been observed for nanostructured ceramics in the literature [18]. However, increased protein adhesion was also observed for nanostructured ceramics with decreasing grain size [18], contrary to typical results that show increased protein adhesion with decreased wettability [10,35,44]. Since decreased contact angle and increased protein adhesion have been observed for nanoHA [18], this indicates surface roughness is likely the cause for decreased contact angle.

NanoHA was found to have a decreased Ca/P ratio (1.45) compared to previously measured micronHA (1.63). It is believed a couple nanometer thick Ca deficient surface layer (Ca/P ratio ~1.5) is created during solid-solution equilibrium during the precipitation process

[64]. Since precipitates approximately turn into grains during sintering, grain boundaries would be Ca deficient. The increase in grain boundary volume for nanoHA would account for its decreased Ca/P ratio as measured by XPS although its bulk Ca/P ratio is likely closer to stoichiometric.

Of the three nanoscale surface interactions examined via HRFS; Hamaker constant, surface charge, and surface adhesion, nanoHA was found to have decreased Hamaker constant, similar surface charge, and decreased surface adhesion compared to micronHA. However, both Hamaker constant and adhesion force which were dissimilar have been shown to be influenced by surface roughness. DLVO measurements via AFM have shown surface roughness to attenuate short range forces such as van der Waals but to have less effect on longer range electrostatic forces [65,66]. It is generally thought that the effect of surface roughness is to limit closer contact between the probe tip and the surface, decreasing contact area, and thus decreasing van der Waals attractions and adhesion force [65,67]. Much lower values of adhesion than expected have been measured for surface/particle interactions which have been attributed to surface roughness [67]. Since the grains of nanoHA have similar size and curvature to the probe tip, as visualized in **Fig. 4.1C and F**, it is likely the decreased grain size and increased roughness of nanoHA over micronHA leads to decreased probe tip-surface interactions which would account for the decreased Hamaker constant and adhesion forces observed.

4.5 CONCLUSIONS

Of the four surface interactions examined nanoHA was found to have increased wettability, decreased Hamaker constant, similar surface charge and decreased surface adhesion compared to micronHA. However, increased surface roughness could account for all differences seen. In conclusion, the surface interaction differences noted here between nanoHA and micronHA are due to probe tip-surface geometric interactions caused by surface roughness and therefore surface force magnitudes of nanoHA and micronHA at physiological conditions for biomolecules should be similar. The enhanced protein adsorption [18] as well as osteoblast attachment, proliferation, and mineralization [4,11,20] of nanoHA over non-nanostructured HA are likely due more to surface morphology differences than nanoscale surface force differences.

4.6 REFERENCES

[1] Z. Zhang, C.-C. Wang, R. Zakaria, J. Ying: *J Phys Chem B*; 102 (1998), p. 10871.
[2] A.J. Zarur, J. Ying: *Nature*; 403 (2000), p. 65.
[3] R.J. Narayan, P.N. Kumta, C. Sfeir, D.-H. Lee, D. Olton, D. Choi: *J Mater*; 56 (2004), p. 38.
[4] J. Tan, W.M. Saltzman: *Biomaterials*; 25 (2004), p. 3593.
[5] E. Palin, H. Liu, T.J. Webster: *Nanotechnology*; 16 (2005), p. 1828.
[6] A. Curtis, C. Wilkinson: *Biomaterials*; 18 (1997), p. 1573.
[7] C.D.W. Wilkinson, M. Riehle, M. Wood, J. Gallagher, A.S.G. Curtis: *Mat Sci Eng C*; 19 (2002), p. 263.
[8] D. Deligianni, N. Katsala, P.G. Koutsoukos, Y. Missirlis: *Biomaterials*; 22 (2001), p. 87.
[9] D.M. Brunette, D. Chehroudi: *J Biomech Eng*; 121 (1999), p. 49.
[10] M. Lampin, R. Warocquier-Clerout, C. Legris, M. Degrange, M.F. Sigot-Luizard: *J Biomed Mater Res*; 36 (1997), p. 99.
[11] E.S. Ahn. Nanostructure apatites as orthopedic biomaterials [PhD Thesis]. Cambridge, MA: Massachusetts Institute of Technology; 2001.
[12] L.L. Hench: *J Am Ceram Soc*; 81(7) (1998), p. 1705.
[13] R.Z. LeGeros, J.P. LeGeros. In: Hench LL, Wilson J, editors. *An introduction to bioceramics*. Singapore: World Scientific Publishing; (1993). p. 139.
[14] W. van Raemdonck, P. Ducheyne, P. De Meester. In: Ducheyne P, Hastings G, editors. *Metal and ceramic biomaterials*. Boca Raton, Fl: CRC Press; (1984). p. 143.
[15] J. Rho, L. Kuhn-Spearing, P. Zioupos: *Med Eng Phys*; 20(2) (1998), p. 92.
[16] R.S. Lakes: *Nature*; 361 (1993), p. 511.
[17] X. Liu, X. Zhao, R.K.Y. Fu, J.P.Y. Ho, C. Ding, P.K. Chu: *Biomaterials*; 26 (2005), p. 6143.
[18] T.J. Webster, C. Ergun, R.H. Doremus, R.W. Siegel, R. Bizios: *J Biomed Mater Res*; 51 (2000), p. 475.
[19] T.J. Webster, R.W. Siegel, R. Bizios: *Biomaterials*; 20 (1999), p. 1221.
[20] T.J. Webster, C. Ergun, R.H. Dormeus, R. Siegal, R. Bizios: *Biomaterials*; 21 (2000), p. 1803.
[21] R.L. Price, K.M. Haberstroh, T.J. Webster: *Med Biol Eng Comput*; 41 (2003), p. 372.
[22] P.N. Kumta, C. Sfeir, D.-H. Lee, D. Olton, D. Choi: *Acta Biomat*; 1 (2005), p. 65.

[23] S. Zhang, K.E. Gonsalves: *J Mater Sci: Mater Med*; 8 (1997), p. 25.
[24] S. Sarig, F. Kahana: *J cryst growth*; 237-239 (2002), p. 55.
[25] E.S. Ahn, N.J. Gleason, A. Nakahira, J. Ying: *Nano Lett*; 1(3) (2000), p. 149.
[26] R.S. Lima, K.A. Khor, H. Li, P. Cheang, B.R. Marple: *Mat Sci Eng A*; 396 (2005), p. 181.
[27] P. Luo, T.G. Nieh: *Biomaterials*; 17 (1996), p. 1959.
[28] L.C. Chow, L. Sun: *J Res Natl Inst Stand Technol*; 109 (2004), p. 543.
[29] M.J. Phillips, J.A. Darr, Z.B. Luklinska, I. Rehman: *J Mater Sci: Mater Med*; 14 (2003), p. 875.
[30] C.S. Chai, B. Ben-Nissan: *J Mater Sci: Mater Med*; 10 (1999), p. 465.
[31] C.-W. Chen, C.S. Oakes, K. Byrappa, R.E. Riman, K. Brown, K.S. TenHuisen, et al.: *J mater chem*; 14 (2004), p. 2425.
[32] X. Guo, P. Xiao: *J Am Ceram Soc*; 88 (2005), p. 1026.
[33] M. Shirkhanzadeh: *J Mater Sci: Mater Med*; 9 (1998), p. 65.
[34] C.E. Orsello, D. Lauffenburger, D. Hammer: *TRENDS in Biotechnology*; 19(8) (2001), p. 310.
[35] B.D. Ratner, A.S. Hoffman, F.J. Schoen, J.E. Lemons, editors. *Biomaterials science: An introduction to materials in medicine*. San Diego: Academic Press; (1996).
[36] C.R. Howlett, M.D.M. Evans, W.R. Walsh, G. Johnson, J.G. Steele: *Biomaterials*; 15 (1994), p. 213.
[37] M. Cohen, D. Joester, B. Geiger, L. Addadi: *ChemBioChem*; 5 (2004), p. 1393.
[38] A.J. Freemont: *Int J Exp Pathol*; 74 (1993), p. 411.
[39] P. Roach, D. Farrar, C. Perry: *J Am Chem Soc*; 128 (2005), p. 3939.
[40] P. Hiemenz, R. Rajagopalan, editors. *Principles of colloid and surface chemistry*. Third ed. New York: Marcel Dekker, Inc.; (1997).
[41] B.D. Ratner, A.B. Johnston, T.J. Lenk: *J Biomed Mater Res*; 21(A1) (1987), p. 59.
[42] R.N. Wenzel: *J Phys Colloid Chem*; 53 (1949), p. 1466.
[43] S.A. Redey, M. Nardin, D. Bernache-Assolant, C. Rey, P. Delannoy: *J Biomed Mater Res*; 50 (2000), p. 353.
[44] A. Sethuraman, M. Han, R.S. Kane, G. Belfort: *Langmuir*; 20 (2004), p. 7779.
[45] D. Leckband: *Annu Rev Biophys Biomol Struct*; 29 (2000), p. 1.
[46] M. Ohgaki, T. Kizuki, M. Katsura, K. Yamashita: *J Biomed Mater Res*; 57 (2001), p. 366.
[47] T. Kobayashi, S. Nakamura, K. Yamashita: *J Biomed Mater Res*; 57 (2001), p. 477.
[48] A. Noy, D.V. Vezenov, C.M. Lieber: *Annu Rev Mater Sci*; 27 (1997), p. 381.
[49] J. Vandiver, D. Dean, N. Patel, W. Bonfield, C. Ortiz: *Biomaterials*; 26 (2005), p. 271.
[50] E.J.W. Verwey, J.T.G. Overbeek, K.V. Nes. *Theory of the stability of lyophobic colloids*. New York: Elsevier Publishing Company; (1948).
[51] *Asylum research*: www.asylumresearch.com.
[52] J. Vandiver, D. Dean, N. Patel, C. Botelho, S. Best, J.D. Santos, et al.: *in press (J Biomed Mater Res) DOI #30737*; (2006), p.
[53] J. Seog, D. Dean, A.H.K. Plass, S. Wong-Palms, A.J. Grodzinsky, C. Ortiz: *Macromolecules*; 35(14) (2002), p. 5601.
[54] O. Devereux, P.L. de Bruyn. *Interaction of plane-parallel double layers*. Cambridge, MA: MIT Press; (1963).

[55] A. Sanfeld. *Thermodynamics of charged and polarized layers*. Bath, UK: Wiley-Interscience; (1968).

[56] T. Peters: *Adv Prot Chem*; 37 (1985), p. 161.

[57] R.G. Reed, R.C. Feldhoff, O.L. Clute, T. Peters: *Biochemistry*; 14 (1975), p. 4578.

[58] S. Ayad, R. Boot-Handford, M.J. Humpries, K.E. Kadler, A. Shuttleworth. *The extracellular matrix facts book*. San Diego, CA: Academic Press Inc.; (1994).

[59] V.E. Koteliansky, M.A. Glukhova, M.V. Bejanian, V.N. Smirnov, V.F. Filimonov, O.M. Zalite, et al.: *Eur. J. Biochem*; 119 (1981), p. 619.

[60] K.T. Preissner, D. Jenne: *Thrombosis and Haemostasis*; 66(1) (1991), p. 123.

[61] A. Nakajima, K. Hashimoto, T. Watanabe: *Monatshefte fur Chemi*; 132 (2001), p. 31.

[62] F. Rupp, L. Scheideler, D. Rehbein, D. Axmann, J. Geis-Gerstorfer: *Biomaterials*; 25 (2004), p. 1429.

[63] U. Ulusoy, M. Yekeler: *Chem Eng Proc*; 44 (2005), p. 557.

[64] P.W. Brown, R.I. Martin: *J Phys Chem B*; 103 (1999), p. 1671.

[65] R.F. Considine, C.J. Drummond: *Langmuir*; 17 (2001), p. 7777.

[66] S. Bhattacharjee, C.-H. Ko, M. Elimelech: *Langmuir*; 14 (1998), p. 3365.

[67] H.-J. Butt, B. Cappella, M. Kappl: *Surf Sci Rep*; (2005), p.

CHAPTER 5: Nanoscale Surface Properties of Calcium Phosphate Precipitated onto Synthetic Hydroxyapatite, Chemically Modified Hydroxyapatite, and Silicon Substituted Hydroxyapatite from Simulated Body Fluid

5.1 INTRODUCTION

The formation of calcium phosphate (CaP) layers, composed of small crystallites on the surface of a biomaterial, is considered essential for bone bonding [1-3]. The ability of a material to initiate formation of CaP layers, which support formation of an interfacial bond between the implant and the surrounding tissue, has been unique to bioactive ceramics [2,4,5] although recently there has been investigation into surface treatments that can induce bioactivity on other biomaterials [2,6-8]. It is believed that a CaP layer is formed *in vivo* on bioactive ceramic surfaces through precipitation of calcium and phosphate ions released from the partially dissolving ceramic, as well as ions present in biological fluid [3], at early implantation periods and that this layer subsequently mediates formation of an interfacial bond [2] possibly through alignment of collagen fibers [3,9]. There is ample evidence for the formation of precipitated CaP crystals and/or layers onto implanted sintered hydroxyapatite within 2-6 weeks [3,9-12]. Transmission electron microscope (TEM) cross-sectional images of dense sintered HA pellets, rods, and granules implanted *in vivo* show surface CaP layers on the order of 10s to 100s of nm thick over the course of 2 weeks to 6 months implantation time [3,11,13]. Globular and plate-like crystallites from 15 nm [14] up to 300 nm [15] in diameter have been observed as well as needle-like crystallites 3-7 × 30-40 × 60-100 nm in size [16]. The structure of CaP precipitates *in vivo* has been found to vary from amorphous [12,13], to calcium-deficient carbonate-containing crystalline HA [11], to crystalline octacalcium phosphate (OCP) [17]. Although CaP layers are known to be integral to bone bonding, the fine nanoscale morphology and intersurface interactions of precipitated CaP layers controlling implant adhesion to the surrounding bone are largely unknown and can be studied using *in vitro* techniques as described following.

As interstitial blood plasma is the predominant fluid that initially interacts with implanted biomaterials, the interaction of bioactive materials with simulated body fluid (SBF), an aqueous electrolyte solution that mimics the ionic concentrations and pH of human blood plasma, is of interest [2]. Plasma contains large amounts of sodium and chloride ions, intermediate amounts of bicarbonate ions, relatively small amounts of potassium, calcium, magnesium, and phosphate ions [18], as well as various proteins. Plasma is highly saturated with respect to calcium phosphates and therefore has great potential to precipitate calcium phosphate [2,19]. It has been demonstrated that CaP layers can be precipitated *in vitro* on bioactive ceramics such as HA, bioglass, and certain glass ceramics from acellular protein-free SBF [1,17,20-23] and the formation of these layers *in vitro* is considered one method of assessing a material's bioactivity [1,10,17]. Studies of *in vitro* CaP precipitation from SBF onto single crystals [21], granules [24,25], porous samples [17], disks [26-29], and plasma-sprayed coatings [23,30,31] of HA have all been performed using such techniques as TEM, X-ray photospectroscopy (XPS), atomic force microscopy (AFM), Fourier transform infrared spectroscopy (FTIR), and thin-film X-ray diffraction (XRD). The thickness of CaP precipitated layers ranges from <1 μm [28,30,32] up to 40 μm [22,23]. The structure of the CaP precipitated layer ranges from poorly crystalline, calcium-deficient HA [24,25,32] with Ca/P ratios from ~1.2-1.5, to almost stoichiometric HA [24,30,31], to OCP [24]. Both *in vitro* and *in vivo* precipitated CaP layers are varied in terms of structure, crystallinity, Ca/P ratio and thickness. The formation of CaP layers on bioactive materials is believed to be mainly a material dependant inorganic chemical process, partly because CaP layers form from SBF devoid of biomolecules or cells [2,11]. Despite this conclusion, *in vitro* and *in vivo* experiments have found significant differences in CaP precipitation rates in that *in vitro* experiments typical take ~30 days to form a surface CaP layer on dense synthetic HA [22,27], whereas *in vivo* experiments have found CaP layer formation in less than 2 weeks [3,11], which indicates there is some affect from the biological environment.

The precipitation of CaP layers onto HA has been suggested to be controlled by electrostatic interactions [33-36], and the literature suggests a negative surface charge is advantageous for the formation of CaP layers through adsorption of positive calcium ions resulting in a positive layer that attracts negative phosphate groups leading to the formation of a CaP layer [34]. It is expected that surface charge density is an influential parameter on precipitation and the structural evolution on the biological-biomaterial interface, especially in the initial stages of implantation. This hypothesis is supported by reports of increased rates of *in vitro* CaP precipitation onto negatively charge self-assembling monolayers [34] and increased crystal growth of bone-like HA to negatively charged surfaces of electrically polarized HA [37]. Additionally, silicon-substituted HA (SiHA), which contains small amounts of silicon substituted into its lattice, has been shown to have markedly enhanced *in vitro* CaP layer formation from SBF compared to non-substituted HA [27,38,39], possibly due to its increased negative surface charge due to substitution of PO_4^{3-} groups with the more negatively charged SiO_4^{4-} groups [38,40].

The first objective of this study was to determine whether or not surface charge is a determinant of CaP precipitation on HA using an *in vitro* model. To accomplish this, dense, polycrystalline, phase pure synthetic HA was chemically treated to yield an amine functionalized surface, while maintaining equivalent micro and nanoscale topography, which was positively charged when immersed in SBF. AFM imaging was employed to directly visualize the formation and morphology of CaP layers at high spatial resolutions as a function of SBF incubation time and this data was compared to controls on untreated HA, which is negatively charged [41]. The second objective of this study was to quantify the nanoscale surface interactions of precipitated CaP layers onto dense, polycrystalline, phase pure synthetic HA and dense, polycrystalline 0.8 weight (wt.)% SiHA, using chemically and spatially specific high resolution force spectroscopy (HRFS), in particular as a function of different morphological regions. Comparison of HRFS data with appropriate theory [42-44] enabled the extraction of relevant material parameters such surface charge density, σ, and van der Waals Hamaker constant, A.

5.2 MATERIALS AND METHODS

5.2.1 Sample Preparation: HA, SiHA, (NH_2)-Functionalized HA, and CaP Layers

HA and SiHA pellets (diameter ~8.5 mm) were synthesized using an aqueous precipitation chemical route between calcium hydroxide, orthophosphoric acid [45], and for SiHA, silicon tetraacetate [46], as described in **Section 1.2.1** . The surface phosphate groups of HA were conjugated to primary amine-containing molecules using the carbodiimide cross-linker EDC (1-ethyl-3-[3-imethylaminopropyl] carbodiimide hydrochloride, *Pierce,* Product No. 22980) and imidazole (*Sigma-Aldrich*), as shown in **Fig 5.1**. An HA pellet was placed in 50 mL of 0.15 ionic strength (IS) phosphate-buffered saline (PBS) with 10 mM of ethylenediaminetetraacetic acid (EDTA, *Sigma-Aldrich*) to which 1.5 g of EDC was added. Immediately, 5 mL of 0.25 M ethylenediamine (*Pierce*, Product No. 23031) in 0.1 M imidazole was added and the solution was gently shaken until all reagents dissolved. Then an additional 20 mL of 0.1 M imidazole was added and the solution was incubated at 37°C overnight. After incubation the HA pellet was rinsed with PBS and stored in PBS until use. The pKA of surface bound amine groups is ~7 [47].

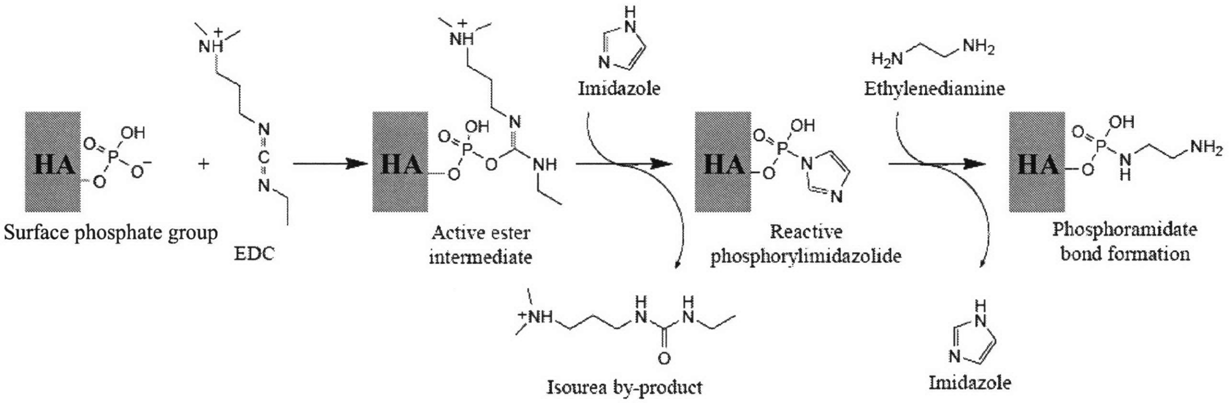

Figure 5.1: Amine-modification of HA via surface phosphate groups using EDC, imidazole, and ethylenediamine [48].

SBF was prepared by dissolving reagent grade NaCl, $NaHCO_3$, KCl, $Na_2HPO_4 \cdot 2H_2O$, $MgCl_2 \cdot 6H_2O$, $CaCl_2$, Na_2SO_4 in Millipore water and buffering at pH 7.4 and 37°C with trihydroxymethyl aminomethane (Tris buffer, $(CH_2OH)_3CNH_2$) and small amounts of HCl [1,49]. All reagents were obtained from *Sigma-Aldrich*. The ion concentrations for this solution are given in **Table 5.1.** Samples were incubated in SBF, refreshed every 2 days, at 37°C for 36 (HA and SiHA) and 7 (NH_3^+-HA) days. As an additional control, HA was also incubated in Tris buffer for 7 days.

	Na^+	K^+	Mg^{2+}	Ca^{2+}	Cl^-	HCO_3^-	HPO_4^{2-}	SO_4^{2-}	
Blood Plasma	142	5	1.5	2.5	103	27	1	0.5	mM
SBF	142	5	1.5	2.5	125	27	1	0.5	mM

Table 5.1: Ion concentrations of simulated body fluid compared to human blood plasma [1,49].

5.2.2. Sample Characterization

The HA and SiHA pellets were found to be >98% of the theoretical density (3.16 g/cm^3) as measured by water displacement and phase purity was verified by wide angle X-ray diffraction and X-ray fluorescence spectroscopy as reported previously [40]. Topography and surface roughness of dry and wet samples were assessed via tapping and contact mode respectively using a *Veeco* (*Digital Instruments)* Nanoscope IIIA System Controller and Multimode AFM. The initial dry HA and SiHA surfaces were examined via tapping mode (TMAFM) in ambient conditions at a scan rate of 1 htz using *Olympus* AC240TS-2 rectangular Si cantilevers (probe tip end radius, R_{TIP} <10 nm, cantilever spring constant, k_c ~2 N/m). The average intragranular linear root-mean-squared (RMS) roughness was calculated from AFM height images using five ~200 nm long line profiles obtained on different crystalline facets (surface regions of relatively constant slope) after the baseline slope was subtracted out. To monitor temporal evolution of CaP precipitation from SBF onto HA and NH_3^+-HA and to monitor the control HA sample incubated in Tris buffer over the first 7 days, fluid-cell contact mode AFM imaging (CMAFM) at a scan rate of 1 htz was employed at various time points in the particular incubation solution (SBF or Tris) using *Thermomicroscopes* Si_3N_4 V-shaped cantilever with k_c ~0.01 N/m. SiHA and HA samples were removed from the incubation solution and dried after 36 days and the resulting well-formed CaP layers were imaged via TMAFM in ambient conditions as described above. A *Kratos* AXIS Ultra Imaging X-ray Photoelectron Spectrometer (XPS) with AlKα X-ray source was used to analyze surface compositions at a take-off angle of 0° (penetration depth < 10 nm).

5.2.3 Chemically and Spatially Specific High Resolution Force Spectroscopy

HRFS experiments were performed with electroplated Au-coated [50] Si_3N_4 cantilever probe tips chemically functionalized with alkanethiol self-assembled monolayers terminated with carboxyl groups (COO^--SAM, 11-Mercaptoundecanoic acid, HS-$(CH_2)_{10}$-COOH, *Aldrich* - used as received). Probe tips were prepared and characterized as described in **Section 1.3.2.2**. HRFS was conducted on the NH_3^+-HA sample before and after modification using a one-dimensional Molecular Force Probe (1DMFP, *Asylum Research, Inc)* to measure the force, F (nN), normal to the sample plane versus tip-sample separation distance normal to the sample surface, D (nm), on approach (i.e. cantilever probe tip advancing towards the surface). HRFS was also conducted on the CaP precipitated layers on HA and SiHA after a 36 day incubation in SBF using a three-dimensional Molecular Force Probe (3DMFP, *Asylum Research, Inc)* to measure F-D curves on both approach and retract (i.e. cantilever probe tip moving away from sample surface). The 3DMFP has the capability to simultaneously image the surface via AFM and perform positionally sensitive HRFS in the plane of the sample surface. Using this capability, distinct areas of CaP precipitate morphology were probed. All experiments were carried out in 0.01 M Tris buffer solution (pH=7.4) where the carboxyl groups on the functionalized probe tip were negatively charged [47]. At each location 10-20 HRFS experiments were performed, at a constant z-piezo rate of 2 μm/s and then averaged with standard deviations reported. This data was compared to previous similar experiments on the initial HA and SiHA surfaces [40,41]. The symbol "n" is used throughout to indicate the number of experiments carried out.

Comparison of HRFS to Derjaguin-Landau-Verwey-Overbeek (DLVO) theory [42] was used to predict the surface charge per unit area (σ, C/m^2) for HA, SiHA, NH_3^+-HA, as well as at specific locations on the CaP layers precipitated on HA and SiHA as described previously in

Section 1.3.2 [42-44]. Average van der Waals component for each position was calculated from the Hamaker constant (*A*) which was estimated from jump-to-contact separation distances ($D_{jump-to-contact}$) using **Eq. 1.3**. A single probe tip was used to probe the HA surface before modification and the NH_3^+-HA surface after modification. Three similar but separate probe tips were used to probe the CaP layers precipitated on HA and a single separate probe tip was used to probe CaP layers precipitated on SiHA. All probe tips were of the same type, from the same manufacturer, and all results compared between probe tips are corrected for tip radius. R_{TIP} for all cantilevers varied between ~ 40-80 nm and the probe tips' experimentally determined surface charge, σ_{COO^-}, varied between -0.0870 - -0.0187 C/m^2. These probe tips of known R_{TIP} and σ were used to probe the samples, and experimental data was fit to theoretical solutions with R_{TIP}, *A*, and the solution IS as fixed parameters and σ as the only free fitting variable.

5.3 RESULTS

5.3.1 Temporal Evolution of NH_3^+-HA and HA surfaces in SBF or Tris buffer

CMAFM images in fluid (SBF or Tris) of the NH_3^+-HA sample incubated in SBF compared to two controls (HA incubated in SBF or Tris) for 1, 3 and 7 days are given in **Fig. 5.2** and allow identification of a precipitated CaP layer by direct visualization. Linear RMS surface roughness was additional used on corresponding height images to monitor the temporal evolution of CaP precipitation (**Fig. 5.3**). No CaP was observed to precipitate on the NH_3^+-HA incubated in SBF or the control HA incubated in Tris buffer after 7 days (**Fig. 5.2C** and **I**) which was further quantified as shown by the linear RMS surface roughness which maintained a constant value of ~1 nm (**Fig 5.3**). The HA incubated in SBF showed clear CaP precipitation (**Fig. 5.2F**) and correspondingly, a statistically significant ($p<0.05$) increase in surface roughness from 1.1 ± 0.4 nm to 2.5 ± 0.5 nm after 7 days of incubation.

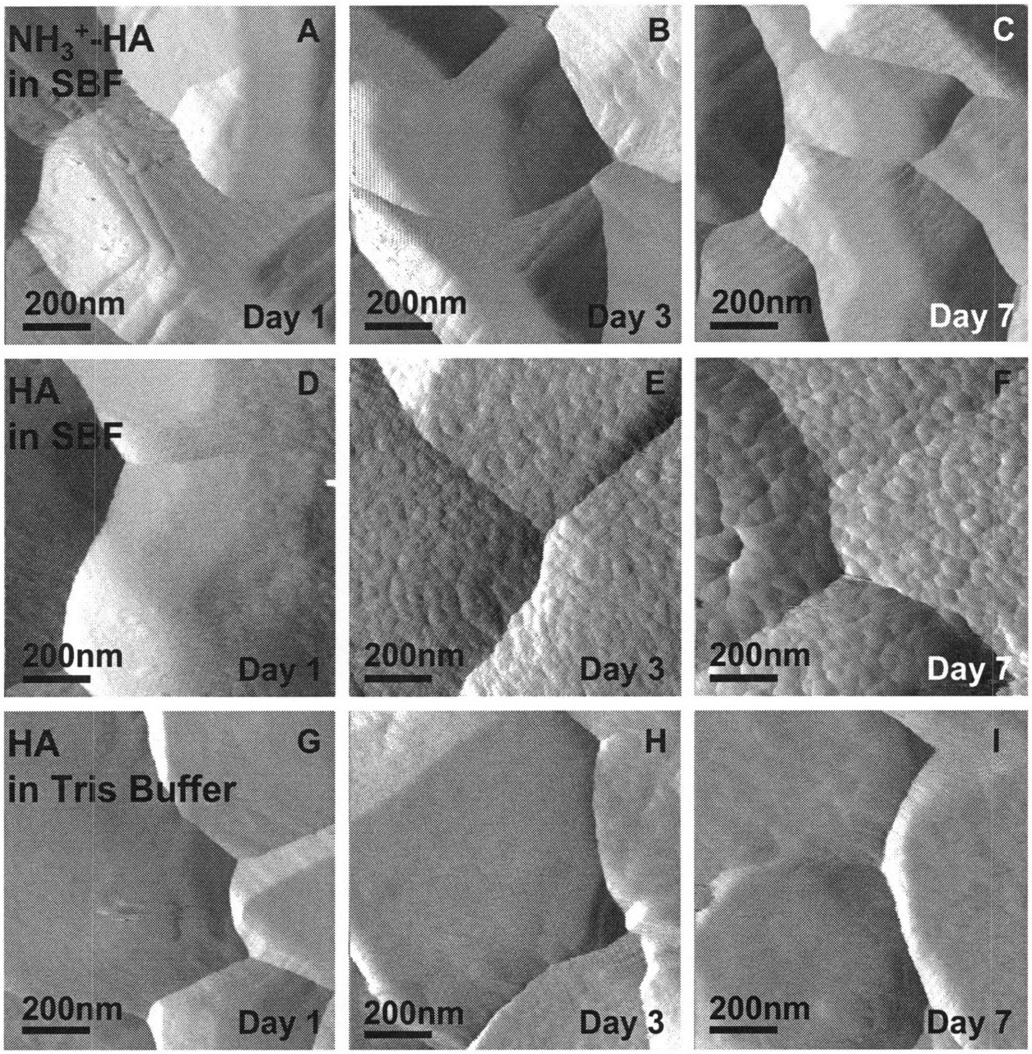

Figure 5.2: CMAFM deflection images in fluid of **A-C)** NH_3^+-HA surface incubated in SBF at 37°C for 1, 3 and 7 days, **D-F)** HA surface incubated in SBF at 37°C for 1, 3 and 7 days showing CaP precipitation and **G-I)** HA surface incubated in Tris buffer at 37°C for 1, 3 and 7 days.

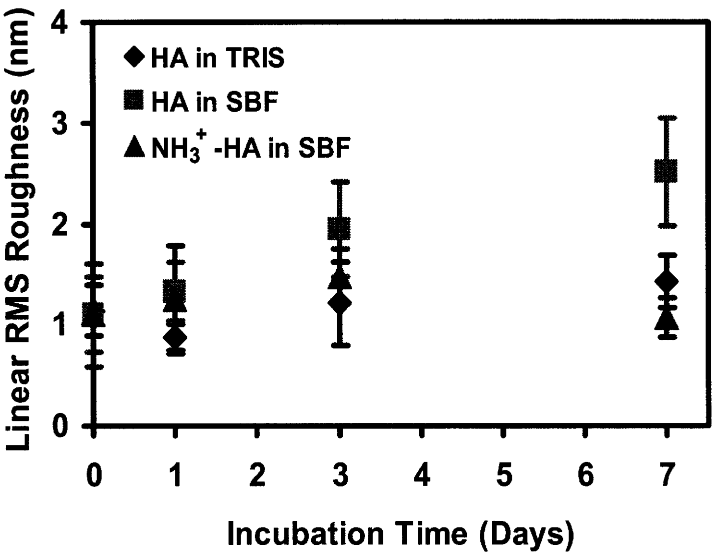

Figure 5.3: Linear RMS roughness measured from CMAFM height images in fluid of HA incubated in Tris buffer or SBF for 7 days and NH_3^+-HA incubated in SBF for 7 days.

5.3.2 Surface Forces of NH_3^+-HA

Averaged (n=20) approach F-D curves with standard deviations for 3 separate positions taken with a COO^--SAM probe tip versus the same sample before (HA) and after chemical modification (NH_3^+-HA) are shown in **Fig. 5.4**. Consistent with previous experiments [40,41], approach of the probe tip to the initial HA surface showed repulsive, nonlinear forces at $D<15$ nm due to electrostatic forces with some attractive forces at $D<5$ nm due to van der Waals forces. In contrast, the chemically-modified HA surface showed attractive, nonlinear forces on approach of the probe to the surfaces for $D<15$ nm. At very short distances the net interaction becomes repulsive, likely due to non-DLVO forces. Average Hamaker constant calculated from averaged individual curve $D_{\text{jump-to-contact}}$ at each position using **Eq. 1.3** for the surface before modification was $A_{HA} = 28 \pm 23$ zJ (n=3) and after modification it increased to $A_{NH3+\text{-}HA} = 116 \pm 194$ zJ (n=3). A_{HA} for the surface before modification is slightly larger than typically measured [40] but could be due to variations in tip geometry since van der Waals forces are more sensitive to small variations in tip geometry or surface roughness than are electrostatic forces [51,52]. Average σ_{HA} (n=3) calculated from theoretical DLVO fits to the averaged curves (n=20) for the initial HA surface shown in **Fig. 5.4** is -0.01 ± 0.004 C/m^2, consistent with previous experiments [40,41]. The average $\sigma_{NH3+-HA}$ (n=3) calculated from theoretical fits to the average (n=20) curves for the NH_3^+-HA surface shown in **Fig. 5.4** is +0.004 ± 0.001 C/m^2 and statistically different from the surface charge of the surface before modification ($p<0.05$). The HA surface was successfully modified from a negative to a positive surface.

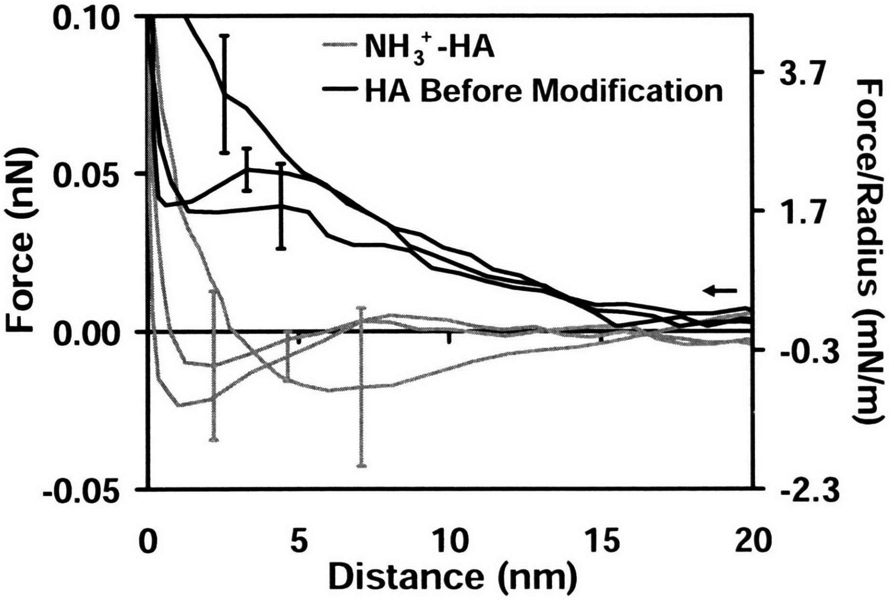

Figure 5.4: Averaged (n=20) approach F-D curves for 3 separate positions taken using the 1DMFP for COO^--SAM probe tip versus HA and NH_3^+-HA surfaces. Hi-lo bars indicate one standard deviation (R_{TIP}~44 nm, IS=0.01M, pH=7.4)

5.3.3 Surface Morphology and Roughness of CaP Layers on HA and SiHA

The initial HA and SiHA surfaces were composed of smooth faceted grains with a maximum dimension, *d*, of 1.5 ± 0.7 μm and 0.7 ± 0.4 μm, respectively, as determined via CMAFM height images (*data not shown*). **Fig. 5.5** compares TMAFM deflection images of the initial HA and SiHA surfaces with the SBF-incubated HA and SiHA surfaces. The initial HA and SiHA surfaces were found to have 200 nm linear RMS roughness of 1.1 ± 0.3 nm and 0.9 ± 0.4 nm, respectively. After incubation there is a distinct change in intragranular topography observed compared to the original HA and SiHA surfaces due to precipitation of CaP. Both the HA and SiHA surfaces were covered by a mostly continuous layer of tiny grains, through which the underlying grain boundaries are clearly visible, with occasional larger globular regions. It is unclear if the larger globular regions are due to precipitation buildup or irregularities in the underlying grain structure. Linear height profiles of "bare" regions adjacent to precipitate regions, which were rarely found, showed the precipitate layer thickness to be roughly 100 nm for both HA and SiHA. 200 nm linear RMS roughness of CaP precipitated onto HA and SiHA after 36 days incubation in SBF was found to be 3.2 ± 1.2 nm and 3.0 ± 1.3 nm, respectively, which are statistically similar ($p<0.05$) and statistically larger than initial surface roughness ($p<0.05$). Within the continuous layer of tiny grains both CaP precipitate on HA and SiHA showed regions (region I) of hemispherical, globular structures with maximum lateral diameter, d_{HA}= 44.7 ± 12.7 (n=30) nm and d_{SiHA}= 50.4 ± 15.8 nm (n=47), which were statistically similar in size ($p<0.05$). The precipitate on the HA surface also showed regions (region II) of elongated, needle-like structures (width, w= 31.0 ± 8.5 nm, d= 104.4 ± 31.1 nm, n=25) which were not observed on the SiHA surface. Separate morphologies appeared localized within individual grains or facets.

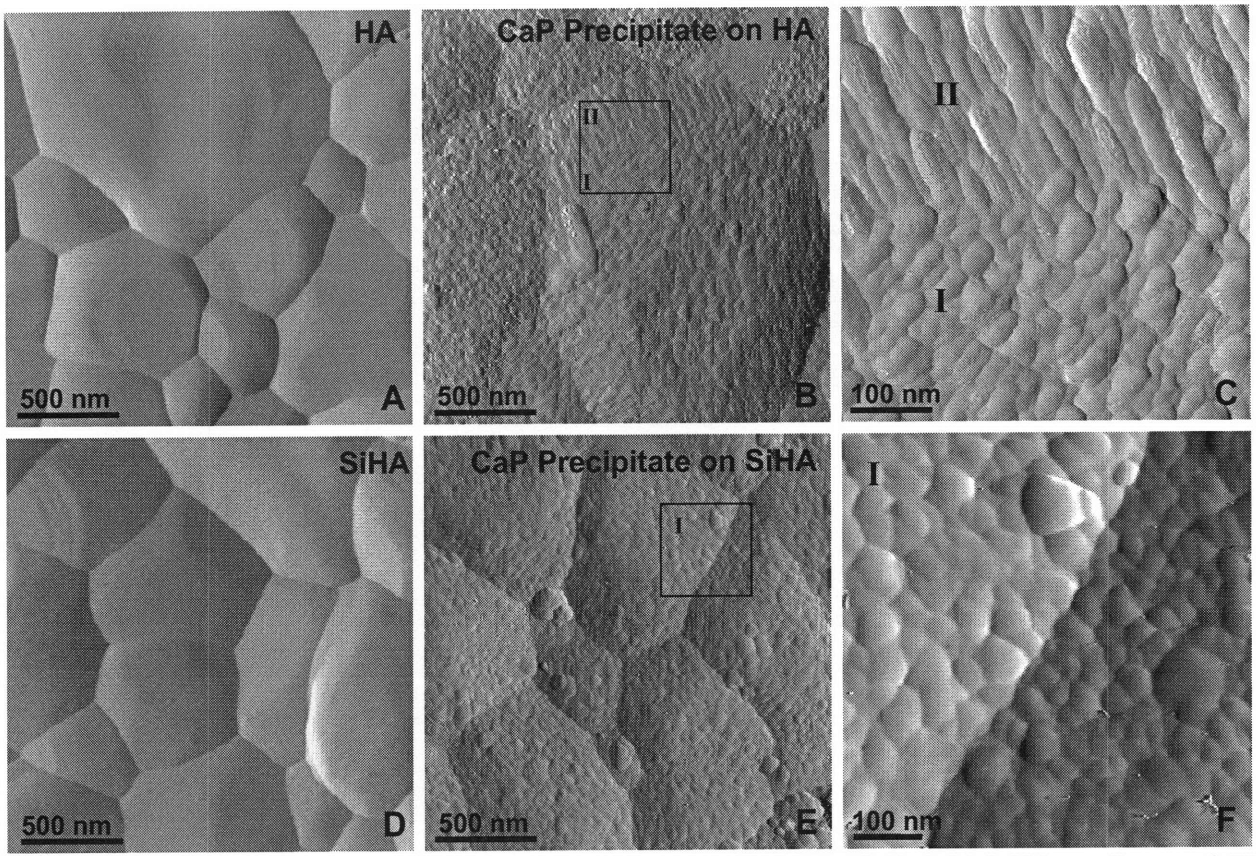

Figure 5.5: TMAFM amplitude images in ambient conditions of **A)** initial HA surface and **B)** HA surface after 36 days incubation in SBF showing two distinct CaP precipitate morphologies labeled I (hemispherical, globular) and II (elongated, needle-like). **C)** A smaller scan of the boxed area in B showing more detail of distinct morphological regions I and II. **D)** Initial SiHA surface and **E)** SiHA surface after 36 days incubation in SBF showing hemispherical, globular morphology. **F)** A smaller scan of the boxed area in E showing more detail of precipitate morphology.

5.3.4 X-ray Photoelectron Spectrometry of CaP Layers on HA and SiHA

Lu et al. demonstrated the ability to classify the biologically relevant calcium phosphate phases by measuring Ca/P ratios and analyzing O(1s) shake-up satellite peaks via XPS [53]. The XPS-measured Ca/P or Ca/(P+Si) ratios of the initial HA, SiHA, CaP precipitated on HA and SiHA were found to be 1.63, 1.54, 1.02, and 1.10, respectively. High resolution XPS scans of the O(1s) peaks for each sample are shown in **Fig. 5.6.** The shapes of the curves for the CaP precipitate on HA and SiHA are similar to each other and distinctly different from the shape of the curves for the initial HA and SiHA which are themselves similar to each other. The ratio between the O(1s) shake-up peak II area and the total area of main O(1s) peak plus shake-ups was calculated for each sample. Using the initial HA and SiHA surfaces $O(1s)_{II}/O(1s)_{Total}$ ratio as a baseline, the precipitated HA and SiHA surfaces $O(1s)_{II}/O(1s)_{Total}$ ratios were found to be 0.053 and 0.056, respectively. The Ca/P ratio and $O(1s)_{II}/O(1s)_{Total}$ ratio of the precipitated layers most closely resemble the biological calcium oxide phase octacalcium phosphate (OCP) [53].

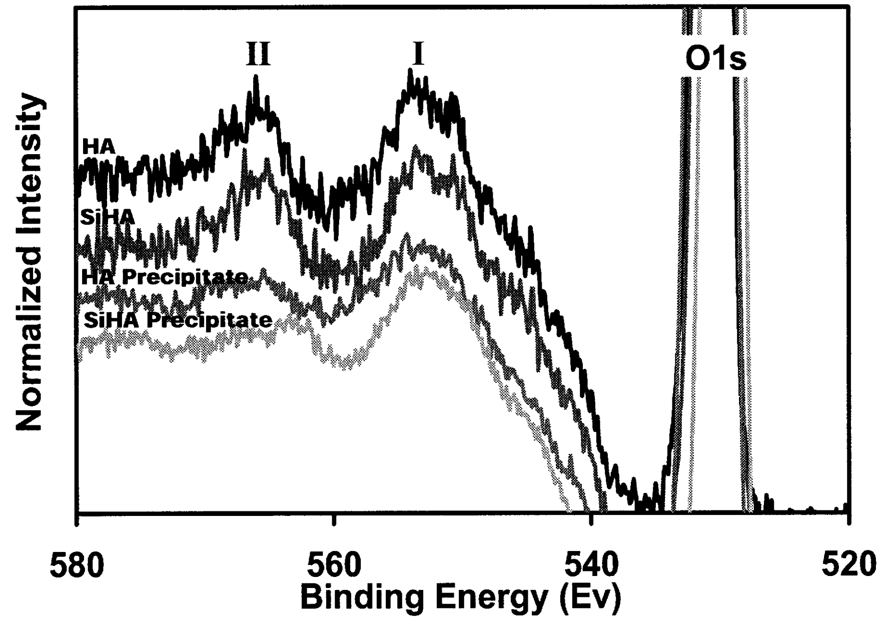

Figure 5.6: High resolution X-ray photoelectron spectroscopy scans of HA, SiHA, CaP precipitate on HA and SiHA after SBF incubation showing O(1s) main peak and shake-up satellite peaks I and II.

5.3.5 Chemically and Spatially Specific High Resolution Force Spectroscopy

5.3.5.1 CaP Layers on HA and SiHA

The 200 nm linear RMS roughness for precipitated CaP on both HA (3.2 ± 1.2 nm) and SiHA (3.0 ± 1.3 nm) is much less than R_{TIP} (~50 nm) where ~200 nm is the maximum probe tip-surface interaction area at the maximum electrostatic interaction distance (i.e. D=15 nm) [54]. **Fig. 5.7A** shows representative (for data clarity) averaged (n=10) approach F-D curves with standard deviations for the COO^-- SAM probe tip versus the CaP precipitate on both HA and

SiHA. All curves exhibit increasing, nonlinear net repulsive force (as indicated by the positive value) with decreasing separation distance for $D<15$ nm consistent with an electrostatic double layer origin for the surface interaction force and with the surface possessing a net negative surface charge. The force magnitudes and ranges of the precipitated surfaces are similar to the initial HA surface as observed previously [41]. 35% and 37% of approach curves demonstrated jump-to-contacts for the CaP precipitate on HA and SiHA respectively. From these curves average $D_{\text{jump-to-contact}}$ was determined for each position and A was calculated for each position using **Eq. 1.3**. Average $A_{\text{HA-Precipitate}}$ was found to be 12.7 ± 8.3 zJ (n=13) and average $A_{\text{SiHA-Precipitate}}$ was found to be 9.0 ± 7.0 zJ (n=11) which are statistically similar ($p<0.05$). The average $\sigma_{\text{HA-Precipitate}}$ and $\sigma_{\text{SiHA-Precipitate}}$ was then calculated for each position from theoretical fits to 5 individual curves and grouped by crystalline facet as shown in **Fig. 5.7B**. Typical individual F-D curves with theoretical fits for CaP precipitate on HA and SiHA are shown in **Fig. 5.8**. The average $\sigma_{\text{HA-Precipitate}}$ for all positions was found to be -0.013 ± 0.006 C/m^2 (n=13) slightly larger ($p<0.05$) than $\sigma_{\text{SiHA-Precipitate}}$ which was found to be -0.008 ± 0.004 C/m^2 (n=11). If surface charges of the precipitated layers are grouped, averaged by facet, and compared, the facet surface charges are statistically significant in 9/10 comparisons for precipitate on HA and 6/10 comparisons for precipitate on SiHA.

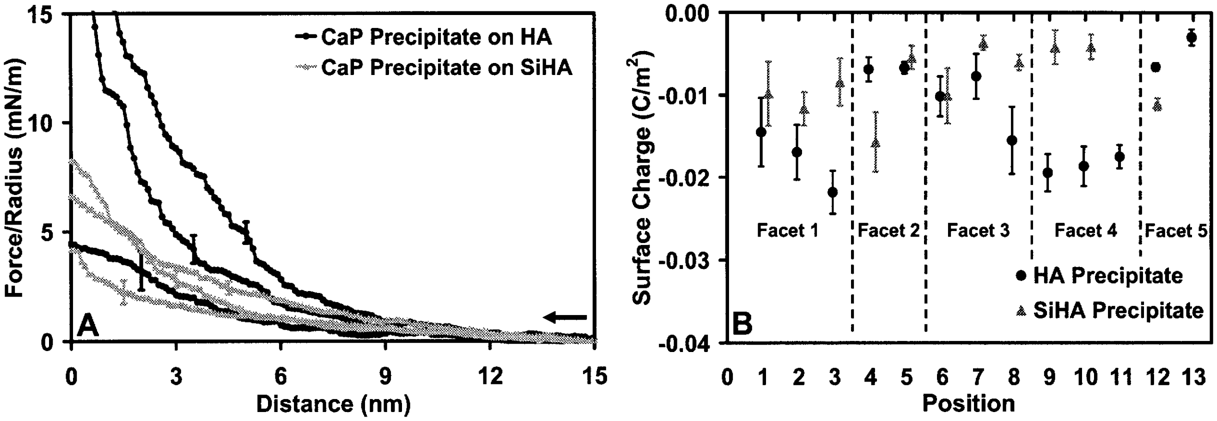

Figure 5.7: **A)** Representative averaged (n=10) approach F-D curves with standard deviations for the COO$^-$-SAM probe tip versus the CaP precipitate on both HA and SiHA for different sample positions (R$_{TIP}$(HA) ~44 nm, R$_{TIP}$ (SiHA) ~80 nm, IS=0.01, pH=7.4) **B)** Averaged (n=5) surface charge for each position of HA and SiHA precipitated surface after SBF incubation calculated by fitting individual approach F-D curves for each position to DLVO theory using the following fixed parameters: σ_{COO^-}, IS, R$_{TIP}$, and A calculated from the D$_{\text{jump-to-contact}}$ at each location.

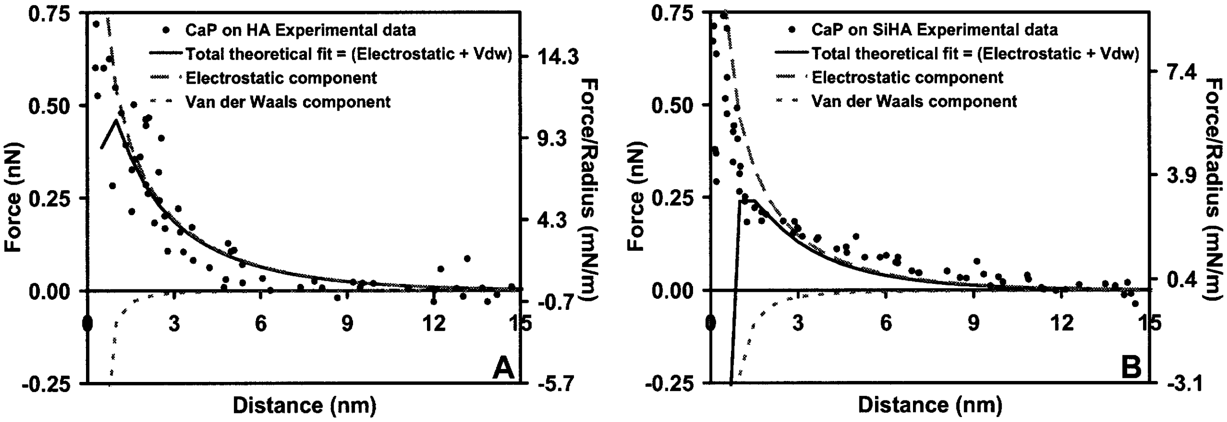

Figure 5.8: Typical individual approach F-D curves with theoretical fits showing predicted net force, as well as individual van der Waals and electrostatic components for a COO$^-$-SAM functionalized probe tip versus **A)** CaP layer on HA (σ_{COO^-} = -0.015 C/m^2, R$_{TIP}$ ~44 nm, $A_{\text{HA-Precipitate}}$= 9.3 zJ, → $\sigma_{\text{HA-Precipitate}}$ = -0.0159 C/m^2) and **B)** CaP layer on SiHA (σ_{COO^-} = -0.019 C/m^2, R$_{TIP}$ ~80 nm, $A_{\text{SiHA-Precipitate}}$= 9.1 zJ, → $\sigma_{\text{SiHA-Precipitate}}$ = -0.0039 C/m^2) in aqueous solution (pH=7.4, IS=0.01M).

The retract F-D curves for the COO^--terminated SAM probe tip versus the precipitated surfaces were also analyzed. The average adhesion distance and maximum force of adhesion for CaP precipitate on HA was 6.1 ± 3.9 nm and 0.51 ± 0.30 nN (n=13) which is statistically the same ($p<0.05$) as precipitate on SiHA which was 6.1 ± 1.3 nm (n=11) and 0.68 ± 0.58 nN (n=11).

5.3.4.2 Surface Charge of Distinct Morphologies of CaP Layers on HA

The two distinct morphologies within the CaP precipitated layer of tiny grains on HA were probed separately. A total of 37 positions from 6 different scans were probed, of which 26 positions were isotropic regions and 11 positions were elongated regions. Additionally, 7 positions on separate large globular domains were probed as well. 31% of all approach curves showed jump-to-contacts, from which a more inclusive total average $A'_{\text{HA-Precipitate}}$ was calculated to be 8.6 ± 8.3 zJ. The σ for each position was calculated from theoretical fits to averaged (n=10) approach data. **Fig. 5.10** shows the average σ for each position which ranged from -0.002 to -0.0309 C/m^2 and the over all average σ for each morphology with one standard deviation. The new total average of all positions, $\sigma'_{\text{HA-Precipitate}}$, was -0.011 ± 0.009 (n=44). Average $\sigma_{\text{elongated}}$ was -0.003 ± 0.002 (n=11), which is statistically smaller ($p<0.05$) than $\sigma_{\text{isotropic}} = -0.013 \pm 0.0082$ (n=26) and $\sigma_{\text{large}} = -0.012 \pm 0.0063$ (n=7) which were statistically similar ($p<0.05$). The new average $\sigma'_{\text{HA-Precipitate}}$ includes the previous data plus more data and is now statistically similar ($p<.05$) to $\sigma_{\text{SiHA-CaP}} = -0.008 \pm 0.004$ C/m^2 (n=11).

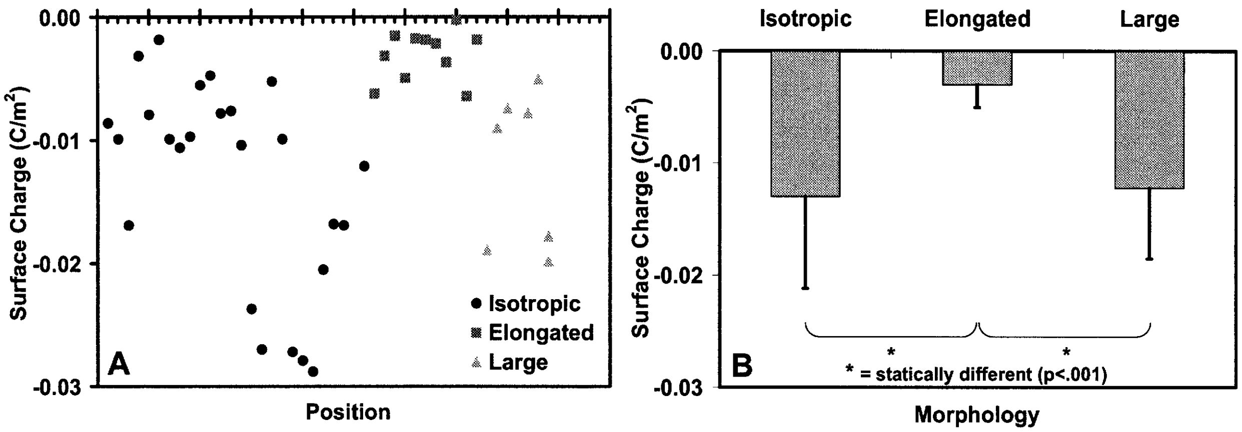

Figure 5.9: **A)** Surface charge for each position probed calculated by fitting average (n=10) approach F-D curves for each position to DLVO theory using the following fixed parameters: σ_{COO^-}, IS, R_{TIP}, and A calculated from the $D_{jump\text{-}to\text{-}contact}$ at each location.. **B)** Average surface charge of each morphological region, averaged from the surface charges in A) with one standard deviation.

5.4 DISCUSSION

5.4.1 Examination of NH_3^+ - HA

Through HRFS it was clearly shown that it is possible to chemically modify the surface of HA by conjugating surface phosphate groups to primary amine-containing molecules using the carbodiimide cross-linker EDC. A reversal of surface charge from -0.01 to +0.004 C/m^2 was obtained while keeping micro and nanoscale topography similar. The modified surface did not show CaP precipitation within 7 days of incubation in SBF although unmodified HA has shown CaP precipitation within this time. It can be concluded that the chemical modification of the HA surface prevented CaP precipitation and that a negative surface charge is necessary for CaP precipitation within a seven day incubation in SBF.

5.4.2 Chemistry and Crystal Structure of CaP Layers

Although the initial HA and SiHA surfaces had significant differences in that SiHA has increased negative surface charge, increased Hamaker constant, and increase adhesion forces over HA, as discussed previously [40], the layers precipitated onto these surfaces from SBF were found to be very similar. They are both CaP with similar Ca/P ratios (1.02 and 1.10 for HA and SiHA respectively) and both show XPS peaks characteristic of OCP [53]. The OCP crystal structure has been described as a hydrous defective apatite and consists of apatite layers separated by hydrated layers parallel to the (100) face or *c*-axis [55,56]. OCP has been identified on hydroxyapatite granules *in vitro* [24] and multiple crystalline phases of calcium phosphate including OCP were found to form during *in vivo* osseointegration on HA- β tricalcium phosphate composite bioceramics [17]. OCP is believed to be a precursor for biological apatite formation since it is a hydrated form with a faster crystallization rate and can transform through a solid-state phase transformation into the more thermodynamically stable apatite structure at physiological conditions [17,56,57]. It is consistent that OCP would have similar surface charge and Hamaker constant to the initial HA surface since the same chemistry and surface functional groups are present in the same arrangements.

5.4.3 Morphology of CaP Layers

The thickness of the precipitated CaP layers (~100 nm) observed in this study are similar in thickness to CaP layers observed *in vivo* [3,11,13] but thinner than thoes observed *in vitro* on HA granules, pellets, and coatings [22,23]. This may be due to a number of factors, including the lower solubility of fully dense, stoichiometric, phase pure HA which is known to reduce the rate of apatite precipitation [11], the decrease in Ca^{2+} ions in solution with immersion time, and the modified SBF formulation used here which has increased HCO_3^- and reduced Cl^- ion concentrations closer to those found in blood plasma compared to typical SBF formulations [1].

The main difference between the HA precipitate and the SiHA precipitated observed in this study was in the nanoscale morphology of the precipitate. It was found that precipitated CaP layers formed a mostly continuous coating of small isotropic grains with occasional larger globular regions onto the SiHA surface, but formed a mostly continuous coating of small isotropic and elongated grains with occasional larger globular regions onto the HA surface. The regions of isotropic small grains on both precipitate surfaces had statistically similar ($p<0.05$) maximum lateral diameter, d_{HA}= 44.7 ± 12.7 nm and d_{SiHA}= 50.4 ± 15.8 nm. These diameters are within the range of measured diameters of globular deposits seen *in vivo* [14,15]. Regions of elongated, needle-like grains (width, w= 31.0 ± 8.5 nm, d= 104.4 ± 31.1 nm) were observed only on the HA precipitate surface and these are very similar in size to needle-like precipitates seen *in vivo* near implanted HA granules which were 3-7 × 30-40 × 60-100 nm in size [16]. Morphological regions of precipitate appeared localized within individual grains or facets. Different facets or grains would have different exposed crystal planes and therefore differing solubility, which has been shown to have a large influence on the structure, morphology, and composition of the apatite layer [58]. Additionally, it has been shown previously that surface charge of the initial HA and SiHA surface varies with nanoscale position on the surface associated with exposed crystal plane [40,41], which could also affect apatite layer precipitation.

5.4.4 Magnitude and Positional Dependence of Surface Forces of CaP Layers

Although the initial HA and SiHA surfaces had significant differences in their surface forces, the CaP layers precipitated from SBF onto these surfaces had statistically similar surface forces, Hamaker constants (A ~10 zJ), and surface charge densities ($\sigma \sim$ -0.01 C/m^2). It has been shown previously that surface charge of HA and SiHA varies with grain and crystalline facet and that there is more of a correlation for HA than SiHA [40]. This is possibly due to substitution of SiO_4^{4-} groups into random PO_4^{3-} lattice locations which could decrease the overall surface charge inconsistently within crystal planes. Similarly, after calcium phosphate precipitation from SBF onto the HA and SiHA surface, there is variation in surface charge related to underlying facet as seen when precipitate surface charges were grouped and averaged by underlying facet. It is interesting to note there was any correlation between precipitated layer and underlying structure since in the precipitated layer, composed of small crystallites [1], a "facet" is not a single exposed crystal plane but a collection of crystallites each with a crystal plane orientation. There has been some evidence in the literature that the precipitation of calcium phosphate layers onto the HA could be a form of epitaxy [5,14,59], which could create the relationship between underlying crystal structure and precipitate crystalline structure, and therefore precipitate surface charge, as seen here. There was more correlation to underlying grains for surface charge of the HA precipitated surface (9/10 comparisons) than for the SiHA precipitated surface (6/10 comparisons). This could possibly be explained through disruption of epitaxial precipitation onto SiHA due to random substitution of SiO_4^{4-} groups into PO_4^{3-} lattice locations. This could make surface charge of the precipitated layer more dependant on underlying surface charge rather than crystal plane and we know from previous experiments that correlation for surface charge and crystal plane is less for SiHA.

5.4.5 Morphological Surface Charge Dependence of CaP Layers

Given epitaxial CaP layer growth on HA, and since the elongated CaP precipitate morphology on HA shows a smaller surface charge, it is likely the elongated morphology forms on crystal facets of lower surface charge. Since OCP crystallites are often elongated along the *c*-axis, giving it a needle-like morphology with the *c*-axis perpendicular to the length of the needle [56], one hypothesis is that the observed elongated morphology occurs when the precipitate forms with the *c*-axis parallel to surface and the observed isotropic morphology occurs when the precipitate forms with the *c*-axis perpendicular to the surface.

The orientation of CaP crystallites formed *in vivo* has been shown to be affected by implant surface properties such as surface charge. Electrically polarized, negatively charged HA (σ_{HA}~ 0.03 C/m^2 in air) has been shown to form a highly oriented bone layer after 14 days implantation in vivo. The newly formed bone on the negatively charged surface possessed crystallites with their *c*-axis perpendicular to the surface while the newly formed bone on a non-polarized surface consisted of small, irregularly shaped domains [60]. TEM studies of CaP precipitation onto SiHA and HA *in vitro* and *in vivo* have shown SiHA, which has increased negative surface charge over HA, to have increased alignment of needle-like precipitates perpendicular to the surface [9,61]. The increased alignment of CaP crystallites on polarized, more negatively charged HA and more negatively charge SiHA over conventional HA indicates that sufficient negative surface charge can selectively conduct and perpendicularly align the *c*-axis of CaP crystallites. This is consistent with the lack of elongated (*c*-axis parallel to surface) morphology seen in CaP precipitate onto SiHA. The decreased correlation between underlying facet and surface charge of precipitate is also consistent since the increased negative surface charge could overpower any epitaxial influence on CaP precipitation. Due to increased rates of *in vitro* CaP precipitation onto negatively charge self-assembling monolayers [34], increased crystal growth of bone-like HA [37] to negatively charged surfaces of electrically polarized HA, increased osteoblast-like cell growth on negatively charged surfaces of electrically polarized HA [62], and markedly enhanced *in vitro* apatite formation in simulated body fluid (SBF) [27,38,39] as well increased *in vitro* cell proliferation [63] and *in vivo* bone ingrowth [64] of more negatively charged SiHA over HA, it can be concluded that these more negatively charged surfaces are more bioactive. As these surfaces also show increased *c*-axis alignment of needle like precipitates perpendicular to the surface, perpendicular crystallites can be associated with increased bioactivity. A possible reason for the increased bioactivity of perpendicularly aligned crystallites could be the subsequent organization and alignment of collagen fibrils as has been proposed in the literature [3,9,61]. From this study, as seen in **Fig. 5.10**, the maximum negative electric charge that still allows formation of elongated precipitation, *c*-axis parallel to the surface, is approximately -0.008 C/m^2 where smaller negative charge is more likely to produce parallel precipitates and larger negative charge is more likely to produce perpendicular precipitate alignment. Therefore a negative surface charge of at least -0.008 C/m^2 in magnitude is desired for superior bioactivity.

5.5 CONCLUSION

It has been determined that a negative surface charge is necessary for CaP precipitation from SBF and that the magnitude of the charge partly determines the morphology of the precipitate. The transitional electric charge for elongated, *c*-axis parallel, to isotropic, *c*-axis perpendicular, precipitation is approximately -0.008 C/m^2 where smaller negative charge is likely to produce parallel precipitates and larger negative charge is likely to produce perpendicular precipitate alignment. Furthermore, through examination of the literature, surfaces that show increased alignment of needle like precipitates perpendicular to the surface can be associated with increased bioactivity. Therefore a negative surface charge of at least -0.008 C/m^2 is desired for superior bioactivity.

5.6 REFERENCES

[1] T. Kokubo, H. Kushitani, S. Sakka, T. Kitsugi, T. Yamamuro: *J Biomed Mater Res*; 24 (1990), p. 721.

[2] H.M. Kim: *Current Opinion in Solid State and Materials Science*; 7 (2003), p. 289.

[3] J.D. de Bruijn, C.A. van Blitterswijk, J.E. Davies: *J Biomed Mater Res*; 29 (1995), p. 89.

[4] L.L. Hench: *J Am Ceram Soc*; 81(7) (1998), p. 1705.

[5] R.Z. LeGeros, J.P. LeGeros. In: Hench LL, Wilson J, editors. *An introduction to bioceramics*. Singapore: World Scientific Publishing; (1993). p. 139.

[6] B. Feng, J.Y. Chen, S.K. Qi, L.HE, J.Z. Zhao, X.D. Zhang: *Biomaterials*; 23 (2002), p. 173.
[7] H.B. Wen, J.G.C. Wolke, J.R. de Wijn, Q. Liu, F.Z. Cui, K. de Groot: *Biomaterials*; 18 (1997), p. 1471.
[8] H.M. Kim, F. Miyaji, T. Kokubo, T. Nakamura: *J Biomed Mater Res*; 38 (1997), p. 121.
[9] A.E. Porter, N. Patel, J.N. Skepper, S.M. Best, W. Bonfield: *Biomaterials*; 25 (2004), p. 3303.
[10] P. Ducheyne, Q. Qiu: *Biomaterials*; 20 (1999), p. 2287.
[11] M. Neo, T. Nakamura, C. Ohtsuki, T. Kokubo, T. Yamamuro: *J Biomed Mater Res*; 27 (1993), p. 999.
[12] Q.Z. Chen, C.T. Wong, W.W. Lu, K.M.C. Cheung, J.C.Y. Leong, K.D.K. Luk: *Biomaterials*; 25 (2004), p. 4243.
[13] H.W. Denissen, K. de Groot, P.C. Makkes, A. van den Hooff, P.J. Klopper: *J Biomed Mater Res*; 14 (1980), p. 713.
[14] B.M. Tracy, R.H. Doremus: *J Biomed Mater Res*; 18 (1984), p. 719.
[15] F.B. Bagambias, U. Joos, W. Schilli: *J Biomed Mater Res*; 27 (1993), p. 1047.
[16] A.E. Porter, L.W. Hobbs, V.B. Rosen, M. Spector: *Biomaterials*; 23 (2002), p. 725.
[17] Y. Leng, J. Chen, S. Qu: *Biomaterials*; 24(2125-2131) (2003), p.
[18] A.C. Guyton, J.E. Hall. *Textbook of medical physiology*. Philidelphia, PA: W.B. Saunders Co.; (1996).
[19] W. Neuman, M. Neuman. *The chemical dynamics of bone mineral*. Chicago, IL: University of Chicago Press; (1958).
[20] J. Hamagami, G. Yamaguchi, K. Kanamura, T. Umegaki: *Bioceramics*; 14 (2002), p. 279.
[21] K. Onuma, A. Ito, T. Tateishi, T. Kameyama: *J cryst growth*; 154 (1995), p. 118.
[22] J.H.C. Lin, K.H. Kuo, S.J. Ding, C.P. Ju: *J Mater Sci: Mater Med*; 12 (2001), p. 731.
[23] K.A. Khor, H. Li, P. Cheang: *Biomaterials*; 24 (2003), p. 769.
[24] S.R. Radin, P. Ducheyne: *J Biomed Mater Res*; 27 (1993), p. 35.
[25] H.M. Kim, T. Himeno, T. Kokubo, T. Nakamura: *Biomaterials*; 26 (2005), p. 4366.
[26] K. Hyakuna, T. Yamamuro, Y. Kotoura, M. Oka, T. Nakamura, T. Kitsugi, et al.: *J Biomed Mater Res*; 24 (1990), p. 471.
[27] I.R. Gibson, J. Huang, S.M. Best, W. Bonfield. In: Ohgushi H, Hastings GW, Yoshikawa T, editors. *Bioceramics 12: Proceedings of the international symposium on ceramics in medicine*. River Edge, N.J.: World Scientific Publishing; (1999). p. 191.
[28] E.I. Dorozhkina, S.V. Doroshkin: *Colloids and Surf A*; 210 (2002), p. 41.
[29] A. Nakahira, M. Tamai, H. Aritani, S. Nakamura, K. Yamashita: *J Biomed Mater Res*; 62 (2002), p. 550.
[30] J. Weng, Q. Liu, J.G.C. Wolke, X. Zhang: *Biomaterials*; 18 (1997), p. 1027.
[31] J.L. Ong, G.N. Raikar, T.M. Smoot: *Biomaterials*; 18 (1997), p. 1271.
[32] N. Kanzaki, K. Onuma, A. Ito, K. Teraoka, T. Tateishi, S. Tsutsumi: *J. Phys. Chem. B*; 102 (1998), p. 6471.
[33] P.X. Zhu, Y. Masuda, K. Koumoto: *J Colloid Interface Sci*; 243 (2001), p. 31.
[34] K. Sato, Y. Kumagai, J. Tanaka: *J Biomed Mater Res*; 50 (2000), p. 16.
[35] M. Tanahashi, T. Matsuda: *J Biomed Mater Res*; 34 (1997), p. 305.
[36] S. Hayakawa, K. Tsuru, C. Ohtsuki, A. Osaka: *J Am Ceram Soc*; 82(8) (1999), p. 2155.
[37] K. Yamashita, N. Oikawa, T. Umegaki: *Chem Mater*; 8 (1996), p. 2697.

[38] C.M. Botelho, M.A. Lopes, I.R. Gibson, S.M. Best, J.D. Santos: *J Mater Sci: Mater Med*; 13 (2002), p. 1123.

[39] F. Balas, J. Perez-Pariente, M. Vallet-Regi: *J Biomed Mater Res*; 66A (2003), p. 364.

[40] J. Vandiver, D. Dean, N. Patel, C. Botelho, S. Best, J.D. Santos, et al.: *in press (J Biomed Mater Res) DOI #30737*; (2006), p.

[41] J. Vandiver, D. Dean, N. Patel, W. Bonfield, C. Ortiz: *Biomaterials*; 26 (2005), p. 271.

[42] E.J.W. Verwey, J.T.G. Overbeek, K.V. Nes. *Theory of the stability of lyophobic colloids*. New York: Elsevier Publishing Company; (1948).

[43] O. Devereux, P.L. de Bruyn. *Interaction of plane-parallel double layers*. Cambridge, MA: MIT Press; (1963).

[44] A. Sanfeld. *Thermodynamics of charged and polarized layers*. Bath, UK: Wiley-Interscience; (1968).

[45] M. Akao, H. Aoki, K. Kato: *J Mater Sci*; 16 (1981), p. 809.

[46] I.R. Gibson, S.M. Best, W. Bonfield: *J Biomed Mater Res*; 44 (1999), p. 422.

[47] E.W. van der Vegte, G. Hadziioannou: *J Phys Chem B*; 101 (1997), p. 9563.

[48] www.piercenet.com.

[49] A.C. Tas: *J Eur Ceram Soc*; 20 (2000), p. 2389.

[50] J. Seog, D. Dean, A.H.K. Plass, S. Wong-Palms, A.J. Grodzinsky, C. Ortiz: *Macromolecules*; 35(14) (2002), p. 5601.

[51] R.F. Considine, C.J. Drummond: *Langmuir*; 17 (2001), p. 7777.

[52] S. Bhattacharjee, C.-H. Ko, M. Elimelech: *Langmuir*; 14 (1998), p. 3365.

[53] H.B. Lu, C.T. Campbell, D.J. Graham, B.D. Ratner: *Anal Chem*; 72 (2000), p. 2886.

[54] M. Rixman, D. Dean, C. Macias, C. Ortiz: *Langmuir*; 19(15) (2003), p. 6202.

[55] M. Mathew, S. Takagi: *J Res Natl Inst Stand Technol*; 106 (2001), p. 1035.

[56] W.E. Brown, J.P. Smith, F.R. Lehr, A.W. Frazier: *Nature*; 196 (1962), p. 1048.

[57] M.S. Tung, W.E. Brown: *Calcif Tissue Int*; 37 (1985), p. 55.

[58] A.E. Porter, N. Patel, J.N. Skepper, S.M. Best, W. Bonfield: *Biomaterials*; 24 (2003), p. 4609.

[59] V.A. Dubok: *Powder Metallurgy and Metal Ceramics*; 39(7-8) (2000), p. 381.

[60] T. Kobayashi, S. Nakamura, K. Yamashita: *J Biomed Mater Res*; 57 (2001), p. 477.

[61] A. Porter, C. Botelho, M. Lopes, J. Santos, S. Best, W. Bonfield: *J Biomed Mater Res*; 69 (2004), p. 690.

[62] M. Ohgaki, T. Kizuki, M. Katsura, K. Yamashita: *J Biomed Mater Res*; 57 (2001), p. 366.

[63] C.M. Botelho, R.A. Brooks, S.M. Best, M.A. Lopes, J.D. Santos, N. Rushton, et al. In: Barbosa MA, Monteiro FJ, Correia R, Leon B, editors. *Bioceramics 16: Proceedings of the international symposium on ceramics in medicine*. Uetikon-Zuerich, Switzerland: Trans Tech Publications; (2004). p. 845.

[64] N. Patel, S.M. Best, W. Bonfield, I.R. Gibson, K.A. Hing, E. Damien, et al.: *J Mater Sci: Mater Med*; 13 (2002), p. 1199.

CHAPTER 6: Observation of *in vitro* Osteocalcin Regulation of Calcium Phosphate Precipitation via Atomic Force Microscopy

6.1 INTRODUCTION

The precipitation of calcium phosphate (CaP) layers onto bone implant materials *in vivo* is considered essential for strong bone bonding [1-3]. It has been demonstrated that CaP layers can be precipitated *in vitro* on bioactive ceramics from acellular protein-free SBF [1,4-8] and the formation of these layers *in vitro* is considered one method of assessing a material's bioactivity [1,7,9]. Because CaP layers can form from SBF devoid of biomolecules or cells [2,10] the formation of CaP layers on bioactive materials has been believed to be mainly a material dependant inorganic chemical process. Despite this conclusion, *in vitro* and *in vivo* experiments have found significant differences in CaP precipitation rates in that *in vitro* experiments typical take ~30 days to form a surface CaP layer on dense synthetic HA [6,11], whereas *in vivo* experiments have found CaP layer formation in less than 2 weeks [3,10], which indicates there is some affect from the biological environment.

The influence of biological macromolecules on the precipitation of CaP layers is currently being investigated [12-15], in particular osteocalcin (OC) [13,16,17]. OC is a small bone protein comprising up to 20% of non-collageneous bone tissue proteins [13,18] and contains two or three residues of γ-carboxyglutamic acid yielding strong Ca^{2+} binding affinity through the carboxyl groups of Gla residues of which there are 6-9 coordination sites of Ca^{2+}. It is believed that OC interacts with both the Ca^{2+} in the bone mineral crystal lattice as well as with Ca^{2+} ions in solution to affect mineralization process [17]. *In vitro* experiments on brushite show that OC accelerates nucleation and regulates growth of precipitated CaP crystals at concentrations of 0.25 mg/mL [17]. OC inhibited CaP crystal growth on seed hydroxyapatite

(HA) crystals *in vitro* at concentrations of 5 µg/mL. Other data has shown 100 µg/mL to be the minimum concentration needed to induce nucleation of HA and that concentrations over 10 µg/mL but below 100 µg/mL inhibited both nucleation and growth processes of HA in a steady-state agarose gel system [13]. The exact mechanisms of OC regulation of CaP precipitation and the origin of concentration dependence are currently unknown. However, there is some thought that due to strong Ca^{2+} binding affinity OC in solution might sequester Ca^{2+} ions away and inhibit precipitation [13]. This is supported by the lack of inhibition when OC is immobilized by attachment to agarose beads [19].

Most often, the rate of mineral precipitation is assessed through loss of calcium or phosphate ions from the incubating solution or by the amount of hydroxyl ions added for pH to remain constant. This is not conducive to determining precisely how OC affects precipitation morphology. This study utilizes tapping mode atomic force microscopy (TMAFM) which enables spatial resolutions of <1 nm to visualize the ultrastructural morphology of CaP layers precipitated *in vitro* from SBF onto dense synthetic polycrystalline hydroxyapatite in the presence of OC at varied concentrations from 1 µg/ml to 120 µg/ml.

6.2 MATERIALS AND METHODS

6.2.1 Sample Preparation

Synthetic, phase pure, dense, polycrystalline HA pellets (~1 cm in diameter) were synthesized as described in Section 1.2.1 [20]. The pellets were embedded in an epoxy resin (Araldite 502), and cut by diamond saw into pieces approximately 4 mm × 4 mm × 2 mm. The surfaces of the pieces were then polished on a uni-pol polisher (*Geoscience Instruments Corp.*), first using a 45 µm grit diamond grinding disk, then *Metadi* diamond suspensions 15 µm, 6 µm and 1 μm, followed by a final step using 0.2 μm diameter colloidal silica. The samples were then sonicated in deionized (DI) water to remove particulates, etched for 90 seconds in 2% citric acid to expose grain structure, then sonicated once more in DI water and dried in air. SBF was prepared by dissolving reagent grade NaCl, $NaHCO_3$, KCl, $Na_2HPO_4 \cdot 2H_2O$, $MgCl_2 \cdot 6H_2O$, $CaCl_2$, Na_2SO_4 in Millipore water and buffering at pH 7.4 and 37°C with trihydroxymethyl aminomethane (Tris buffer, $(CH_2OH)_3CNH_2$) and small amounts of HCl [1,21]. Solutions containing the following concentrations of purified bovine OC (*Biodesign*, Product No. A95020B) in SBF were made: 1 μg/mL, 5 μg/mL, 20 μg/mL, and 120 μg/mL. Each sample was placed in 2 mL of its solutions, with a control sample placed in 2 mL SBF without OC, and incubated for 32 days at 37°C, after which they were rinsed with DI water and dried with N_2 gas.

6.2.2 Sample Characterization

TMAFM with Olympus AC240TS-2 rectangular Si cantilevers (probe tip end radius, R_{TIP} <10 nm, cantilever spring constant, k_c ~2 N/m) was employed to image surface topography at high resolutions in ambient conditions at a scan rate of 1 htz using a *Veeco Digital Instruments* Nanoscope IIIA System Controller and Multimode AFM. A *Kratos* AXIS Ultra Imaging X-ray Photoelectron Spectrometer (XPS) with AlKα X-ray source was used to analyze the initial HA surface and the CaP precipitated surfaces from SBF with no OC and with 120 μg/ml OC at a take-off angle of 0° (penetration depth < 10 nm).

6.3 RESULTS

6.3.1 Tapping Mode Atomic Force Microscopy

Representative TMAFM amplitude images are show in **Fig. 6.1** illustrating qualitative difference between samples. The initial polished and etched surface has distinctive grains but the intergrain surfaces are quite smooth. The 0 μg/ml and 1 μg/ml samples showed precipitate as non-continuous globular regions with the underlying grain structure clearly visible. The 5 μg/ml and 20 μg/ml samples show no precipitate as their surfaces are smooth and similar to the initial surface. The 120 μg/ml sample showed similar precipitate to the 0 μg/ml and 1 μg/ml samples. Qualitative observations are supported by roughness analysis performed on these images. A total of 9 roughness profiles 300-400 nm across representative areas of the surface within the facets of the underlying grain structure clearly seen through the precipitate were obtained from several 1 μm × 1 μm images of each sample. The average intragranular linear root-mean-squared (RMS) roughness of the height profiles (after subtraction of the baseline slope of the underlying facet) was calculated and is shown in **Fig. 6.2**. The surface roughnesses are as follows: initial = 1.6 ± 0.2 nm, 0 μg/mL OC roughness = 3.2 ± 0.8 nm, 1 μg/mL OC roughness = 3.2 ± 0.6 nm, 5 μg/mL OC roughness = 1.9 ± 0.5 nm, 20 μg/mL OC roughness = 1.9 ± 0.3 nm, and 120 μg/mL OC roughness = 3.3 ± 0.8 nm.

The samples incubated in SBF with 0 μg/mL OC, 1 μg/mL OC, and 120 μg/mL OC were statistically rougher than the initial surface ($p<0.05$). There was no statistical difference in roughness between the initial surface and the samples incubated in SBF with 5 μg/mL OC and 20 μg/mL OC. Samples incubated in SBF with 0 μg/mL OC, 1 μg/mL OC, and 120 μg/mL OC were not statistically different in roughness from each other and neither were samples incubated in 5 μg/mL OC and 20 μg/mL.

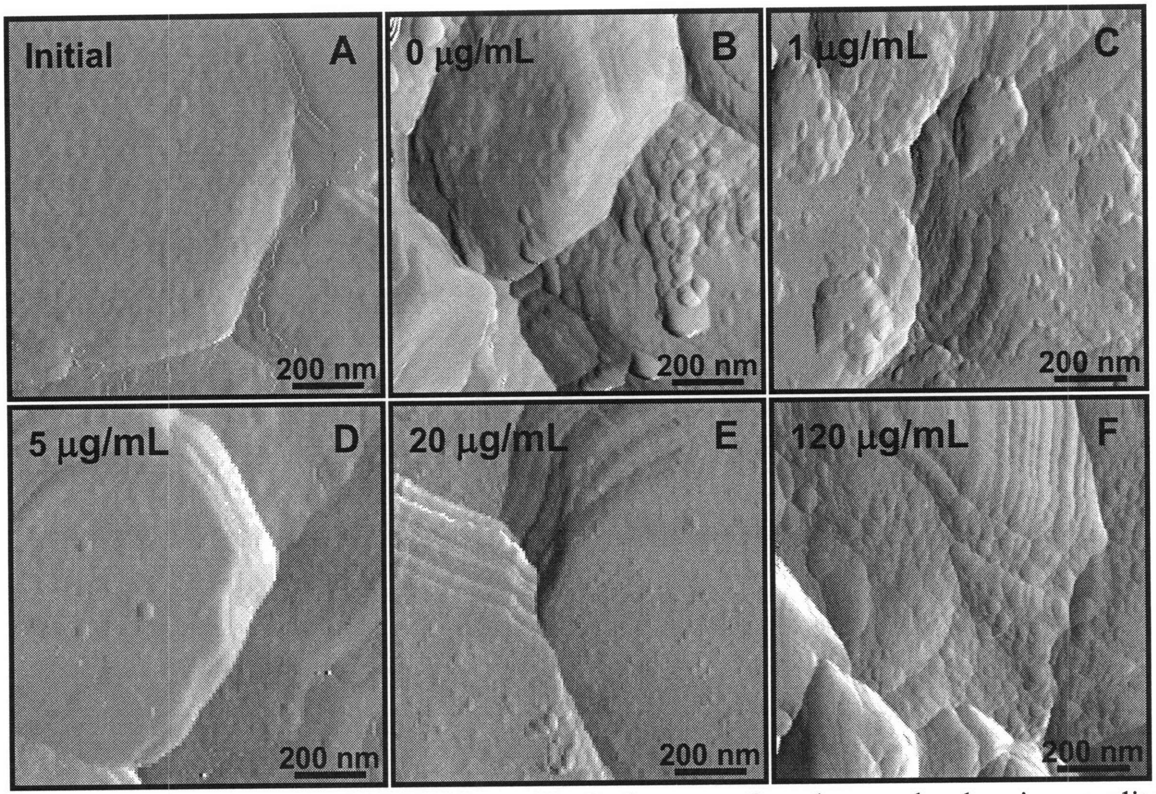

Figure 6.1: Representative TMAFM amplitude images of each sample showing qualitative differences in roughness due to CaP layer precipitation. **A)** Initial polished and etched surface **B-F)** samples incubated in SBF for 32 days with 0, 1, 5, 20 and 120 μg/mL OC added, respectively.

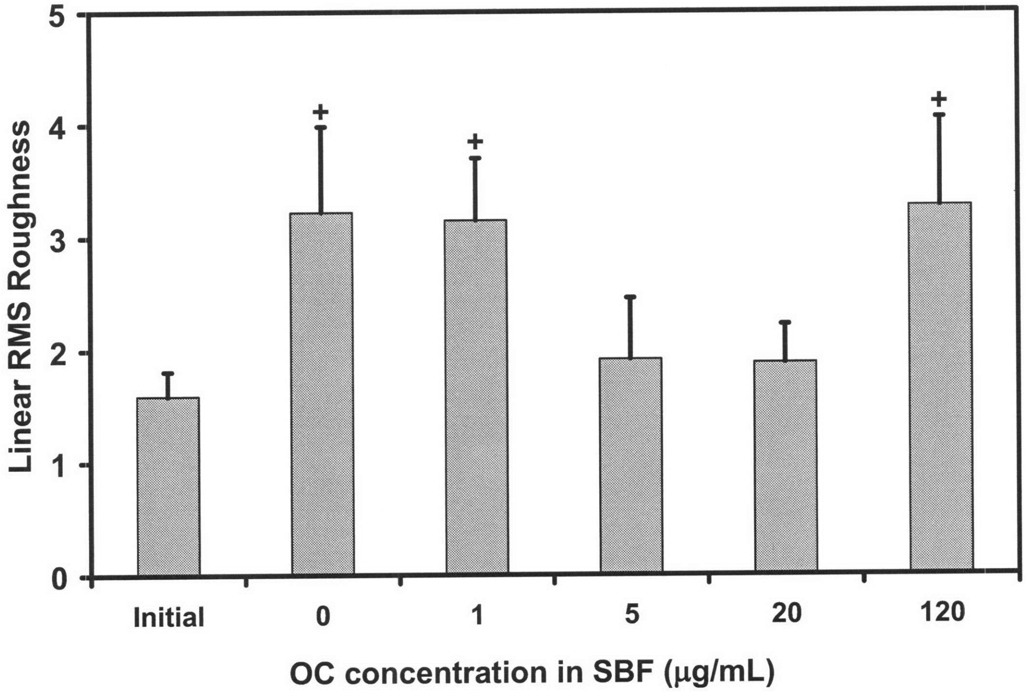

Figure 6.2: Average (n=9) linear RMS roughness and one standard deviation of each sample. (+) denotes samples with statistically greater ($p<0.05$) roughness than initial surface.

6.3.2 X-ray Photospectroscopy

Lu et al. has demonstrated the ability to classify the biologically relevant calcium phosphate phases by measuring Ca/P ratios and ratios of O(1s) shake-up satellite peak areas via XPS [22]. The measured Ca/P ratios of the initial HA surface and the precipitated surface from SBF without OC and with 120 μg/mL OC were 1.63, 1.02, 1.35 respectively. A high resolution XPS scan of the O(1s) peak is shown in **Fig. 6.3** and the ratio between the O(1s) shake-up peak II area and the total area of main O(1s) peak plus shake-ups was calculated. Using the initial HA surface $O(1s)_{II}/O(1s)_{Total}$ ratio as a baseline, both precipitated HA surfaces had a $O(1s)_{II}/O(1s)_{Total}$ ratio = .053. The Ca/P ratio and $O(1s)_{II}/O(1s)_{Total}$ ratio of the precipitated layers most closely resembles the biological calcium oxide phase octacalcium phosphate (OCP).

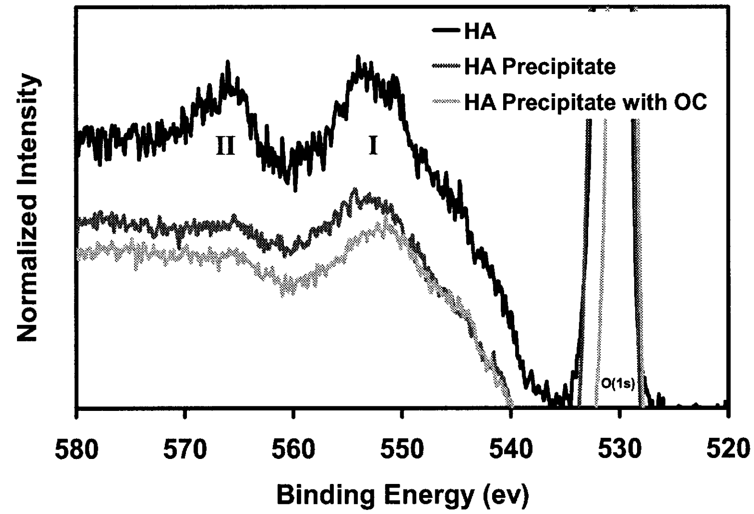

Figure 6.3: High resolution X-ray photoelectron spectroscopy scan of HA, CaP precipitation onto HA from SBF and SBF containing 120 μg/mL of OC showing O(1s) peak and shake-up satellite peaks I and II.

6.4 DISCUSSION

The CaP precipitated layers formed here were less distinct than precipitated CaP layers studied previously in Chapter 5. Overall precipitate quantities were small and the precipitated layer is non-continuous, likely due to small SBF incubation volume and lack of SBF refreshing which were required to incubate samples in high concentrations of limited proteins. Areas of precipitation did show globular isotropic and elongated morphology similar to those seen before. XPS curves of the precipitate formed in the presence of OC were very similar to those formed without OC and it appears the precipitate structure is similarly OCP. One significant difference is that the Ca/P ratio for the precipitated layer in the presence of 120 μg/mL OC was larger (1.35) than that for the precipitated layer without OC (1.02). The incorporation of OC into the precipitated layers with its Ca^{2+} binding sites filled could account for the higher Ca/P ratio.

From the results, it can be seen that concentrations of OC greater than 1 μg/mL in SBF inhibit the precipitation of CaP layers, but at 120 μg/mL, this inhibiting effect is absent. These results agree with previously published literature that found concentrations over 10 μg/mL OC to inhibit CaP layer formation [13,17]. However, a higher concentration of OC was not found to promote the formation of CaP layers, only to stop inhibition. The samples incubated in SBF with 0 μg/mL OC, 1 μg/mL OC, and 120 μg/mL OC did not show noticeable differences in morphology from each other.

The importance of the biological environment has already been established in the case of natural bone mineralization. Mineral deposition will not occur without a matrix, which contains both collagenous and non-collagenous proteins, and it was found that matrix proteins can initiate mineralization and regulate the growth, proliferation, or agglomeration of mineral crystals, by either stabilizing crystal nuclei or binding to the crystal surface [12]. Thus, many proteins have been proposed to function as regulators of the mineralization process, either as nucleators or inhibitors of crystal formation [13,23].

OC has a high affinity for Ca^{2+} ions [18], and has been shown to act as an inhibitor of mineralization in solution at low concentrations [13,23]. Bound Ca^{2+} ions induce a helical conformation in osteocalcin which is important for the adsorption of osteocalcin to HA [18]. Osteocalcin has 6-9 coordination sites and can bind to free Ca^{2+} ions as well as to HA at the same time [18]. At low concentrations of OC (5 μg/mL and 20 μg/mL), the protein in solution because of its high affinity for Ca^{2+} and the large excess of Ca^{2+} ions compared to protein molecules, may have no free sites with which to bind to HA and so it acts only to remove free Ca^{2+} ions from solution. This could subsequently hinder the deposition of Ca^{2+} onto the HA surface, disrupting the natural formation of CaP layers. However, at very low concentrations of OC (1 μg/mL), there would not be enough OC to remove a significant quantity of Ca^{2+} ions, so precipitation occurs normally. At very high concentrations of OC there will be a larger ratio of protein to free Ca^{2+} ions allowing OC to adhere to the HA surface, becoming immobilized, and possibly acting as a nucleator [19]. It is believed that the accumulation of Ca^{2+} ions on the HA surface serves to initiate the formation of CaP layers [24-29].

6.5 REFERENCES

[1] T. Kokubo, H. Kushitani, S. Sakka, T. Kitsugi, T. Yamamuro: *J Biomed Mater Res*; 24 (1990), p. 721.

[2] H.M. Kim: *Current Opinion in Solid State and Materials Science*; 7 (2003), p. 289.

[3] J.D. de Bruijn, C.A. van Blitterswijk, J.E. Davies: *J Biomed Mater Res*; 29 (1995), p. 89.

[4] J. Hamagami, G. Yamaguchi, K. Kanamura, T. Umegaki: *Bioceramics*; 14 (2002), p. 279.

[5] K. Onuma, A. Ito, T. Tateishi, T. Kameyama: *J cryst growth*; 154 (1995), p. 118.

[6] J.H.C. Lin, K.H. Kuo, S.J. Ding, C.P. Ju: *J Mater Sci: Mater Med*; 12 (2001), p. 731.

[7] Y. Leng, J. Chen, S. Qu: *Biomaterials*; 24(2125-2131) (2003), p.

[8] K.A. Khor, H. Li, P. Cheang: *Biomaterials*; 24 (2003), p. 769.

[9] P. Ducheyne, Q. Qiu: *Biomaterials*; 20 (1999), p. 2287.

[10] M. Neo, T. Nakamura, C. Ohtsuki, T. Kokubo, T. Yamamuro: *J Biomed Mater Res*; 27 (1993), p. 999.

[11] I.R. Gibson, J. Huang, S.M. Best, W. Bonfield. In: Ohgushi H, Hastings GW, Yoshikawa T, editors. *Bioceramics 12: Proceedings of the international symposium on ceramics in medicine*. River Edge, N.J.: World Scientific Publishing; (1999). p. 191.

[12] A.L. Boskey: *Connect Tissue Res*; 35 (1996), p. 357.

[13] G.K. Hunter, P.V. Hauschka, A.R. Poole, L.C. Rosenberg, H.A. Goldberg: *Biochem J*; 317 (1996), p. 59.

[14] S. Radin, P. Ducheyne: *J Biomed Mater Res*; 30 (1996), p. 273.

[15] R. Rohanizadeh, M. Padrines, J.M. Bouler, D. Couchourel, Y. Fortun, G. Daculsi: *J Biomed Mater Res*; 42 (1998), p. 530.

[16] A.L. Boskey, F.H. Wians, P.V. Hauschka: *Calcif Tissue Int*; 37 (1985), p. 57.

[17] K. Flade, C. Lau, M. Mertig, W. Pompe: *Chem Mater*; 13 (2001), p. 3596.

[18] P. Hauschka, L. JB, C. DEC., G. CM: *Physiol Rev*; 69(3) (1989), p. 990.

[19] A. Linde, A. Lussi, M. Crenshaw: *Calcif Tissue Int*; 44 (1989), p. 286.

[20] M. Akao, H. Aoki, K. Kato: *J Mater Sci*; 16 (1981), p. 809.

[21] A.C. Tas: *J Eur Ceram Soc*; 20 (2000), p. 2389.

[22] H.B. Lu, C.T. Campbell, D.J. Graham, B.D. Ratner: *Anal Chem*; 72 (2000), p. 2886.

[23] R.W. Romberg, P.G. Werness, B.L. Riggs, K.G. Mann: *Biochem*; 25 (1986), p. 1176.

[24] C.M. Botelho, M.A. Lopes, I.R. Gibson, S.M. Best, J.D. Santos: *J Mater Sci: Mater Med*; 13 (2002), p. 1123.

[25] T. Himeno, H.-M. Kim, H. Kaneko, M. Kawashita, T. Kokubo, T. Nakamura. In: Besim Ben-Nissan DS, William Walsh, editor. *Bioceramics 15: Proceedings of the international symposium on ceramics in medicine*. Uetikon-Zuerich, Switzerland: Trans Tech Publications; (2003). p. 457.

[26] K. Sato, Y. Kumagai, J. Tanaka: *J Biomed Mater Res*; 50 (2000), p. 16.

[27] M. Tanahashi, T. Matsuda: *J Biomed Mater Res*; 34 (1997), p. 305.

[28] K. Yamashita, N. Oikawa, T. Umegaki: *Chem Mater*; 8 (1996), p. 2697.

[29] K.S. Hwang, J.E. Song, J.W. Jo, H.S. Yang, Y.J. Park, J.L. Ong, et al.: *J Mater Sci: Mater Med*; 13 (2002), p. 133.

CHAPTER 7: Human Osteoblast Response to Micro- and Nanostructured Hydroxyapatite and Calcium Phosphate Precipitate

7.1 INTRODUCTION

When the bioactive ceramic hydroxyapatite (HA) is implanted into a bony site, it interacts first with biological fluid. Serum proteins adsorb concurrently with solution-mediated chemical reactions such as dissolution, precipitation and ion exchange reactions [1] which lead to the formation of globular accretions that merge to form mostly continuous organic and mineral calcium phosphate (CaP) interfacial layers to which collagen fibers attach [1-3]. The interaction of bone cells with HA is thought to be mediated by these interfacial layers [1-4]. Osteoblasts and their progenitors attach to these layers, differentiate, and begin synthesizing new bone [1,5]. In some instances bone cells do interact directly with the HA surface, but this is usually where the implant borders on bone marrow [4].

The response of osteoblasts to materials in cell culture is an established method of predicting *in vivo* behavior, and many studies of osteoblast response to calcium phosphate ceramics have been done to look at the effect of composition [6,7], Ca/P ratio [8], solubility [9,10], roughness [11], and porosity [12]. However, while many studies have been performed on the interaction of osteoblasts directly with the bioceramic surface, there has been little examination of how bone cells interact with precipitated CaP layers on bioactive ceramics. It has been demonstrated that CaP layers similar to those formed *in vivo*, without the organic constituents, can be precipitated *in vitro* on bioactive ceramics such as HA from acellular protein-free simulated body fluid (SBF), an aqueous electrolyte solution that mimics the ionic concentrations and pH of human blood plasma [13-18].

The precipitation of CaP layers onto dense microstructured, polycrystalline HA (micronHA) from SBF has been examined in depth previously (**Chapter 5**) and it has been found that the nanoscale surface forces, i.e. surface charge density and van der Waals Hamaker constant of the CaP precipitate is similar to the underlying initial surface. However, the crystal structure, and Ca/P ratio are different in that the precipitate has an octacalcium phosphate (OCP) crystal structure with a much lower Ca/P ratio (1.02) than the initial HA surface (1.63). *In vitro* studies have found protein adsorption from serum [19] and initial cell attachment [8] to HA to depend on Ca/P ratio and hence, may have important consequences for subsequent cellular interactions. Additionally, the CaP precipitated layer is formed of nanoscale globular deposits ~50 nm in diameter which increases the nanoscale intragrain surface roughness.

It is widely recognized that surface topology on both a micro and nano scale significantly influences cell response [11,20-24] and generally rougher surfaces have increased cell response [11,24,25]. Surface roughness of HA has been correlated with increased *in vitro* human bone marrow stromal cell attachment and adhesion [11] and i*n vivo* studies have shown roughened surfaces to have stronger bone fixation [26]. Nanostructured ceramics such as alumina, titania, and hydroxyapatite with grain sizes less than 100 nm and increased nanoscale roughness have shown increased bioactivity through enhanced protein adsorption [27], osteoblast adhesion [28] and osteoblast function [29] over their respective non-nanostructured ceramics. Previous studies (**Chapter 4**) on micronHA compared to nanoHA have shown them to have similar crystal structure, a slightly lower Ca/P ratio of 1.45, similar nanoscale surface forces, i.e. surface charge and Hamaker constant, but very different surface morphology (e.g. grain size and density of grain boundaries, topographical curvature, surface roughness, and underlying slope).

In this study, human osteoblasts were cultured on micronHA, a CaP layer precipitated from simulated body fluid (SBF) onto micronHA, and nanoHA [30,31] to observe how these different surfaces might affect osteoblast attachment, spreading, and differentiation. The techniques used include a cell proliferation assay, fluorescence microscopy, and real-time reverse transcription polymerase chain reaction (PCR). Additionally, the adsorption of the adhesion protein fibronectin, which has been shown to mediate osteoblast attachment and spreading [32,33], was examined to illuminate the relationship between surface morphology, protein adhesion, and osteoblast response.

7. 2 MATERIALS AND METHODS

7.2.1 Sample Preparation and Characterization

MicronHA pellets were synthesized using an aqueous precipitation chemical route between calcium hydroxide and orthophosphoric as described in **Section 1.2.1** [34]. Dense, phase pure, monolithic samples of nanostructured polycrystalline HA (nanoHA) were donated by *Angstrom Medica* (Woburn, MA). Briefly, it was prepared through an aqueous precipitation reaction between analytical grade $Ca(NO_3)_2{\cdot}4H_2O$ and $(NH_4)_2HPO_4$. The precipitate was washed, ground, dried, and aged with processing parameters such as solution pH, aging time and temperature adjusted to achieve desired ultrafine spherical particles which were then subjected to pressure-assisted sintering at 90°C for 30 minutes at a pressure of 100 MPa. The resulting material is transparent and 98.5% of theoretical density of HA [30,31]. Phase purity of initial materials was verified through X-ray diffraction (XRD) using a *Rigaku* Rotaflex X-ray diffractometer with Cu X-ray source. Data was collected between 25° and 40° 2θ using a step size of 0.02° and a count time of 2.5 seconds. Phase identification was accomplished by comparing the peak positions of the diffraction patterns with ICDD (JCPDS) standards.

The top surface of the nanoHA samples were polished on a uni-pol polisher (*Geoscience Instruments Corp.*), first using a *Bueler* ultra-prep 45 μm grit diamond grinding disk, then *Metadi* diamond suspensions 15 μm, 6 μm and 1 μm, followed by a final step using *MasterMet* 0.2 μm diameter colloidal silica. The samples were then sonicated in deionized (DI) water to remove particulates, etched for 90 seconds in 2% citric acid to expose grain structure, sonicated once more in DI water and dried with N_2 gas. CaP precipitate layer samples were created by incubating micronHA in SBF for 36 days at 37°C to form a CaP layer.

Tapping mode AFM (TMAFM) with *Olympus* AC240TS-2 rectangular Si cantilevers (spring constant k=2 N/m) was employed to image topography, grain size, and surface roughness of each sample at high resolutions in ambient conditions with a *Veeco* (*Digital Instruments)* Nanoscope IIIA System Controller and Multimode AFM. Grain size was measured through digital diameter measurements using the image analysis program SigmaScan Pro (*Systat Software, Inc.*). Surface roughness was measured on a larger scale, including grains, through RMS roughness analysis of four 3 μm scans and on a smaller (intragranular) scale through linear RMS roughness of four 800 nm long height profiles, from which the slope of the underlying grain or surface was subtracted. Wettability of the samples was assessed via contact angle measurements with deionized (DI) water on a Video Contact Angle System 2000, *AST Inc.*

7.2.2 Protein Adhesion

MicronHA, CaP layer, and nanoHA samples were incubated in McCoy's modified medium plus 10% fetal bovine serum (*VWR*) overnight at 37°C. One sample of each was stained for fibronectin. After incubation in serum, each sample was rinsed 3× with phosphate buffered saline (PBS) and then washed with 3% bovine serum albumin (BSA) in PBS for 5 minutes at 37°C to block non-specific binding. Then the samples were incubated in anti-fibronectin rabbit polyclonal antibody (*abcam*, Product No. ab23752) at a dilution of 1:40 in PBS for 1 hour at room temperature followed by 3× PBS rinse. Then the samples were incubated in the secondary, FTIC conjugated goat anti-rabbit antibody (*abcam*, Product No. ab6717) at a dilution of 1:100 in PBS for 1 hour at room temperature followed by 3× PBS rinse. Images of stained samples were taken with a *Zeiss* Axioplan 2 fluorescent microscope using a green fluorescent filter. Control images of samples incubated in serum and then only in the secondary antibody were taken to assess non-specific binding and auto-fluorescence. The intensity per unit area of the stained samples was measured, corrected by the intensity per unit area of the control samples, and used to quantify fibronectin adsorption.

7.2.3 Cell Culture of Human Osteoblasts

Commercial human osteoblasts (*PromoCell*), isolated from a 68 Caucasian male, were cultured for 12 days prior to seeding on samples. Cells arrived at passage 2 and cells from passage 4 were seeded onto 10 samples each of micronHA, CaP layer and nano HA, at a concentration of 50,000 cells/mL. Immediately prior to cell seeding, the samples were heat sterilized at 200°C for 2 hours. In order to seed cells only on the top surface, a 10 μL drop of cell suspension was placed on each sample and allowed to sit for 2 hours in a humidity chamber to allow initial cell attachment. Then each sample was placed in 1 mL of culture medium (McCoy's modified medium plus 10% fetal bovine serum, 1% L-glutamine, and 0.2% Vitamin C) within a 24 well plate. The 24 well plate was then placed in an incubator at 37°C.

7.2.3.1 Cell Attachment

After 1, 3 and 7 days of culture, 3 samples per time point were removed from culture. An MTS assay [3-(4,5-dimethylthiazol-2-yl)-5-(3-carboxymethoxyphenyl)-2-(4-sulfophenyl)-2H-tetrazolium] was performed to quantify cell number as an assessment of cell attachment on each sample using the CellTiter 96 AQ$_{\text{ueous}}$ Non-Radioactive Cell Proliferation Assay (*Promega*, Product No. G5421) to determine cell number. In this assay MTS is bioreduced by cells into formazan which can be measured through absorbance at 490 nm, and the quantity of formazan is directly proportional to the number of living cells in culture [35]. Samples were incubated at 37°C in 500 µL of 20 v/v% of MTS reagent in cell culture medium for 4 hours. After incubation the medium was transferred to a 96 well plate and the absorbance at 490 nm was measured via a Multiskan EX plate reader (*Thermo Electron Corporation*). Values were compared to those of a standard curve produced similarly using known dilutions of the initial seeding cell suspension.

7.2.3.2 Fluorescent Microscopy and Cell Spreading

After the MTS assay, the same samples were then placed in 1 mL of fresh culture medium to which 1 µL of 2 mM calcein AM (*Invitrogen*, Product No. C1430) in DMSO was added. Calcein AM is a cell-permeable dye and in live cells the non-fluorescent calcein AM is converted to green-fluorescent calcein [36]. The samples were incubated for 30 minutes at 37°C and then mounted for florescent microscopy. Images of stained samples were taken with a *Nikon* Microphot-SA EPI-FL3 fluorescent microscope, using a green fluorescent filter, to measure cell spreading. Using *SigmaScan Pro* the cell areas in μm^2 were measured.

7.2.3.3 Real-time reverse transcription polymerase chain reaction (PCR)

After fluorescence microscopy, the samples were place in 0.5 mL of TRIzol® (*Gibco BRL*, Product No. 15596) to lyse the cells and the cell lysis was retained in a microcentrifuge tube for RNA extraction. The RNA was extracted through the following procedure. 100 μL of chloroform was added to each tube, and then each tube was mixed by hand, incubated at room temperature for 3 minutes, and centrifuged at 12,000 g for 15 minutes at 4°C. The colorless aqueous phase was then transferred to a new to tube to which 1.5 μL of linear acrylimide (*Ambion*, Product No. 9520) was added as a co-precipitator. Then 250 μL of isopropanol was added to precipitate the RNA, the tubes were mixed by hand and then chilled at -20°C for 15 minutes after which they were centrifuged at 12,000 g for 15 minutes at 4°C. The supernatant was removed and the pellet was washed twice with ethanol and then re-suspended in sterile RNAse free water. A 10× dilution series of RNA was also prepared from a near confluent 75 cm^2 flask of *Promocell* human osteoblasts in order to create a standard curve. PCR was performed using SuperScript III Platinum One-Step Quantitative PCR Kit (*Invitrogen*, Product No. 11732-020) and *Exiqon* probes and primers on a *Strategene* MX3000 RT PCR Thermocycler. The genes amplified were glyceraldehydes 3-phosphare dehydrogenase (GAP) as a housekeeping gene, alkaline phosphatase (ALP) and type I collagen (COL) using *Exiqon* universal probes human #90, human #12, and human #7 respectively. Relative mRNA levels were measured by normalizing to the GAP housekeeping gene and comparison to the standard curve. Additionally the ratio of ALP/COL mRNA was examined as an indicator of osteoblast differentiation [37].

7.3 RESULTS

7.3.1 Sample Characterization

Sample characterization is summarized in **Table 7.1**. Contact angle measurements showed micronHA to have an instantaneous contact angle (78 ± 3°, n=12), significantly greater than CaP layer (72 ± 4°, n=12), and both were significantly greater than nanoHA (69 ± 4°, n=12) ($p<0.05$). TMAFM images of each surface are shown in **Fig. 7.1**. The average grain size of the micronHA was 1.5 ± 0.7 μm (n=93), while the size of the intragranular crystallites in the CaP precipitated layer were 43 ± 10 nm (n=54). It still was possible to observe the underlying larger grain size of the micronHA surface beneath the precipitated CaP layer. The grain size of the nanoHA was 83 ± 27 nm (n=89). Average large scale RMS roughness for four 3 μm scans was 50 ± 10 nm, 59 ± 29 nm and 89 ± 21 nm for micronHA, CaP layer and nanoHA respectively where micronHA and CaP layer are statistically similar and nanoHA significantly rougher ($p<0.05$). Average smaller scale linear RMS roughness showed micronHA, CaP layer, and nanoHA to have roughnesses of 3 ± 1 nm, 8 ± 4 nm, and 23 ± 5 nm respectively. At the smaller scale nanoHA is significantly rougher than CaP layer which is significantly rougher than micronHA ($p<0.05$).

Property	Technique	HA	CaP Layer	NanoHA
Ca/P ratio	XPS	1.63	1.02	1.45
Crystal structure	XRD or XPS	hydroxyapatite	octacalcium phosphate	hydroxyapatite
Grain size	AFM	1.48±0.68 μm	44.7±12.7 nm	83±27 nm
Contact angle	Video Contact Angle Measurement	78±3°	72±4°	69±4°
RMS roughness of 3 μm scan	AFM	50±10 nm	59±29 nm	89±21 nm
200nm linear intragrain RMS roughness	AFM	3±1 nm	8±46 nm	23±5 nm

Table 7.1: Surface material properties for micronHA, CaP precipitated layer, and nanoHA

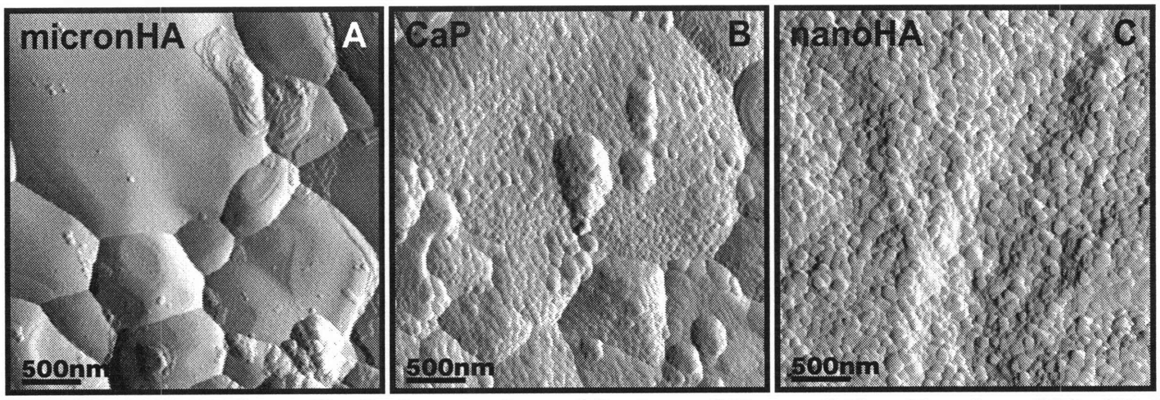

Figure 7.1: TMAFM amplitude images in ambient conditions of the **A)** micronHA, **B)** CaP precipitated layer on micronHA and **C)** nanoHA surfaces.

7.3.2 Protein Adhesion

The stained CaP layer had the greatest corrected intensity. MicronHA had ~30% and nanoHA had ~20% of the corrected intensity of the CaP layer sample, where intensity is proportional to amount of absorbed fibronectin. Therefore, the Ca/P layer had the greatest fibronectin adhesion followed by micronHA and then nanoHA at 30% and 20% respectively.

7.3.3 Cell Attachment and Spreading

From day 1 to day 3 all samples showed increased cell number, as measured via MTS (**Fig. 7.2A**), and cell spreading (**Fig. 7.2B**), as measured through fluorescent microscopy (**Fig. 7.3**). On day 7 however, all samples showed a decrease in cell number. Calcein staining, partially dependant on cell metabolism seemed weaker on day 7 which could be caused by less active cells.

ANOVA statistics with Fisher post hoc tests showed statistically different material dependence of cell number at day 3 and cell area at day 3 and 7. Day 1 results were inconclusive. In general, an increase in cell attachment was seen on the nanoHA and a decrease in cell attachment was seen on the CaP layer in comparison to micronHA. Additionally, decreased cell areas were observed on both nanoHA and the CaP layer compared to micronHA.

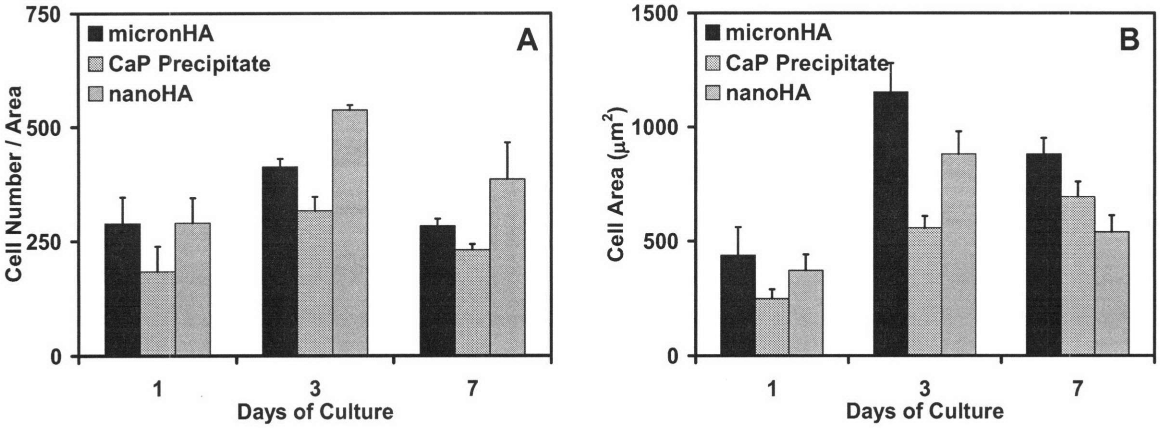

Figure 7.2: A) Average (n=3) cell number per area on micronHA, CaP layer, and nanoHA with standard error and **B)** Average (n~10) cell area.

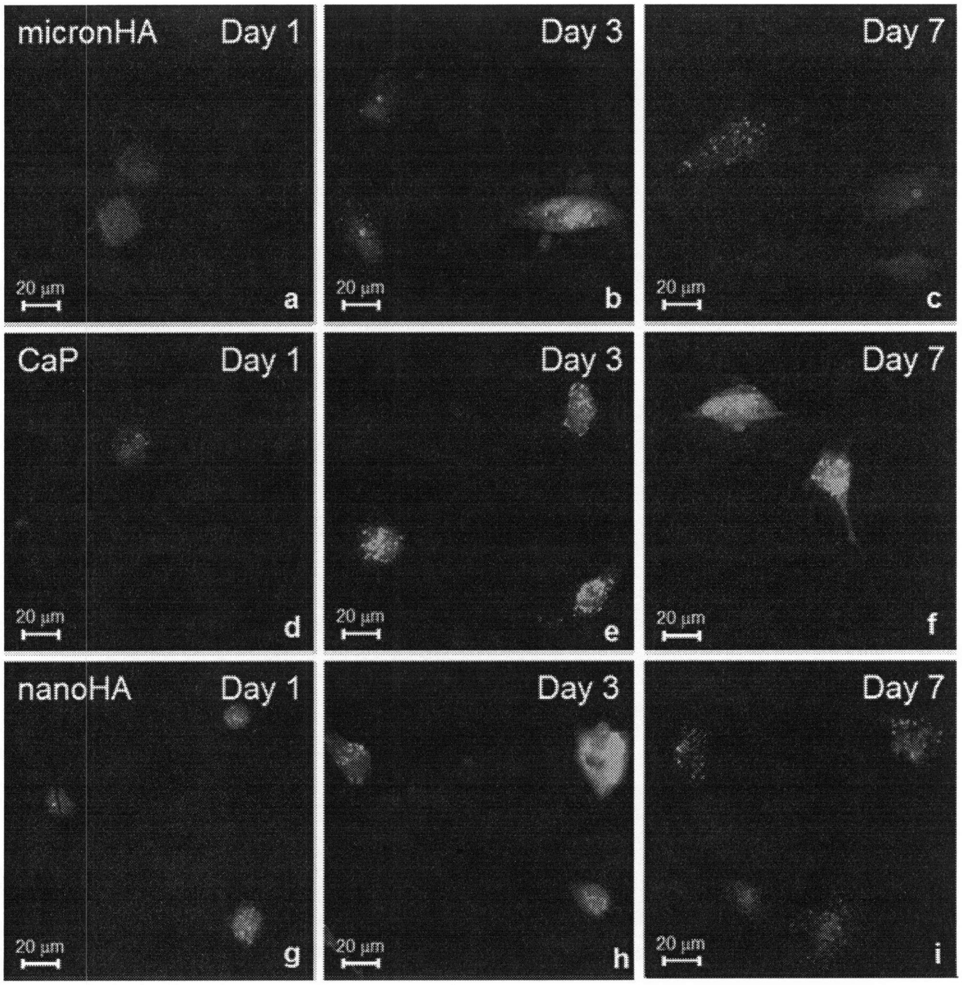

Figure 7.3: Representative fluorescent images of calcein stained cells on **a-c)** micronHA, **d-f)** CaP layer, and **g-i)** nanoHA after 1, 3 and 7 days in culture.

7.3.4 Real-time reverse transcription polymerase chain reaction (PCR)

Due to slow cell grow and the decreased cell activity by day 7, there was not enough RNA for amplification using day 1 or day 7 samples. The mRNA COL/GAP, ALP/GAP, and COL/ALP ratios are shown in **Fig. 7.4** for all samples after 3 days of culture. Ratios to GAP are used to normalize by cell number. ANOVA statistics with Fisher post hoc tests showed COL/GAP mRNA ratio to have no material dependence after 3 days of culture. ALP/GAP and ALP/COL mRNA ratios seem larger for CaP layer over micronHA and nanoHA but were not statistically different due to small number of samples and large standard error.

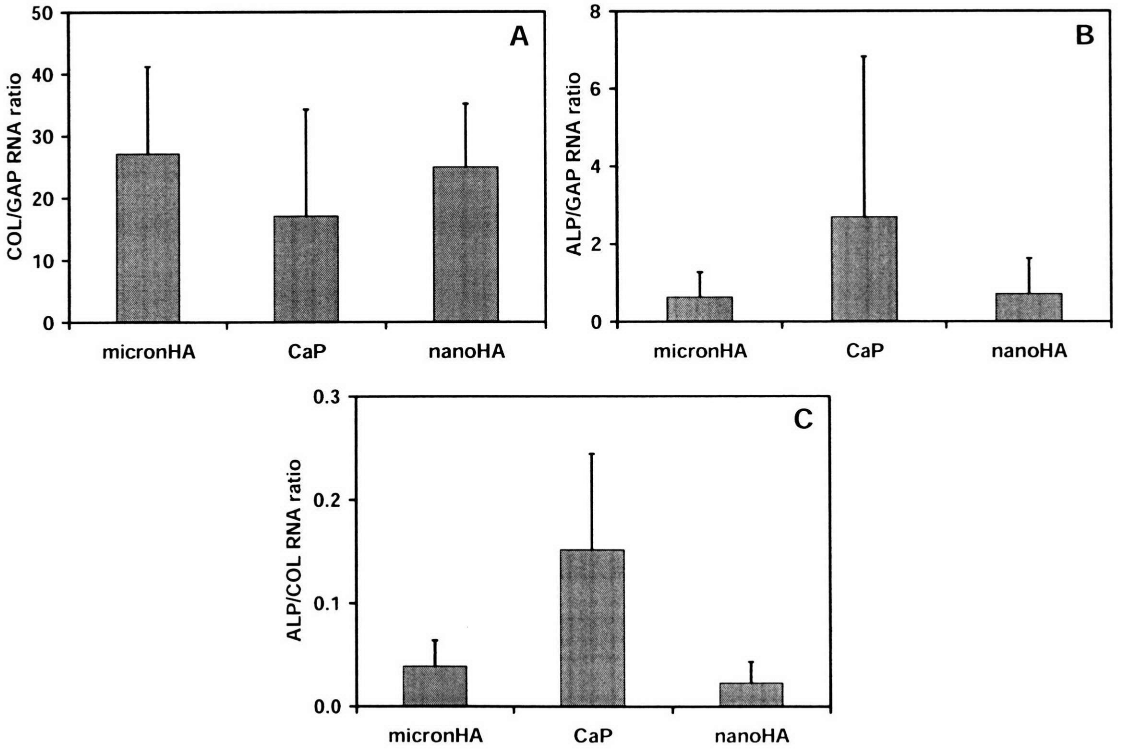

Figure 7.4: **A)** COL/GAP mRNA ratio of all three samples after 3 days of culture. **B)** ALP/GAP mRNA ratio of all three samples after 3 days of culture. **C)** ALP/COL mRNA ratio of all three samples after 3 days of culture.

7.4 DISCUSSION

Human osteoblast response quantified here on micronHA, nanoHA and a CaP precipitated layer includes cell attachment measured through MTS assays, cell spreading measured through fluorescent microscopy, and cell differentiation observed through ALP/COL mRNA ratios. Analysis of day 3 samples, where cell number was greatest, shows nanoHA to have the greatest cell attachment while CaP layer had the least. NanoHA and CaP layer had smaller cell areas than micronHA for all time points. MicronHA and nanoHA are both phase pure hydroxyapatite, and previous work has shown the surface forces of micronHA and nanoHA to be very similar although their surface morphologies are very different. Previous work has also shown the surface forces of micronHA and a precipitated CaP layer to be very similar but that there are differences in the crystal structure and Ca/P ratio. Therefore surface forces are not a likely cause for the differences in osteoblast response seen here. The surface properties examined here that could account for differences seen in osteoblast response include surface morphology and topography, Ca/P ratio, or wettability. Each of these possible contributions will be discussed following.

7.4.1 Effect of Surface Morphology and Topography

It is widely recognized that surface topology on both a micro and nano scale significantly influences cell response [11,20-24] and generally rougher surfaces have increased cell response [11,24,25]. It is likely that the increased osteoblast attachment and decreased cell areas on nanoHA over micronHA is due purely to surface morphology and properties such as grain size and roughness. Increased attachment is consistent with the literature that has found increased roughness to be correlated with increased bone cell adhesion on polished micronHA [11] and on nanostructured HA [27,29,31]. Decreased cell areas of nanoHA compared to micronHA is also consistent with the literature that has found decreased cell areas on nanostructured ceramics [29,31]. Increased cell attachment and decreased cell areas on nanostructured ceramics could be due to the tendency of cells to attach to areas of junction or discontinuity [21] or to increased adhesion protein density or function.

The importance of proteins in mediating cell adhesion is well established [5,33,38,39] and it has been shown that in the absence of serum, osteoblast adhesion to nanostructured ceramics was independent of nano grain size, demonstrating the critical role proteins play in the increased osteoblast adhesion to nanostructured ceramics [28]. For anchorage-dependant cells such as osteoblasts, adhesion is critical for subsequent cell function [40] and so greater protein adhesion could account for increased osteoblast function on nanostructured ceramics [23,29,41].

Unexpectedly, results showed nanoHA to have the smallest fibronectin adhesion. One possible explanation could be that although fibronectin adhesion is less, other adhesion protein adhesion, such as vitronectin, which has also been shown to mediate osteoblast attachment [42], might be increased. Increased protein adhesion onto nanostructured HA over non-nanostructured HA from serum has been observed in the literature, but the absorbance of individual proteins is more varied [27]. Increased protein adhesion could be partly due to increased surface area of nanostructured materials but results in the literature indicate there are other important factors. Surface topology, as measured by surface radius of curvature on the order of 8-80 nm, has been shown to affect protein adhesion and in particular, proteins of different shapes interact with the surface in dissimilar ways [43]. It was found that vitronectin adsorption from serum was selectively increased by 10% and the protein configuration was more unfolded on nanostructured alumina compared to conventional alumina [29]. Greater unfolding could expose more specific cell-adhesion areas and therefore increase cell adhesion [20,29]. If there is a greater density of cell adhesion areas, cells are likely to spread less as the focal points of the cell will be closer together [5]. Therefore specific interactions between adhesion proteins and surface morphology such as decreased grain size, increased grain boundaries, and increased surface curvature could account for the increased osteoblast attachment to nanoHA and decreased spreading seen here.

Although the CaP precipitated layer had decreased attachment, the affect of surface roughness is seen in decreased cell areas, analogous to nanoHA, which could be due to similar specific interactions between adhesion proteins and surface morphology since the grain size and surface curvatures are comparable. The decreased cell attachment is likely due to Ca/P ratio discussed in the next section.

7.4.2 Effect of Ca/P ratio

Previous work has shown the surface forces of micronHA and a precipitated CaP layer to be very similar but that there are differences in the crystal structure and Ca/P ratio. MicronHA has a hydroxyapatite crystal structure and Ca/P ratio = 1.63 versus an octacalcium phosphate (OCP) crystal structure and Ca/P ratio = 1.02 of the CaP precipitated layer. Greater fibronectin adhesion was observed for the CaP layer over the others which is consistent with the literature that found CaP precipitated surface onto bioactive glass to have increased fibronectin adhesion over HA [32]. It is interesting to note however, that increased fibronectin adhesion did not correlate with increased osteoblast attachment since the CaP layer had the least cell attachment of the samples studied. However, the CaP layer also had a significantly lower Ca/P ratio than the other samples and decreased cell attachment has been associated with decreased Ca/P ratio due to increased solubility and therefore decreased surface stability [8]. The increase in surface roughness of the CaP layer over the micronHA did not increase cell attachment, as it did for nanoHA. Therefore, the decreased Ca/P ratio must be the dominant factor here in cell attachment.

Although the higher ALP/COL mRNA ratio of CaP layer was not statistically significant, it could indicate an area of future interest. The possible trend might be that although the CaP layer has less cell adhesion than micronHA, the cells that do attach become more differentiated into mature osteoblasts. Previous work showed that the incorporation of the bone protein osteocalcin into the SBF during precipitation produced a CaP layer with an increased Ca/P ratio. It is possible then that *in vivo* the CaP layer which forms has an increased CaP layer over that formed here, which could have a positive effect on cell attachment in addition to enhanced differentiation.

7.4.3 Effect of wettability

In addition to surface morphology, surface energy or wettability could also influences protein and cell interactions. Increased surface energy or wettability of a surface has been correlated with increased cell spreading [5,6] and decreased wettability has been correlated with increased protein adhesion and cell adhesion [5,25,44]. However, observations here, increased cell spreading on nanoHA, are in direct contrast to trends in the literature. A possible explanation could be that surface roughness and wettability are not independent parameters. For smooth surfaces, wettability is directly related to surface energy [45,46], but for rough surfaces the interaction is more complicated. In the Wenzel model, which describes the contact angle for a rough surface, increased surface roughness increases the contact angle for surfaces with contact angle > 90° and decreases the contact angle for surface with contact angle < 90° [47]. Common materials such as titanium, calcite, quartz, barite, and talc of all been shown to have increased wettability with increased roughness [48,49] and increased contact angle with increased grain size has been observed for nanostructured ceramics in the literature [27]. Since the order of decreasing contact angle was proportional to the increase in roughness, it is likely contact angle measurements were not a good measurement of surface energy and the actual wettabilities of these surfaces may be more similar than were measured.

7.5 CONCLUSION

Human osteoblast response to three surfaces has been examine and it has been determined that surface morphology, as defined through grain size and roughness, and surface Ca/P ratio are the largest influences on osteoblast behavior for these three surfaces. Increased osteoblast attachment with increased surface roughness and decreased osteoblast attachment with decreased Ca/P ratio were observed. Additionally, it is possible that formation of CaP layers on a biomaterial surface affects osteoblast differentiation. However, it is important to remember that a biomaterial's interaction with the biological environment is a very complex process and it is difficult to de-convolute the effects of many interdependent processes.

7.6 REFERENCES

[1] P. Ducheyne, Q. Qiu: *Biomaterials*; 20 (1999), p. 2287.

[2] J.D. de Bruijn, C.A. van Blitterswijk, J.E. Davies: *J Biomed Mater Res*; 29 (1995), p. 89.

[3] H.W. Denissen, K. de Groot, P.C. Makkes, A. van den Hooff, P.J. Klopper: *J Biomed Mater Res*; 14 (1980), p. 713.

[4] M. Neo, T. Nakamura, C. Ohtsuki, T. Kokubo, T. Yamamuro: *J Biomed Mater Res*; 27 (1993), p. 999.

[5] B.D. Ratner, A.S. Hoffman, F.J. Schoen, J.E. Lemons, editors. *Biomaterials science: An introduction to materials in medicine*. San Diego: Academic Press; (1996).

[6] S.A. Redey, M. Nardin, D. Bernache-Assolant, C. Rey, P. Delannoy: *J Biomed Mater Res*; 50 (2000), p. 353.

[7] S. Best, B. Sim, M. Kayser, S. Downes: *J Mater Sci: Mater Med*; 8 (1997), p. 97.

[8] T. Suzuki, T. Yamamoto, M. Toriyama, K. Nishizawa, Y. Yokogwa, M. Mucalo, et al.: *J Biomed Mater Res*; 34 (1997), p. 507.

[9] C. Knabe, R. Gildenhaar, G. Berger, W. Ostapowicz, R. Fitzner, R.J. Radlanski, et al.: *Biomaterials*; 18 (1997), p. 1339.

[10] C. Knabe, R. Gildenhaar, G. Berger, C.R. Howlett, B. Markovic, H. Zreiqat: *Biomaterials*; 25 (2004), p. 335.

[11] D. Deligianni, N. Katsala, P.G. Koutsoukos, Y. Missirlis: *Biomaterials*; 22 (2001), p. 87.

[12] A. El-Ghannam, P. Ducheyne, I.M. Shapiro: *J Biomed Mater Res*; 36 (1997), p. 167.

[13] T. Kokubo, H. Kushitani, S. Sakka, T. Kitsugi, T. Yamamuro: *J Biomed Mater Res*; 24 (1990), p. 721.

[14] J. Hamagami, G. Yamaguchi, K. Kanamura, T. Umegaki: *Bioceramics*; 14 (2002), p. 279.

[15] K. Onuma, A. Ito, T. Tateishi, T. Kameyama: *J cryst growth*; 154 (1995), p. 118.

[16] J.H.C. Lin, K.H. Kuo, S.J. Ding, C.P. Ju: *J Mater Sci: Mater Med*; 12 (2001), p. 731.

[17] Y. Leng, J. Chen, S. Qu: *Biomaterials*; 24(2125-2131) (2003), p.

[18] K.A. Khor, H. Li, P. Cheang: *Biomaterials*; 24 (2003), p. 769.

[19] R.L. Sammons, J. Sharpe, P.M. Marquis: *Biomaterials*; 15 (1994), p. 842.

[20] E. Palin, H. Liu, T.J. Webster: *Nanotechnology*; 16 (2005), p. 1828.

[21] A. Curtis, C. Wilkinson: *Biomaterials*; 18 (1997), p. 1573.

[22] C.D.W. Wilkinson, M. Riehle, M. Wood, J. Gallagher, A.S.G. Curtis: *Mat Sci Eng C*; 19 (2002), p. 263.

[23] J. Tan, W.M. Saltzman: *Biomaterials*; 25 (2004), p. 3593.

[24] D.M. Brunette, D. Chehroudi: *J Biomech Eng*; 121 (1999), p. 49.

[25] M. Lampin, R. Warocquier-Clerout, C. Legris, M. Degrange, M.F. Sigot-Luizard: *J Biomed Mater Res*; 36 (1997), p. 99.

[26] A. Wennerburg, T. Albrektsson. In: Ellingsen J, Lyngstadaas S, editors. *Bio-implant interface: Improving biomaterials and tissue reactions*; (2003).

[27] T.J. Webster, C. Ergun, R.H. Doremus, R.W. Siegel, R. Bizios: *J Biomed Mater Res*; 51 (2000), p. 475.

[28] T.J. Webster, R.W. Siegel, R. Bizios: *Biomaterials*; 20 (1999), p. 1221.

[29] T.J. Webster, C. Ergun, R.H. Dormeus, R. Siegal, R. Bizios: *Biomaterials*; 21 (2000), p. 1803.

[30] E.S. Ahn, N.J. Gleason, A. Nakahira, J. Ying: *Nano Lett*; 1(3) (2000), p. 149.

[31] E.S. Ahn. Nanostructure apatites as orthopedic biomaterials [PhD Thesis]. Cambridge, MA: Massachusetts Institute of Technology; 2001.

[32] A. El-Ghannam, P. Ducheyne, I.M. Shapiro: *J Bone Jt Surg*; 17 (1999), p. 340.

[33] C.R. Howlett, M.D.M. Evans, W.R. Walsh, G. Johnson, J.G. Steele: *Biomaterials*; 15 (1994), p. 213.

[34] M. Akao, H. Aoki, K. Kato: *J Mater Sci*; 16 (1981), p. 809.

[35] A. Cory, T. Owen, J. Barltrop, J. Cory: *Cancer Commun*; 3 (1991), p. 207.

[36] R. Lichtenfels, W. Biddison, K. Schulz, A. Vogt, R. Martin: *J Immun Meth*; 172 (1994), p. 227.

[37] D.C. Ireland, S. Bord, S. Beavan, J. Compston: *J Cell Biochem*; 91 (2004), p. 594.

[38] C.E. Orsello, D. Lauffenburger, D. Hammer: *TRENDS in Biotechnology*; 19(8) (2001), p. 310.

[39] M. Cohen, D. Joester, B. Geiger, L. Addadi: *ChemBioChem*; 5 (2004), p. 1393.

[40] A.J. Freemont: *Int J Exp Pathol*; 74 (1993), p. 411.

[41] R.L. Price, K.M. Haberstroh, T.J. Webster: *Med Biol Eng Comput*; 41 (2003), p. 372.

[42] B.A. Dalton, C.D. McFarland, T.R. Gengenbach, H.J. Griesser, J.G. Steele: *J Biomater Sci, Polym Ed*; 9(8) (1998), p. 781.

[43] P. Roach, D. Farrar, C. Perry: *J Am Chem Soc*; 128 (2005), p. 3939.

[44] A. Sethuraman, M. Han, R.S. Kane, G. Belfort: *Langmuir*; 20 (2004), p. 7779.
[45] P. Hiemenz, R. Rajagopalan, editors. *Principles of colloid and surface chemistry*. Third ed. New York: Marcel Dekker, Inc.; (1997).
[46] B.D. Ratner, A.B. Johnston, T.J. Lenk: *J Biomed Mater Res*; 21(A1) (1987), p. 59.
[47] R.N. Wenzel: *J Phys Colloid Chem*; 53 (1949), p. 1466.
[48] F. Rupp, L. Scheideler, D. Rehbein, D. Axmann, J. Geis-Gerstorfer: *Biomaterials*; 25 (2004), p. 1429.
[49] U. Ulusoy, M. Yekeler: *Chem Eng Proc*; 44 (2005), p. 557.

CHAPTER 8: Conclusions

Three model synthetic hydroxyapatite (HA) based bioceramic systems were examined; HA, silicon substituted HA (SiHA) and nanostructure HA (nanoHA). Nanoscale surface chemical properties such as Ca/P ratio, charge distribution, and Hamaker constant were quantified as well as morphological structure such as grain size, shape, distribution, and roughness. The form of a biomaterial, the nanoscale surface chemical properties and morphological structure, will govern its interaction with the biological environment. The direct measurement of ultrastructure and nanoscale surface forces of model HA based biomaterials compared with *in vitro* and *in vivo* data will lead to better understanding of the impact these properties have on the physiochemical processes occurring at the biomaterial-biological interfaces influencing bioactivity.

It was found that SiHA had increased surface charge, Hamaker constant and adhesion forces over HA but similar morphology and that nanoHA had similar surface charge, Hamaker constant, and adhesion forces but significantly different morphology in that it had increased roughness along with much smaller grain size. Through comparison with data in the literature it was concluded that SiHA's increased bioactivity over HA could be due to the increased nanoscale surface charge, Hamaker constant, and adhesion forces since they have similar micro- and meso-scale properties. The increased bioactivity of nanoHA over HA is likely due to purely morphological differences since the surface forces were so similar. Therefore, increased negative surface charge, Hamaker constant, surface adhesion and surface roughness all encourage bioactivity.

Calcium phosphate (CaP) layer precipitation, essential for bone bonding, was examined on both the HA and SiHA surface. It was determined that a negative surface charge is necessary for CaP precipitation from SBF and that the magnitude of the charge partly determines the morphology of the precipitate. The transitional electric charge for elongated to isotropic precipitation morphology is approximately -0.008 C/m^2 where smaller negative charge is likely to produce elongated precipitates and larger negative charge is likely to produce isotropic precipitates. Furthermore, through examination of the literature, surfaces that show increased alignment of needle like precipitates perpendicular to the surface, equivalent to the isotropic precipitate regions, are associated with increased bioactivity. Therefore a negative surface charge of at least -0.008 C/m^2 is desired for superior bioactivity.

Human osteoblasts were cultured on HA, a CaP precipitated layer on HA from simulated body fluid, and nanoHA so that osteoblast response to these surfaces could be quantified. Response measured included; cell attachment measured through a cell proliferation assay, cell spreading measured through fluorescent microscopy, and cell differentiation measured by qualitative real-time reverse transcription polymerase chain reaction (PCR). Increased osteoblast attachment was observed with increased surface roughness, and decreased osteoblast attachment was observed with decreased Ca/P ratio. It was determined that surface morphology and surface Ca/P ratio were the largest influences on *in vitro* osteoblast behavior, and therefore bioactivity, between these three surfaces.

Although it showed decreased osteoblast attachment, it is possible that precipitated CaP layers on a biomaterial surface enhance osteoblast differentiation, as seen by increased ALP/COL mRNA ratio. Therefore, it might be advantageous to determine a way to create a precipitated CaP layer with an increased Ca/P ratio such that cell attachment would be enhanced along with differentiation. Incorporation of the bone protein osteocalcin into SBF during CaP precipitation produced a CaP layer with increased Ca/P ratio, so CaP precipitation with biomolecules might be a promising direction to explore.

Of the properties examined, a HA-based biomaterial with a high degree of surface roughness, a Ca/P ratio of at least 1.45, a minimum negative surface charge of -0.008 C/m^2, and increased Hamaker constant would be optimal for increased bioactivity. One way to obtain such a biomaterial would be to fabricate nano-structured SiHA. The preparations of both SiHA and nanoHA begin with similar aqueous precipitation reactions, so it is conceivable that their preparation methods are compatible and that nano-structured SiHA could be created. Future work would be needed to confirm this.

Individually quantifying all possible contributions to bioactivity is critical to the optimization, development, and design of new HA-based biomaterials. However, it is important to remember that a biomaterial's interaction with the biological environment is a very complex process and it is difficult to de-convolute the effects of many interdependent processes. *In vivo* studies should be used for final bioactivity assessment.